Final Report

February 1, 1990

MESOSCALE MONITORING OF THE SOIL FREEZE/THAW BOUNDARY FROM ORBITAL MICROWAVE RADIOMETRY

NASA Grant: NAG5-852

Submitted by:	Craig Dobson	Principal Investigator
	Fawwaz T. Ulaby	Co-Investigator
	Brian Zuerndorfer	Graduate Student
	Anthony W. England	Co-Investigator

Radiation Laboratory
Department of Electrical Engineering and
Computer Science
University of Michigan
Ann Arbor, MI 48109

nam

MRC636

CONTENTS

I Introduction

We have recently completed the NASA funded study, "Mesoscale monitoring of the soil freeze/thaw boundary from orbital microwave radiometry." While most of our objectives were met, a few will have to be addressed within the newly begun NASA project, "Mapping regional freeze/thaw patterns with satellite microwave radiometry." The salient scientific products of the initial project are that regional freeze/thaw maps can be extracted from Nimbus 7, Scanning Multichannel Microwave Radiometer (SMMR) data, that diurnal thermal gradients have a small but measurable effect upon the SMMR spectral gradient, and that scale-space filtering can be used to improve the spatial resolution of a freeze/thaw classified image.

This Final Report of the initial project contains a summary of the investigation, a discussion of accomplishments and of unresolved issues, and copies of publications and of conference abstracts and proceedings. We very much appreciate the opportunity to have worked upon this exciting, and, we believe, fruitful project.

II Summary of the Investigation

Soil moisture contributes to the energy exchange between the air and ground through latent heats of fusion and vaporization, and to rainfall runoff through the field moisture deficiency of a drainage basin. Whether or not soil moisture is frozen affects both the rate of energy transfer to the atmosphere, and the infiltration capacity of the soil. The amount and state of soil moisture are regional parameters that one would like to estimate using satellite remote sensing. There is a large body of literature about estimating soil moisture from radiobrightness (e.g. Burke et al., 1979; Wang et al., 1982; Schmugge, 1983; Jackson et al., 1984; Camillo and Schmugge, 1984; and Schmugge et al., 1986). We have developed a technique for mapping the spatial extent of frozen soils from the spectral characteristics of the 10.7-37 GHz radiobrightness. Through computational models for the spectral radiobrightness of diurnally heated, freezing soils, we identified a distinctive radiobrightness signature for frozen soils, and cast that signature as a discriminant for unsupervised classification. Our initial results were reported at the Interdisciplinary Science Land Surface Climatology Program's (ISLSCP) meeting in Las Cruces, NM, November 16-18, 1988 by A. W. England, and will appear as a paper in a special NASA ISLSCP journal publication (Zuerndorfer et al., 1989).

Freezing influences the apparent radiobrightness temperature of the ground, T_b, through parameters in the approximation (Ulaby et al., 1981),

$$T_b = e\,T_o + (1\text{-}e)\,T_{sky},$$

where e and T_o are the emissivity and surface temperature of the ground, respectively, and T_{sky} is the effective sky brightness. In this approximation, atmospheric transmissivity is ignored. Frozen ground exhibits signatures of (1) lower thermal temperature, T_o, (2) higher emissivity, e, and, (3) a decrease in brightness temperature with microwave frequency, f,

$$\frac{\partial T_b}{\partial f} < 0.0$$

Signatures (1) and (2) are frequently ambiguous indicators of frozen ground because the variations in radiobrightness that result from freezing are easily confused with the effects of

variations in soil moisture. Water molecules in frozen plants and soils are not free to align themselves with microwave electric fields. This constraint upon the rotational freedom of water gives rise to an apparent dryness to microwaves. The consequence is a decrease in the real part of the dielectric constant, and an increase in frozen soil emissivity. For example, the real part of dielectric constants, ε', and corresponding emissivities at nadir, e(0), of two, homogeneous, smooth surfaced, 15% moist soils at 10 GHz are (ε' from Hoekstra and Delaney, 1974):

	+ 5° C			- 5° C		
Material	ε'	e(0)	T_b	ε'	e(0)	T_b
Goodrich Clay	8.2	0.77	221	4.9	0.86	235
Fairbanks Silt	9.6	0.74	214	4.1	0.89	242

Because of increasing emissivity with freezing, a 10° decrease in the clay and silt soil temperatures, from +5° C to -5° C, would cause an increase in T_b of approximately +14 K and +28 K, respectively. The positive direction of change in T_b with soil freezing will cause confusion in discrimination between moist soils which will appear radiometrically warmer when frozen, and dry soils which undergo little molecular change and will appear radiometrically colder.

The shift in emissivity with freezing is most pronounced at the lower microwave frequencies. At 37 GHz, the effect is reduced but not absent. We observe that the 37 GHz radiobrightness correlates relatively well with air temperature (Figure 1). Since soil surface temperature should follow the air temperature, the 37 GHz radiobrightness can be expected to provide a reasonably reliable estimate of soil surface temperature. However, discrimination based only on the 37 GHz radiobrightness would misclassify too often.

The third signature of frozen soil occurs because freezing reduces the imaginary part of the dielectric constant, ε'', proportionally more than it does the real part, ε'. The loss tangent,

$$\tan \delta = \varepsilon''/\varepsilon'$$

is a measure of the attenuation per microwave wavelength in emitting media. Reduced loss tangent, or lower attenuation, means that thermally emitted photons originate deeper within emitting media. That is, the effective depth of emission, z_e, ($1-e^{-1}$ of the emission originates above z_e) becomes a larger fraction of the free-space wavelength, λ_o (England, 1974, 1975, 1976, and 1977). For example, Goodrich Clay and Fairbanks Silt exhibit an increase of z_e with freezing (dielectric data from Hoekstra and Delaney ,1974) ,

	+ 5° C				- 5° C			
Material	ε'	ε''	tan δ	z_e	ε'	ε''	tan δ	z_e
Goodrich Clay	8.2	3.5	0.43	0.13 λ_o	4.9	1.0	0.20	0.36 λ_o
Fairbanks Silt	9.6	5.0	0.52	0.10 λ_o	4.1	0.02	0.005	15.7 λ_o

The effective emission depth of moist soils is typically 10% of the free-space wavelength. Frozen soils have effective emission depths that may be 30% or more of free-space wavelength. The effective emission depth of frozen sandy soils, like the Fairbanks Silt, can be several wavelengths. In the more transparent emitting media, particularly in frozen sandy soil or dry snow, the greater average thermal photon path lengths have two effects: (1) a greater likelihood that thermal gradients affect spectral gradients, and (2) a greater opportunity for volume scattering of photons.

(1) Thermally induced spectral gradients occur because longer wavelength photons tend to originate below the optical surface where thermal temperatures may differ by several degrees from surface temperatures. For the lower loss tangents of frozen soil, this difference in average emitting depth is enough to reflect near surface thermal gradients caused by diurnal heating. That is, a positive thermal gradient, $\partial T_o/\partial z$, will yield a negative spectral gradient, $\partial T_b/\partial f$. SMMR data are collected at midnight and noon. In the absence of changing weather conditions, midnight thermal gradients will be positive and noon thermal gradients will be negative (Figure 2) so that midnight spectral gradients will be negative, and noon spectral gradients will be positive. An average +0.2 Kelvin/f(GHz) shift in the spectral gradient is observed between midnight and noon for SMMR radiometric brightnesses (Figure 3). While we have developed a computer model of these gradient effects, for the purposes of this report, thermally induced spectral gradients are noise to be filtered out.

(2) The second consequence of soil freezing is a greater opportunity for volume scattering -- particularly at shorter microwave wavelengths. This occurs because of the greater average photon path lengths in frozen soil, and because plants and soil appear increasingly heterogeneous at shorter wavelengths. This "law of darkening" means that, for an isothermal, volume scattering halfspace,

$$\frac{\partial T_b}{\partial f} < 0.0$$

(England, 1974). Frozen terrain may also be snow covered. Dry snow is exceedingly transparent to microwaves so that snow exhibits significant of darkening (Figure 4, Edgerton et al., 1971). That is, both frozen soil and snow tend to exhibit negative spectral gradients. While neither a low 37 GHz radiobrightness nor a negative spectral gradient is solely adequate as a classifier of frozen soils, particularly at the relatively coarse resolutions of the Nimbus-7 SMMR, a discriminant based upon a combination of these signatures appears to classify correctly most of the time.

SMMR radiobrightness data at 6.6 GHz, 10.7 GHz, 18 GHz, and 37 GHz were obtained for August 1, 1984, through December 31, 1984, over an area that included North Dakota, about half of each neighboring state, and part of southern Canada (Figures 7-9). We chose this large, relatively uniform area because of the low spatial resolution of the SMMR instruments -- 150 Km at 6.6 GHz, 100 Km at 10.7 GHz, 60 Km at 18 GHz, and 30 Km at 37 GHz, and because of the importance of soil moisture state to this region's hydrologic processes. The data arrived from the National Space Science Data Center (NSSDC) on 21, high density, SMMR Cell Tapes. Such data are referenced to latitude and longitude in a satellite-centered coordinate system. We produced two types of image products: Single-band, radiobrightness images at the intrinsic resolution of each sensor, and (2) composite, multi-band images at a common resolution based upon local area averaging. Each radiobrightness pixel was referenced to latitude-longitude in a Mercator projection by interpolation and resampling the Cell Tape data. We used a bi-cubic approximation of a sinc function (Moik, 1980) for the interpolation. H and V radiobrightnesses were averaged to produce a single brightness for each pixel for each frequency.

In addition to large area images, local area spatial averages of radiobrightness were calculated for each radiobrightness channel at 7 meteorologic sites within our test region--Miles City, MT; Bismark, Fargo, and Williston, ND; and Abileen, Huron, and Rapid City, SD. A local area is defined as a 150x150 Km cell centered on the meteorological site (150 Km is the spatial resolution of the 6.6 GHz channel). Air and ground temperature data for the Fall of 1984 were obtained from NOAA's National Climatic Data Center in Asheville, North Carolina. Air temperature measurements were available for noon and midnight at the meteorologic sites (i.e., simultaneously with the satellite pass), but ground temperature measurements were for 7:00 a.m. and 7:00 p.m. EST, and were not co-located with the meteorologic sites. Ground temperatures are measured at 5 cm depths. Diurnal heating will affect 5 cm temperatures so that there will be differences between those temperatures and the effective soil temperatures at the times of satellite passes.

Local area averages at the meteorologic sites were used to define the preliminary boundaries in our Freeze Indicator discriminant. For example, Figure 1 illustrates the correlation between 37 GHz radiobrightness and reported air temperature. The nominal line in these figures is a single best fit linear regression in the least squares sense of all local area averages. Individual linear fits will differ slightly as shown in Figure 1(a). We used the nominal line in our discriminant for simplicity, but a more sophisticated discriminant might use the actual least squares fit for the local area and for the time of day. The discriminant boundaries in Figures 1(b) and 1(c) are merely estimates based upon the nominal regression and a compromise between midnight and noon air temperatures that would imply frozen soil (the lower boundary) and thawed soil (the upper boundary). Remember that diurnal temperature gradients will generally cause midnight, sub-surface soil temperatures to be warmer than air temperatures, and noon, sub-surface soil temperatures to be colder.

Similarly, local area averages of spectral gradient versus air temperature were the bases for the spectral gradient decision boundaries shown in Figure 3. Note that the midnight freeze boundary in this example is relatively unambiguous, while a more effective noon freeze boundary would be shifted upwards by 0.2 K/GHz. Again, for simplicity in this initial study, we used discriminant boundaries that were time and location independent.

Our 2-parameter Freeze Indicator incorporates the single-band, 37 GHz radiobrightness, and a spectral gradient based upon linear regression of 10.7, 18, and 37 GHz radiobrightnesses for each 100x100 Km pixel. Based upon the decision boundaries in Figure 1(b) and 1(c), the likelihood of frozen ground in a 37 GHz pixel, p_{37}, is estimated as

$$p_{37} = \begin{cases} 0 & : \quad Tb_{37} > Tb_{max} \\ \dfrac{Tb_{max} - Tb_{37}}{Tb_{max} - Tb_{min}} & : \quad Tb_{min} < Tb_{37} < Tb_{max} \\ 1 & : \quad Tb_{37} < Tb_{min} \end{cases}$$

where Tb_{37} is the measured 37 GHz radiobrightness, and the preliminary decision boundaries are

$$Tb_{max} = 259 \text{ K}$$

$$Tb_{min} = 247 \text{ K}$$

The likelihood of frozen ground based upon spectral gradient decision boundaries in Figure 3(a) and 3(b) is p_{sg}, and is estimated as

$$p_{sg} = \begin{cases} 0 & : \frac{\partial Tb}{\partial f} > \left(\frac{\partial Tb}{\partial f}\right)_{max} \\ \frac{\left(\frac{\partial Tb}{\partial f}\right)_{max} - \frac{\partial Tb}{\partial f}}{\left(\frac{\partial Tb}{\partial f}\right)_{max} - \left(\frac{\partial Tb}{\partial f}\right)_{min}} & : \left(\frac{\partial Tb}{\partial f}\right)_{min} < \frac{\partial Tb}{\partial f} < \left(\frac{\partial Tb}{\partial f}\right)_{max} \\ 1 & : \frac{\partial Tb}{\partial f} < \left(\frac{\partial Tb}{\partial f}\right)_{min} \end{cases}$$

where the preliminary decision boundaries are

$$\left(\frac{\partial Tb}{\partial f}\right)_{max} = 0.3 \text{ K/GHz}$$

$$\left(\frac{\partial Tb}{\partial f}\right)_{min} = -0.3 \text{ K/GHz}$$

These boundaries are preliminary in that they were chosen to yield the fewest misclassifications in plots of the type shown in Figure 5(a) and 5(b). More refined discriminants would incorporate area and time specific decision boundaries. This would be relatively straightforward if there were a higher density of weather stations in the test area. As it is, we believe that diurnal temperature modeling well yield effective time dependent boundaries, and, perhaps, requiring sub-region consistency within a classification will yield improved spatially dependent boundaries. The basic sparseness and lack of control of air and ground data should prompt some caution about over-interpreting these results.

Our freeze/thaw discriminant, or Freeze Indicator, is the product of p_{37} and p_{sg}, and is applied at the scale of the 10.7 GHz data. Resolution differences between different frequency channels can produce anomalous composite image results if the data were processed at their original scale. To avoid these problems, the resolution of the data from each channel is compensated to the (coarse) resolution of the lowest frequency channel used in estimating spectral gradients (i.e. 10.7 GHz and 100 Km resolution). Under certain constraints upon the classification process, these images can be referenced to the higher resolution, 37 GHz format for better location of freeze/thaw boundaries (Zuerndorfer, et al., 1989). The effort needed to do this would be justified as a part of an improved classification process. Figures 7 through 12 include images of the Freeze Indicator for various times during the test period. Black in these images indicates a high likelihood of frozen ground.

Figure 6(a) and 6(b) show normalized brightness temperatures for midnight and noon, respectively, in the northern Great Plains during the Fall of 1984. Normalized brightnesses are the average regional brightness at each microwave frequency divided by the average regional air temperature. Normalized brightness thus has the dimension of emissivity. Note that there is little systematic ordering among the 10.7, 18, and 37 GHz normalized brightnesses during August through most of November. However, during the latter half of November through December, the normalized brightnesses at midnight are uniformly ordered, 10.7 GHz brightnesses are high, 18 GHz brightnesses are middle, and 37 GHz brightnesses are low. That is, they exhibit negative average spectral gradients. The noon normalized brightnesses for December exhibit a similar trend, but with exceptions. These are, we believe, illustrations of the law of darkening for frozen soils. Soils at midnight in December for the northern Great Plains are very likely to be frozen.

Performance of the freeze/thaw discriminant is demonstrated in Figures 7-9 where Freeze Indicator (FI) images are compared with ground and air temperature measurements for midnight on 9/20/84, 10/24/84, and 12/9/84. Midnight FI images are shown as better examples of the potential of a freeze discriminant. Noon FI images are generally less consistent with meteorologic reports because of the contribution of the noontime positive diurnal spectral gradient to the negative frozen ground spectral gradient that we discussed in the last section. Areas not covered by the satellite in a particular pass are shown in white. Tables 1-3 are summaries of the meteorologic reports.

On the night of September 20 (Fig. 7), air temperatures throughout the region were near 60° F and had been above freezing for several days. The FI image shows weak, probably false indications of freezing in the prairies of ND, southern Canada, and the rolling glacial terrain east of the Red River Valley in Minnesota. While the dry air of the northern prairies permits nighttime radiation cooling of the ground to temperatures below that of the air, the more likely explanation for the weak freeze indication is short wavelength scattering by the tall prairie grasses in the northern great plains, and by woodland areas in Minnesota. However, there are no strong indications of freezing in the FI image.

On the night of October 24 (Fig. 8), air temperatures hovered about freezing throughout the area, but had been below freezing at Williston for several days, and generally above freezing toward the east (see the temperatures for Fargo, Aberdeen, and Huron in Table 2). The FI image shows a strong freeze indication in northwestern ND which is consistent with the temperature patterns. Similarly, the definite thaw indication along the Red River Valley is consistent with the warmer temperatures reported and the generally more moist soil in the Valley.

On the night of December 9 (Fig. 9), air temperatures were generally below freezing except at Rapid City, SD, and had been below freezing for several days. There was no more than trace snow on the ground anywhere in the region. The FI image shows strong freeze indications throughout most of the region with weaker indications near Rapid City, and in the Aberdeen-Fargo sub-region (Aberdeen is not shown on the December 9 map because its temperature report was missing for that date). Again, the FI image is consistent with the temperature record.

37 GHz radiobrightness and FI image sequences were produced at midnight and noon for six-day periods in September, October, and December (Figures 10-12). SMMR coverage is based on a 48 hour cycle--midnight (0000 local hours on the date shown), noon (1200 hours on the same date), and then midnight again 36 hours later. However, orbit precession causes gaps in the cycle and variations in the coverage footprint. Within these constraints, our objective was to observe, if possible, weather dynamics reflected in the FI images.

The 37 GHz sequence beginning on September 16 (Figure 10 and Table 1) shows the moist area associated with the Missouri River, Sakakawea and Devils Lakes in ND, and the Missouri River and Lake Oahe in SD. Rain during the night of September 21 appears as a regional darkening of the 37 GHz image for midnight on the 22nd. Note that the rain is not picked up in the FI image.

The October sequence (Figure 11) is dominated by a cold front passing through the area from the northwest with rain and snow beginning on October 19. The region is warmer and drier by the 26th. The moisture pattern dominates the 37 GHz image, but only the apparent freeze pattern, which generally lags the cold front, is shown in the FI image. Note that strong freeze indications follow the cold front but weaken in the south with warming on the 26th.

The December sequence (Figure 12) is characterized by cold temperatures and snow from December 2 through December 5, followed by daytime warming into the 40s (and even 58^{o} at Rapid City, SD) by the 9th. The FI images reflect this general coldness, but also show daytime thawing toward the end of the period.

Accomplishments and Open Items

Freeze Indicator images based upon a preliminary, 2-parameter discriminant--37 GHz radiobrightness and 10.7, 18, and 37 GHz spectral gradient--show relatively good correlation with the expected state of moisture in northern Great Plains soils during the Fall of 1984. The discriminant is preliminary in the sense that experimental testing of theoretical models needs to be done to fully understand the spectral radiobrightness signatures of frozen soils. The concept underlying the preliminary discriminant is that frozen soil will exhibit volume scatter darkening at shorter microwave wavelengths much like the effect observed in dry snow. Few other phenomena cause negative microwave spectral gradients. One such phenomenon is diurnal insolation which should cause negative spectral gradients at midnight, but positive spectral gradients at noon. We have modeled diurnal insolation and are in the process of tailoring our discriminant to allow for diurnal gradients.

Freeze Indicator images based upon SMMR data effectively map temporal variations in the freeze/thaw pattern for the northern Great Plains at the time scale of days. These patterns are synchronized with weather patterns, but are not identical. We intend to expand our test data set to include several complete seasons. The product would be, in essence, a movie of freeze/thaw patterns as weather fronts sweep through the Great Plains throughout several seasons. The development of these data from SMMR archives should provide one aspect of hydrologic and mesoscale climatic baselines for the region.

The one significant objective of our initial project that has not been achieved is the incorporation of the frozen/thawed soil classification map into regional climate climate models. Such classification maps represent new boundary parameters that are not a part of current models. A very high priority of the new investigation is to explore how this freeze/thaw parameter should be incorporated.

Ancillary to the scientific achievements, but, nevertheless, extremely important to this investigation, and to continuing freeze/thaw investigations, are the computational and image manipulation tools that have been developed within the Radiation Laboratory partly as a result of this project. The primary computational tool is the Fortran coded model for the spectral radiobrightness of periodically heated, two-phase media (England, 1989). This model guided our

examination of SMMR's spectral response of soil to freezing and thawing, and to diurnal insolation. Our image processing tools have evolved from resampling and classification algorithms on a general use, Apollo system, to a dedicated image processing system resident in a Sun/4 Workstation. The Sun/4 system includes two commercial, image processing software packages, and peripherals for reading tapes (and, shortly, CD's), digitizing maps and images, and printing color images to film and to paper.

Year 1984	Site	Air Temp (°F) 00	12	Cloud Cover (x/10) 00	12	Precip. (in.) 00	12	24h	Rem	Snow Pack (in.) 24h
9/15	Aberdeen	40	63	2	3	0	0	0		0
	Bismark	39	64	0	0	0	0	0		0
	Fargo	46	63	8	0	0	0	T		0
	Huron	44	64	0	3	0	0	0		0
	Miles City	50	65	2	2	0	0	0		0
	Rapid City	44	63	4	2	0	0	0		0
	Williston	48	60	6	0	0	0	0		0
9/16	Aberdeen	46	65	1	3	0	0	0		0
	Bismark	53	67	0	2	0	0	0		0
	Fargo	47	69	0	0	0	0	0		0
	Huron	50	64	5	10	0	0	0		0
	Miles City	58	74	0	3	-	-	0		0
	Rapid City	52	70	3	6	0	0	0		0
	Williston	55	68	0	3	0	0	0		0
9/17	Aberdeen	57	71	2	8	0	0	0		0
	Bismark	56	83	0	1	0	0	0		0
	Fargo	57	73	0	3	0	0	0		0
	Huron	58	73	10	3	0	0	0		0
	Miles City	61	80	0	0	-	-	0		0
	Rapid City	64	84	0	0	0	0	0		0
	Williston	56	74	0	3	0	0	0		0
9/18	Aberdeen	64	81	0	0	0	0	0		0
	Bismark	57	80	0	0	0	0	0		0
	Fargo	64	81	0	0	0	0	0		0
	Huron	62	84	0	0	0	0	0		0
	Miles City	60	80	0	0	-	-	0		0
	Rapid City	63	90	0	0	0	0	0		0
	Williston	67	73	0	0	0	0	0		0
9/19	Aberdeen	59	84	0	1	0	0	0		0
	Bismark	55	86	0	0	0	0	0		0
	Fargo	65	90	0	0	0	0	0		0
	Huron	68	90	0	0	0	0	0		0
	Miles City	67	76	0	0	-	-	0		0
	Rapid City	60	90	0	0	0	0	0		0
	Williston	57	72	0	0	0	0	0		0
9/20	Aberdeen	62	65	0	9	0	0	0		0
	Bismark	58	63	0	9	0	0	0		0
	Fargo	54	62	0	6	0	0	0		0
	Huron	62	71	0	2	0	0	0		0
	Miles City	63	72	7	2	-	-	T		0
	Rapid City	59	67	2	6	0	0	0		0
	Williston	54	51	8	9	0	.01	0.15	(R)	0
9/21	Aberdeen	59	82	2	2	0	0	0.1		0
	Bismark	58	81	8	7	0	0	0.3	(R)	0
	Fargo	59	77	10	9	0	0	0		0
	Huron	60	83	0	0	0	0	0		0
	Miles City	66	56	10	10	-	-	0.18	(R)	0
	Rapid City	60	83	2	1	0	0	0.07	(R)	0
	Williston	57	54	10	10	.02	.01	0.3	(R)	0
9/22	Aberdeen	61	65	8	2	T	0	T		0
	Bismark	52	60	3	1	0	0	0		0
	Fargo	72	66	9	0	T	0	0.02		0
	Huron	66	66	10	2	.05	0	.011	(R)	0
	Miles City	46	52	4	6	-	-	0		0
	Rapid City	45	60	3	4	0	0	0		0
	Williston	45	44	10	9	0	0	0		0

Year 1984	Site	Air Temp (°F) 00	12	Cloud Cover (x/10) 00	12	Precip. (in.) 00	12	24h	Rem	Snow Pack (in.) 24h
10/19	Aberdeen	37	44	10	8	.01	0	.1	(R)	0
	Bismark	36	40	10	10	0	0	.04	(S)	0
	Fargo	40	38	10	10	.07	0.2	.77	(R)	0
	Huron	38	45	10	7	0.1	0	.01		0
	Miles City	28	39	7	4	-	-	T		0
	Rapid City	26	42	2	7	0	T	T		T
	Williston	27	34	2	10	-	-	.1	(S)	0
10/20	Aberdeen	36	44	-	10	0	0	T		0
	Bismark	35	38	9	10	T	.01	.1	(R)	0
	Fargo	37	42	10	10	T	.01	.12	(R)	0
	Huron	35	41	0	10	0	0	T		0
	Miles City	31	33	10	10	-	-	.01	(S)	0
	Rapid City	26	43	0	0	0	0	T	(S)	0
	Williston	33	33	10	10	.02	0	.08	(S)	T
10/21	Aberdeen	37	41	-	10	0	0	T		0
	Bismark	36	37	10	10	0	0	.03	(S)	0
	Fargo	38	39	10	9	0	T	.07	(R)	0
	Huron	35	44	2	6	0	0	T		0
	Miles City	29	32	8	9	-	-	T		T
	Rapid City	33	38	10	10	T	0	T	(S)	T
	Williston	32	33	10	9	.01	0	T	(S)	T
10/22	Aberdeen	34	41	7	8	0	0	T		T
	Bismark	33	39	10	8	0	0	0		T
	Fargo	36	38	10	10	T	0	T		0
	Huron	31	42	0	3	0	0	0		0
	Miles City	25	38	0	7	-	-	0		0
	Rapid City	24	43	3	8	0	0	0		0
	Williston	27	32	7	10	0	T	T	(S)	0
10/23	Aberdeen	35	46	10	4	0	0	0		0
	Bismark	36	43	10	3	0	0	0		0
	Fargo	34	39	10	10	0	0	0		0
	Huron	32	46	3	5	0	0	0		0
	Miles City	23	37	1	0	-	-	0		0
	Rapid City	29	42	0	0	0	0	0		0
	Williston	27	40	10	0	0	0	0		0
10/24	Aberdeen	31	54	0	4	0	0	0		0
	Bismark	33	48	0	7	0	0	0		0
	Fargo	33	49	0	8	0	0	0		0
	Huron	36	57	0	1	0	0	0		0
	Miles City	35	44	5	10	-	-	0		0
	Rapid City	36	57	0	3	0	0	0		0
	Williston	30	42	5	7	0	0	T		0
10/25	Aberdeen	38	37	10	10	0	0	0		0
	Bismark	34	39	10	10	0	0	0		0
	Fargo	38	42	10	10	0	0	0		0
	Huron	43	40	8	10	0	0	0		0
	Miles City	33	44	10	10	-	-	T		0
	Rapid City	34	54	1	1	0	0	0		0
	Williston	30	42	10	10	T	0	T		0
10/26	Aberdeen	46	56	0	4	0	0	0		0
	Bismark	41	57	3	10	0	0	0		0
	Fargo	43	53	0	7	0	0	0		0
	Huron	46	61	0	0	0	0	0		0
	Miles City	44	52	0	10	-	-	T		0
	Rapid City	53	65	0	5	0	0	0		0
	Williston	39	50	6	10	0	0	T	(R)	0

Year 1984	Site	Air Temp (°F) 00	Air Temp (°F) 12	Cloud Cover (x/10) 00	Cloud Cover (x/10) 12	Precip. (in.) 00	Precip. (in.) 12	Precip. (in.) 24h	Precip. (in.) Rem	Snow Pack (in.) 24h
12/2	Aberdeen	17	10	10	4	T	0	T	(S)	2
	Bismark	14	19	10	10	T	T	.01	(S)	1
	Fargo	8	3	10	10	T	T	T	(S)	T
	Huron	19	14	10	1	.01	T	.07	(S)	6
	Miles City	13	11	10	9	-	-	.01	(S)	4
	Rapid City	19	19	4	4	0	0	T	(S)	T
	Williston	11	8	10	8	T	0	T	(S)	1
12/3	Aberdeen	4	17	0	4	0	0	T	(S)	2
	Bismark	15	15	10	7	T	T	T	(S)	1
	Fargo	0	10	0	0	0	T	0.1		T
	Huron	5	14	0	0	0	0		T(S)	6
	Miles City	-3	-2	10	1	-	-	0		4
	Rapid City	11	27	0	1	0	0	0		T
	Williston	9	9	10	8	T	T	T	(S)	1
12/4	Aberdeen	13	10	10	0	0	0	0.02	(S)	2
	Bismark	8	15	10	1	T	0	T		1
	Fargo	9	15	10	0	0	0	0		T
	Huron	5	12	6	2	T	0	T	(S)	5
	Miles City	-1	7	0	10	-	-	0		4
	Rapid City	15	24	2	0	0	0	0		T
	Williston	-5	10	0	10	0	0	0		1
12/5	Aberdeen	14	7	3	5	T	0	T	(S)	2
	Bismark	19	-1	4	0	0	0	T	(S)	1
	Fargo	11	-1	10	10	0	0	T	(S)	T
	Huron	15	15	4	7	0	T	T		4
	Miles City	24	13	10	10	-	-	T	(S)	3
	Rapid City	26	19	8	7	0	T	T	(S)	T
	Williston	8	-5	3	3	T	0	T	(S)	1
12/6	Aberdeen	-14	3	0	0	0	0	0		2
	Bismark	-11	20	0	8	0	0	T		1
	Fargo	-8	8	0	3	0	0	0		T
	Huron	-6	11	0	4	0	0	0		4
	Miles City	9	23	0	9	-	-	0		3
	Rapid City	6	44	1	1	0	0	0		T
	Williston	-7	24	0	9	0	0	T		1
12/7	Aberdeen	18	42	7	4	0	0	0		2
	Bismark	30	43	9	8	0	0	0		1
	Fargo	12	43	7	9	0	0	0		T
	Huron	19	42	3	0	0	0	0		3
	Miles City	35	44	4	0	-	-	0		2
	Rapid City	43	61	10	0	0	0	0		0
	Williston	34	43	3	6	0	0	0		1
12/8	Aberdeen	30	36	2	3	0	0	0		T
	Bismark	31	42	7	2	0	0	0		T
	Fargo	30	43	2	5	0	0	0		0
	Huron	31	42	0	4	0	0	0		1
	Miles City	29	33	3	3	-	-	0		1
	Rapid City	33	51	0	10	0	0	0		0
	Williston	31	37	7	8	0	0	0		T
12/9	Aberdeen	-	46	-	7	0	0	0		T
	Bismark	31	43	2	3	0	0	0		T
	Fargo	29	40	0	9	0	0	0		0
	Huron	35	39	7	7	0	0	0		T
	Miles City	26	35	5	4	-	-	0		1
	Rapid City	43	58	6	0	0	0	0		0
	Williston	28	37	0	2	0	0	0		0

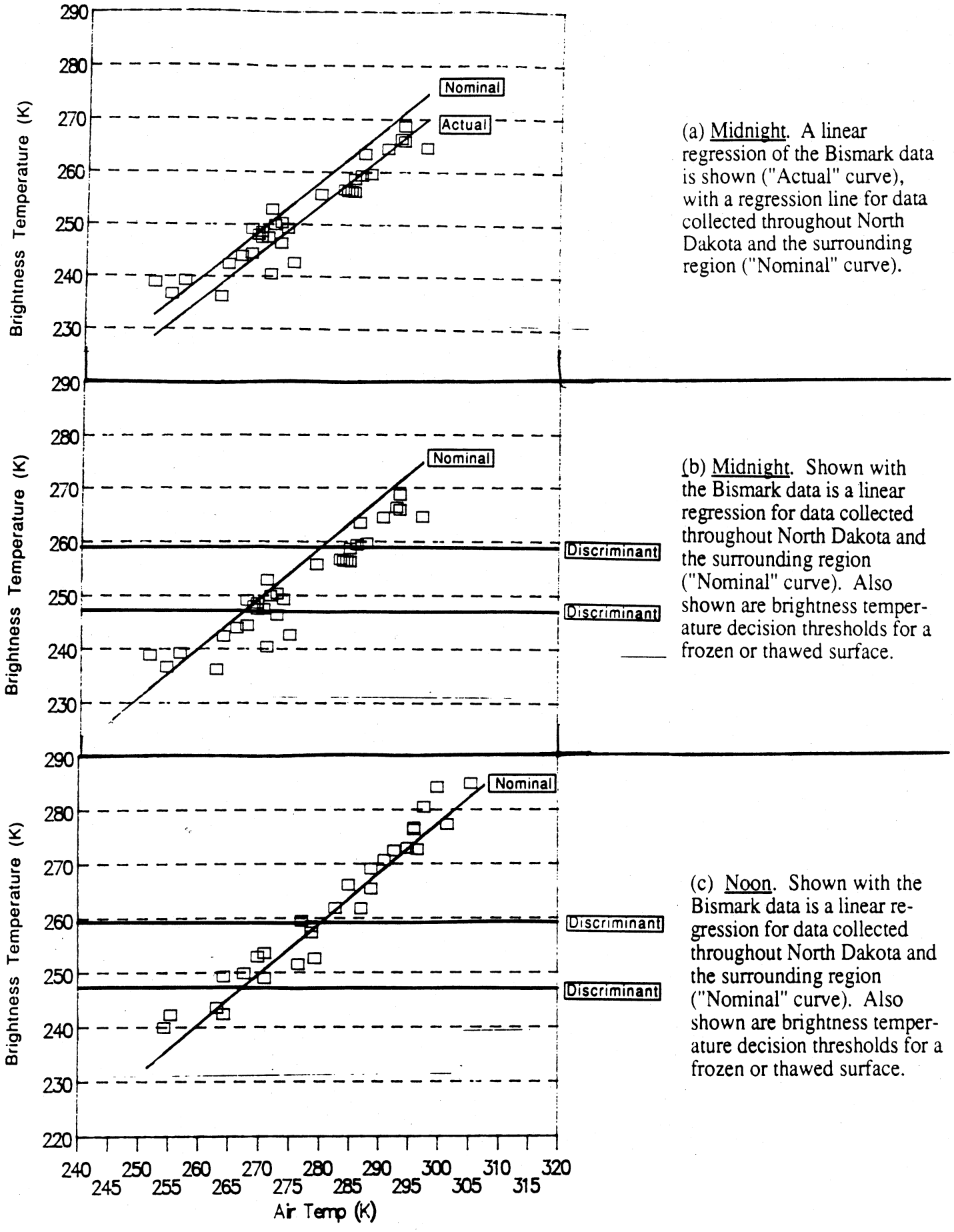

(a) Midnight. A linear regression of the Bismark data is shown ("Actual" curve), with a regression line for data collected throughout North Dakota and the surrounding region ("Nominal" curve).

(b) Midnight. Shown with the Bismark data is a linear regression for data collected throughout North Dakota and the surrounding region ("Nominal" curve). Also shown are brightness temperature decision thresholds for a frozen or thawed surface.

(c) Noon. Shown with the Bismark data is a linear regression for data collected throughout North Dakota and the surrounding region ("Nominal" curve). Also shown are brightness temperature decision thresholds for a frozen or thawed surface.

Figure 1. 37 GHz SMMR brightness temperature versus measured surface air temperature, Bismark, North Dakota. Data were collected from 8/1/84 to 12/31/84.

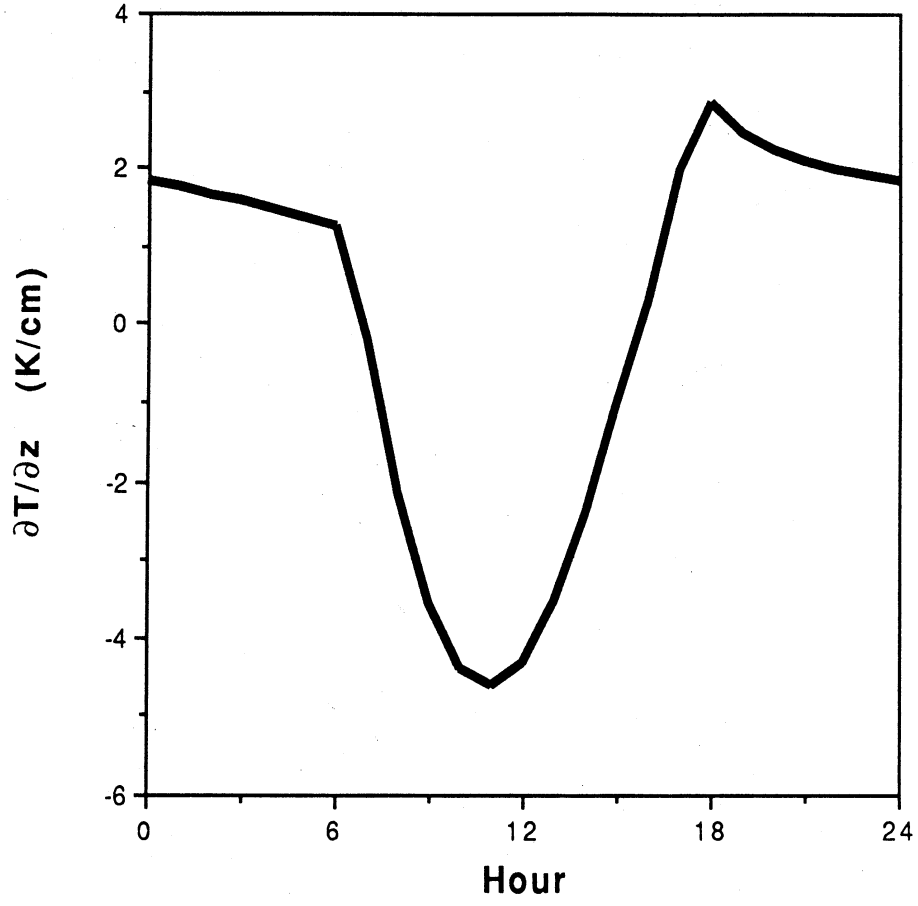

Figure 2. Soil surface thermal gradient. Computed for 10% moist soil at Bismarck, ND, for a standard day in September.

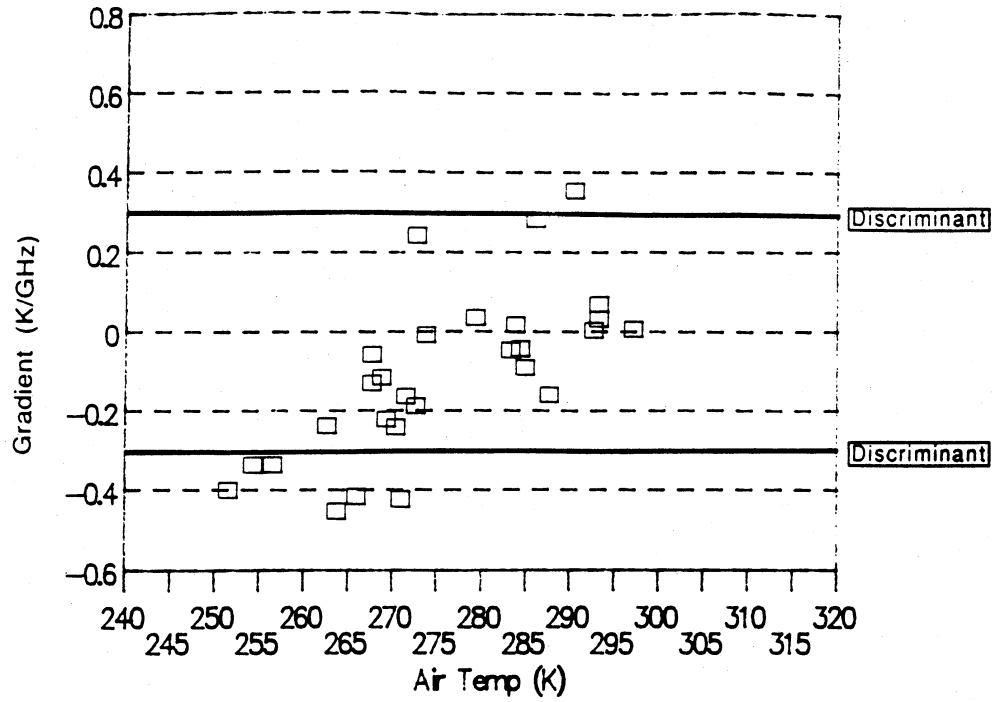

(a) Midnight

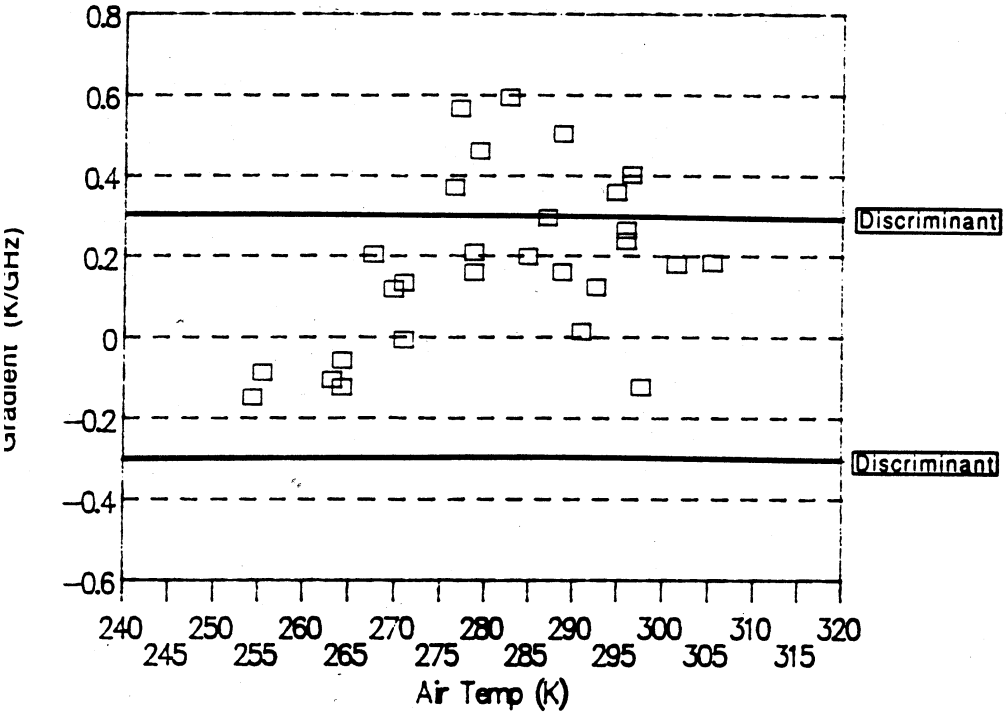

(b) Noon

Figure 3. Frequency gradient versus measured surface air temperature, Bismark, North Dakota. Data were collected from 8/1/84 to 12/31/84. The frequency gradient is the frequency regression slope for simultaneous SMMR brightness temperatures at 37GHz, 18 GHz, and 10.7 GHz. Shown with the Bismark data are frequency gradient decision thresholds for a frozen or thawed surface.

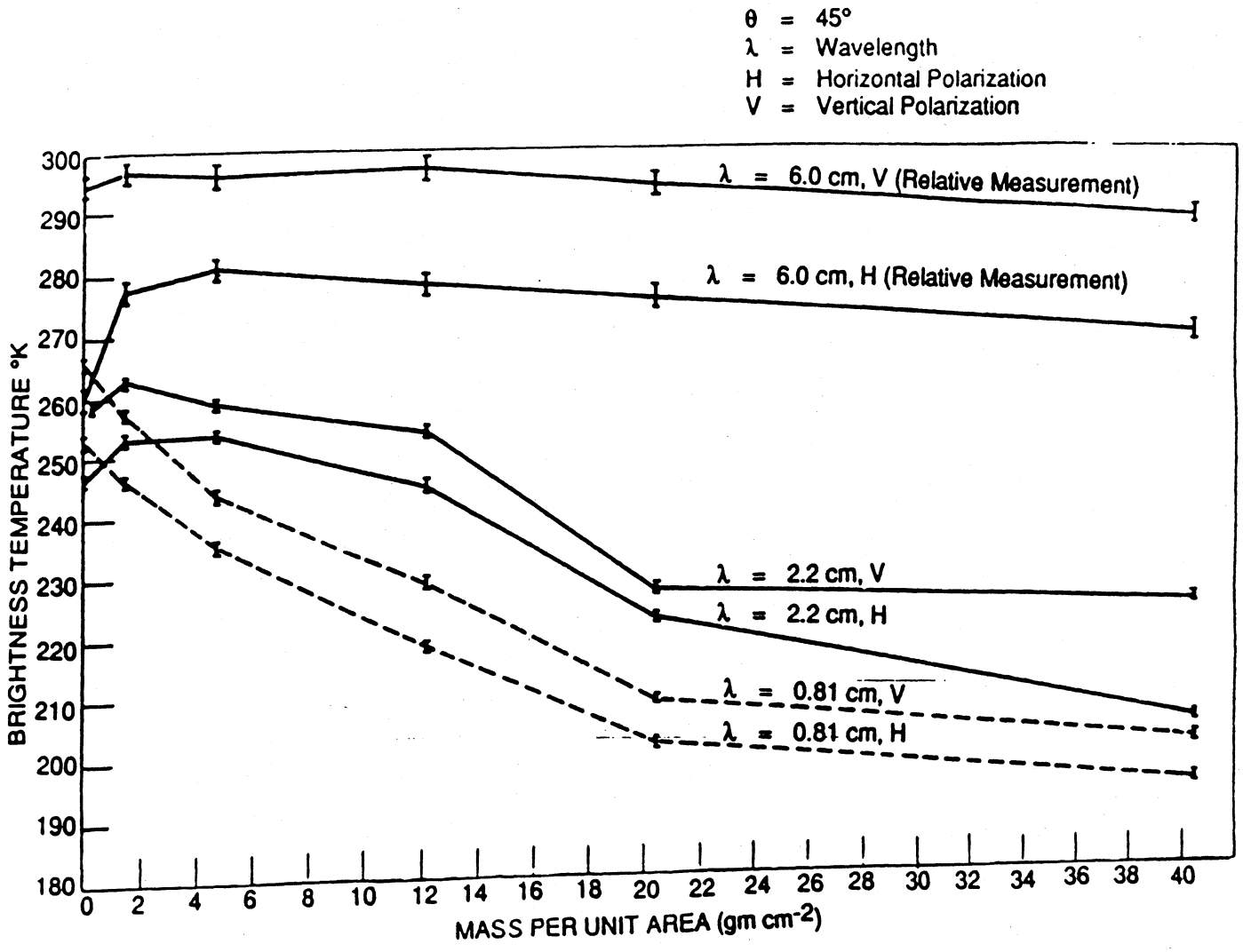

Figure 4. Brightness temperature versus equivalent dry snow, Crater Lake, Oregon, 22 March 1970 (Edgerton et al., 1971). Note the short wavelength darkening evident for thick snowpacks.

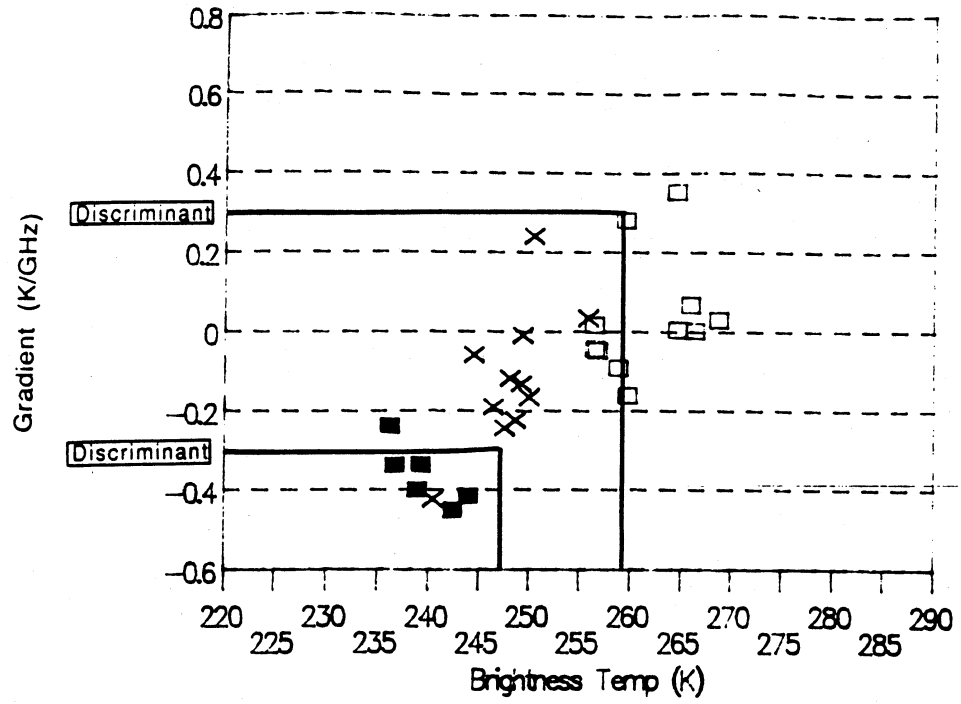

(a) Midnight

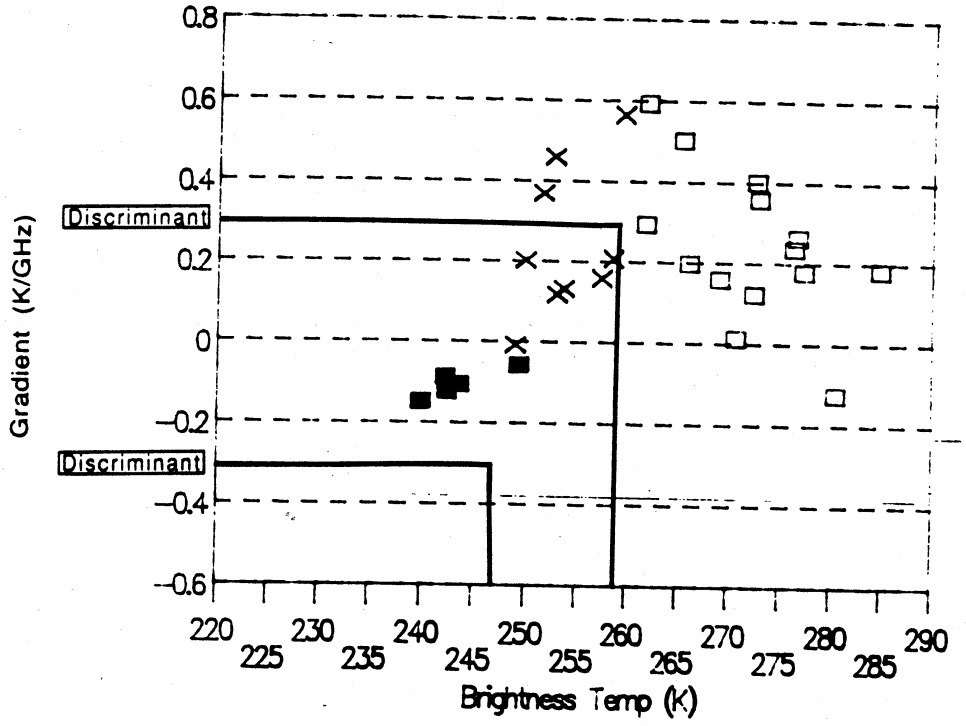

(b) Noon

Figure 5. Frequency gradient versus SMMR 37 GHz brightness temperature, Bismark, North Dakota. Data were collected from 8/1/84 to 12/31/84. Shown with the Bismark data are clustering decision thresholds for a frozen, mixed, or thawed surface. Based upon ground truth, the solid boxes are frozen, open boxes are thawed, and x's are mixed pixels.

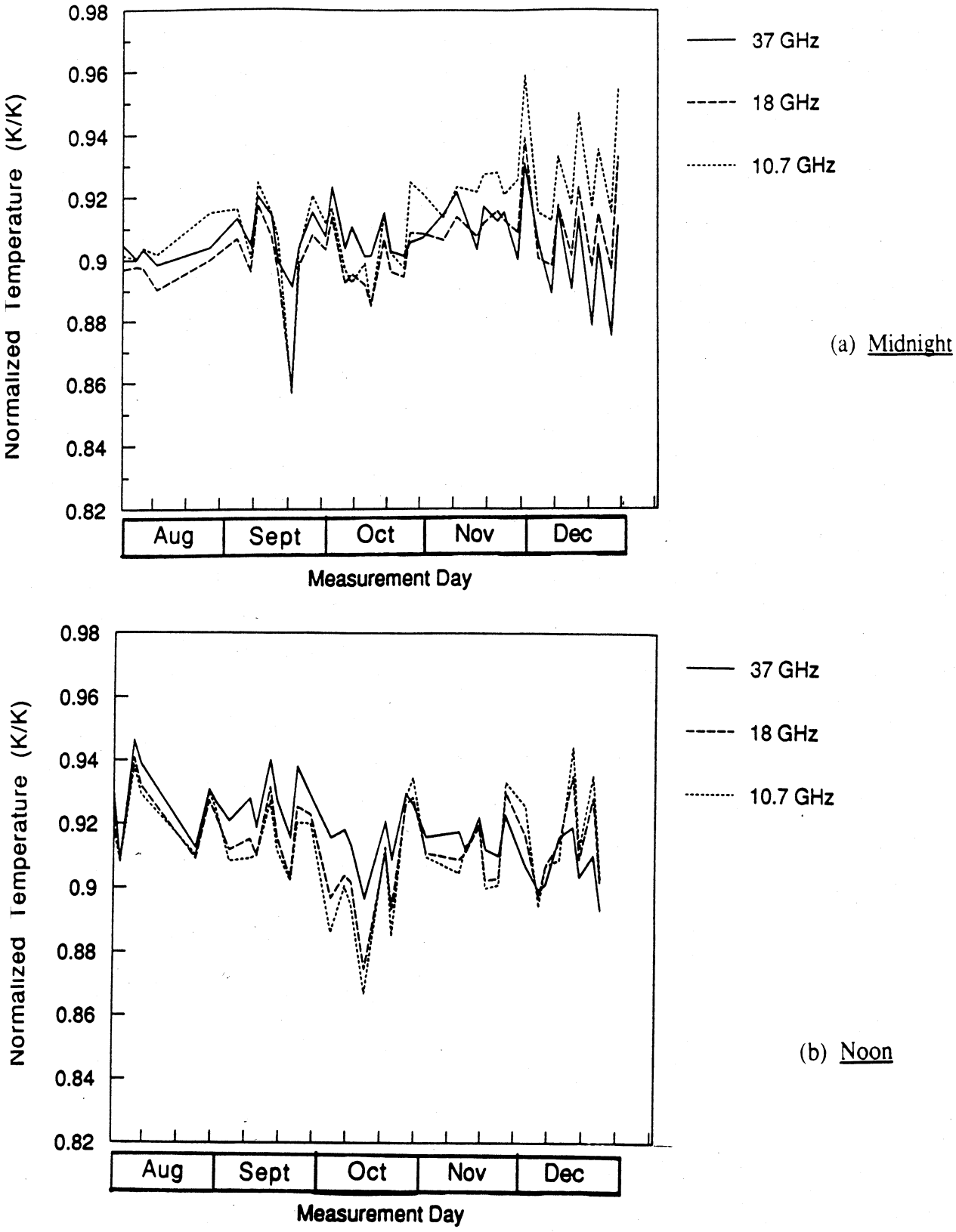

Figure 6. 37 GHz, 18 GHz, and 10.7 GHz SMMR normalized brightness temperatures versus calender day. Measurements were made at irregular intervals from 8/1/84 to 12/31/84. The normalized brightness temperature of a single SMMR frequency channel is the average brightness divided by the average surface air temperature, averages are calculated over North Dakota and the surrounding region.

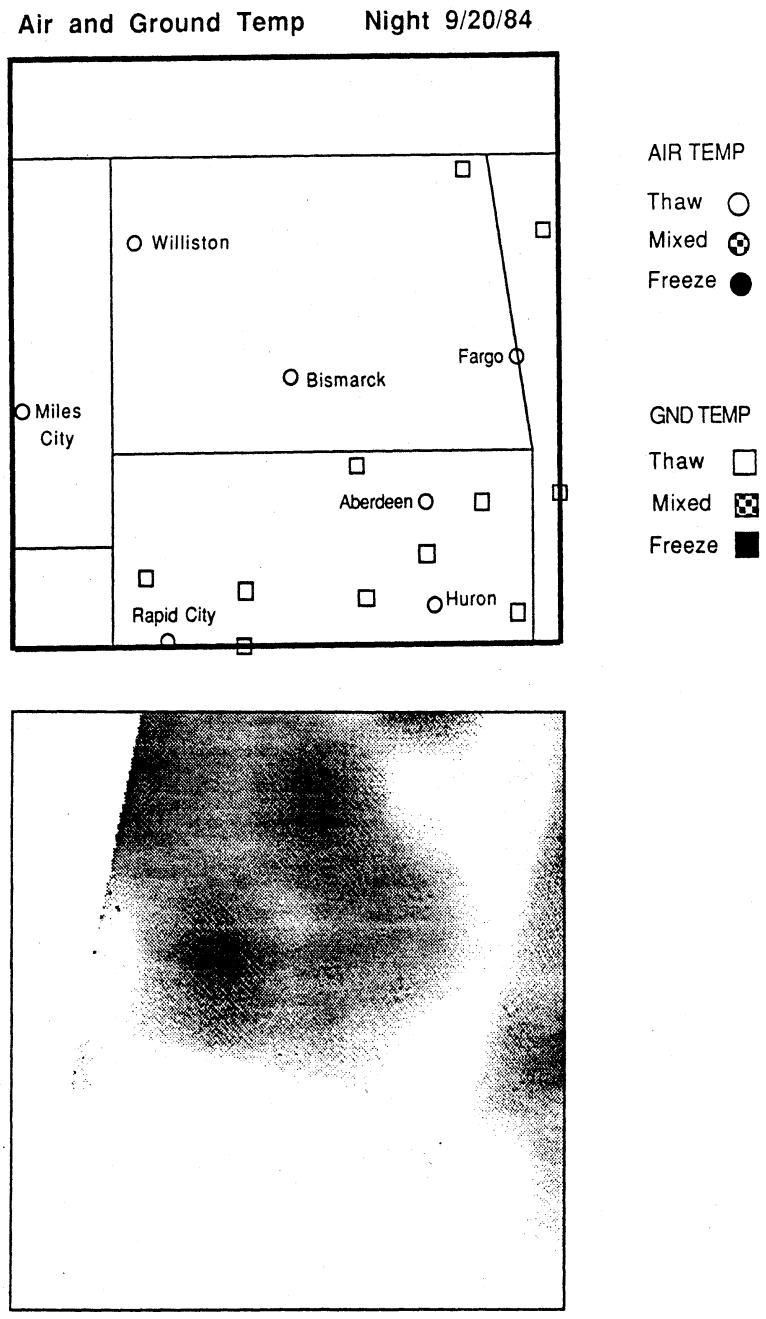

Figure 7. A comparison of reported air and ground temperatures with the Freeze Indicator for midnight, September 20, 1984.

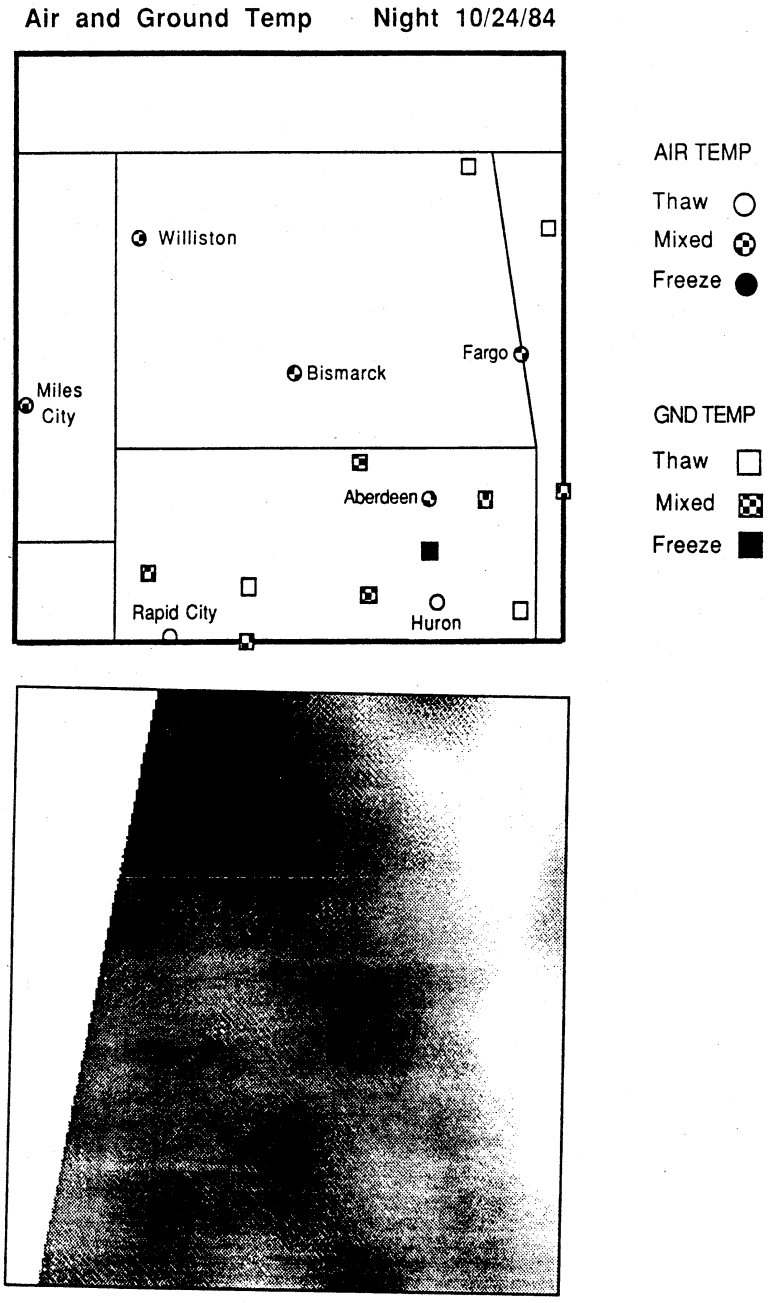

Figure 8. A comparison of reported air and ground temperatures with the Freeze Indicator for midnight, October 24, 1984.

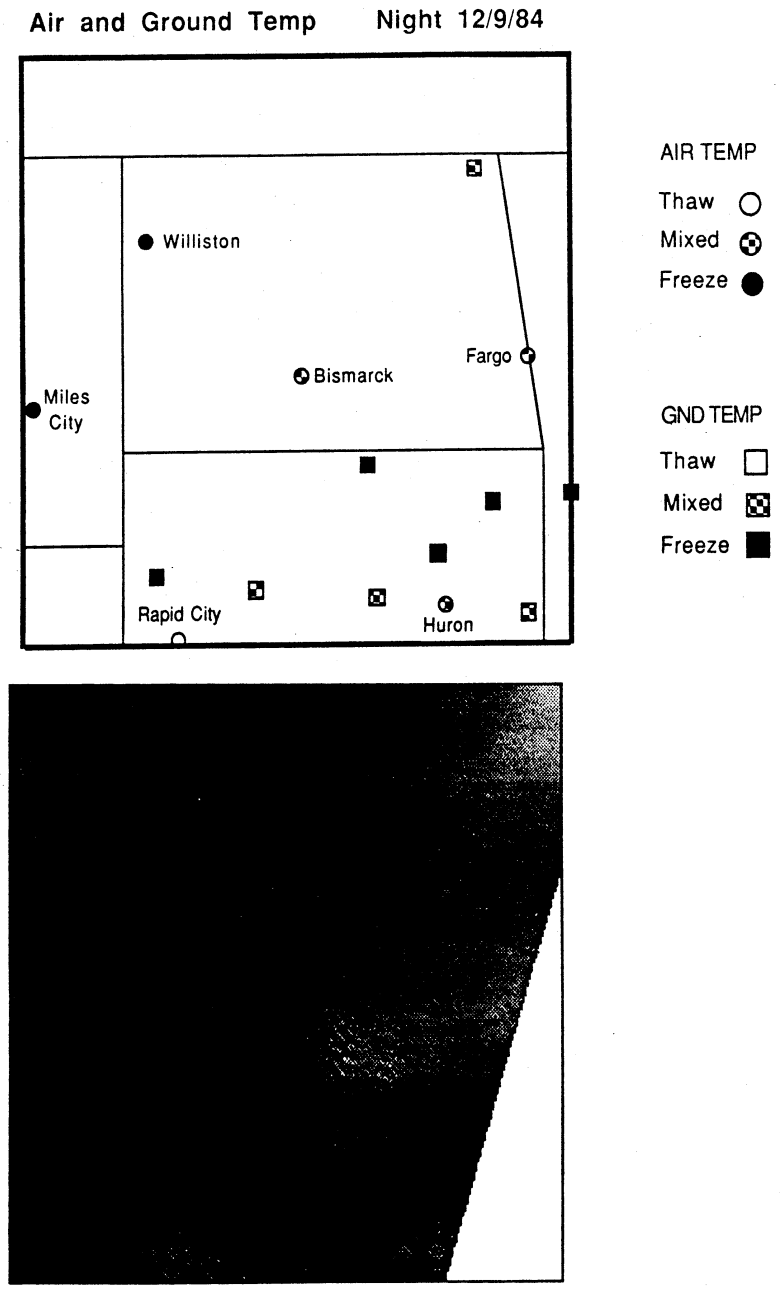

Figure 9. A comparison of reported air and ground temperatures with the Freeze Indicator for midnight, December 9, 1984.

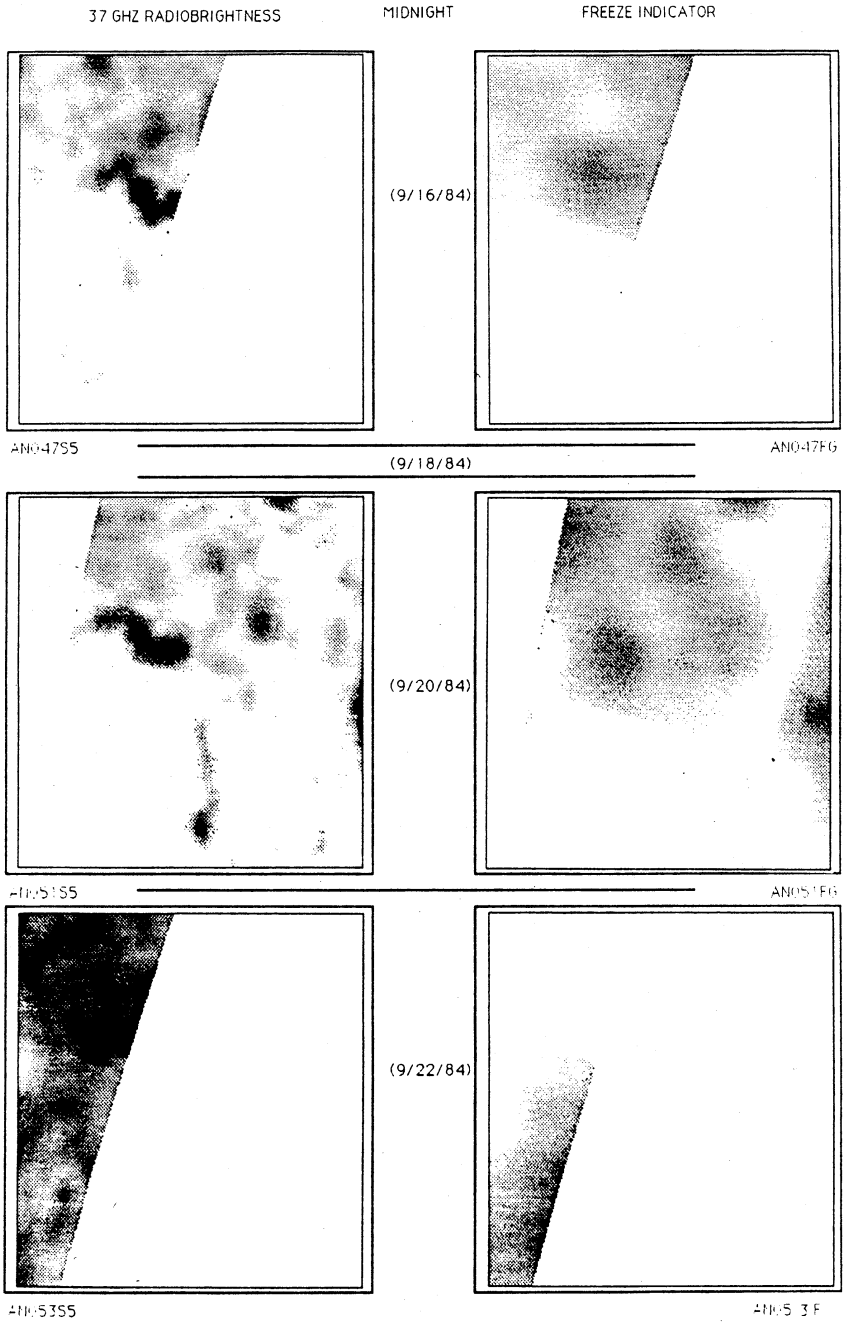

Figure 10(a). Midnight 37 GHz and Freeze Indicator image sequences for a 6 day period in September.

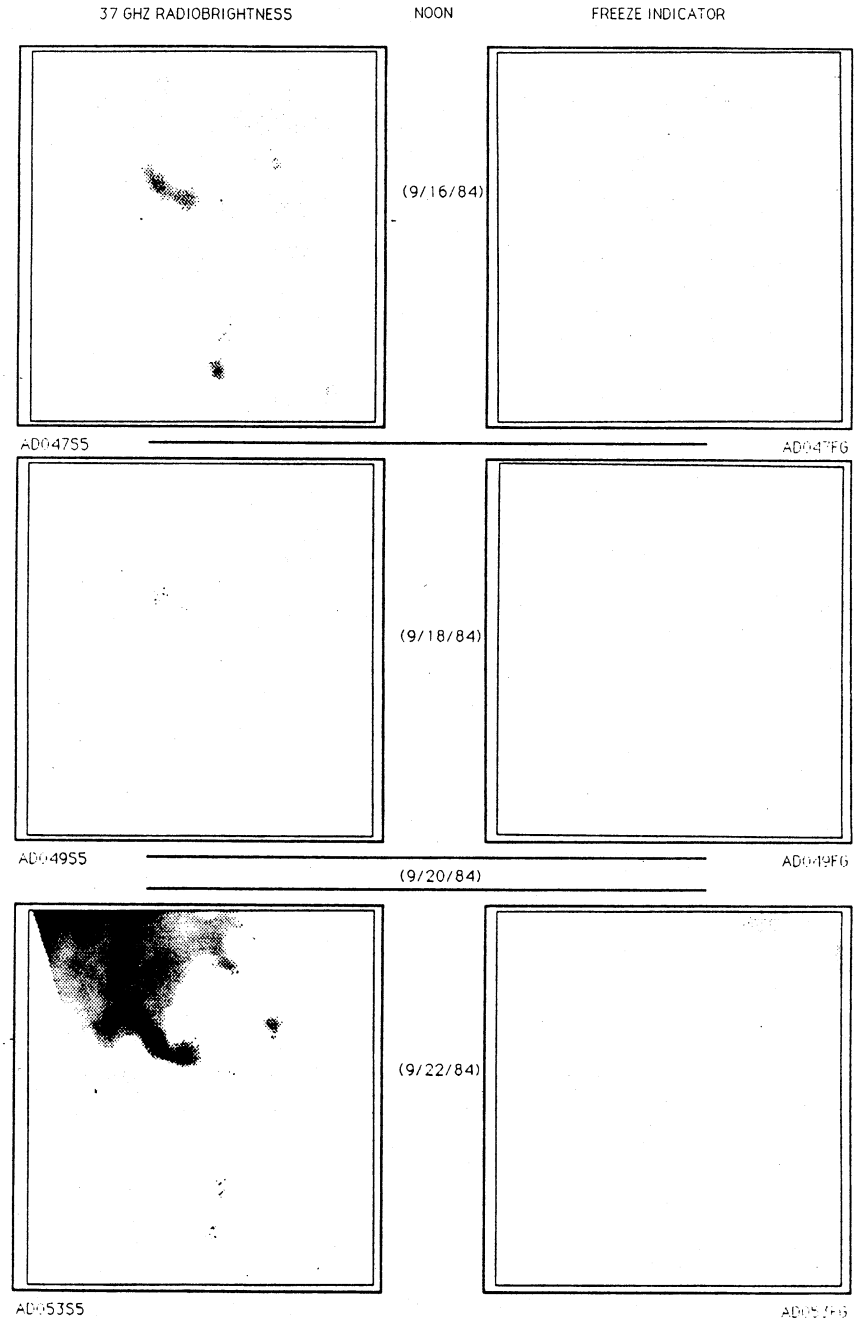

Figure 10(b). Noon 37 GHz and Freeze Indicator image sequences for a 6 day period in September.

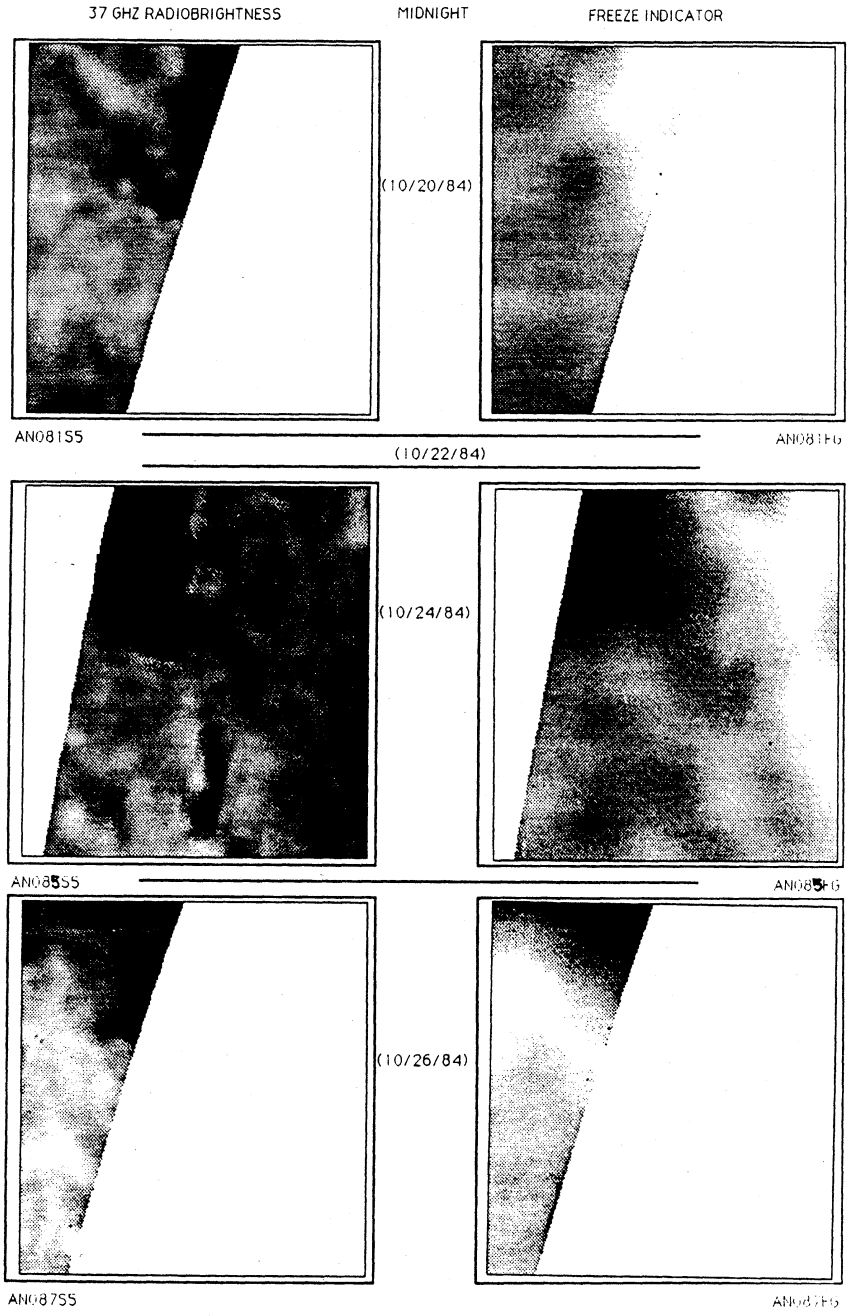

Figure 11(a). Midnight 37 GHz and Freeze Indicator image sequences for a 6 day period in October.

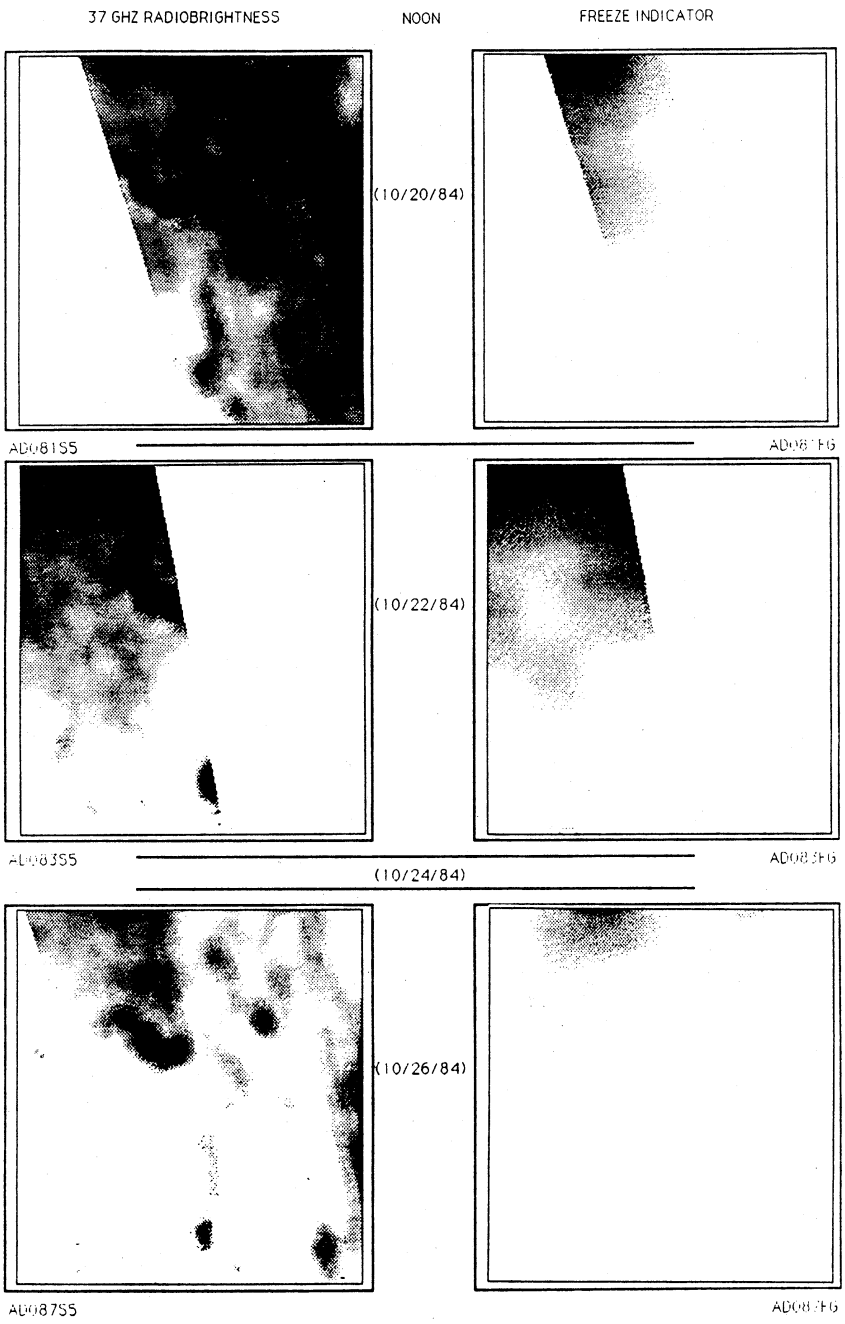

Figure 11(b) Noon 37 GHz and Freeze Indicator image sequences for a 6 day period in October.

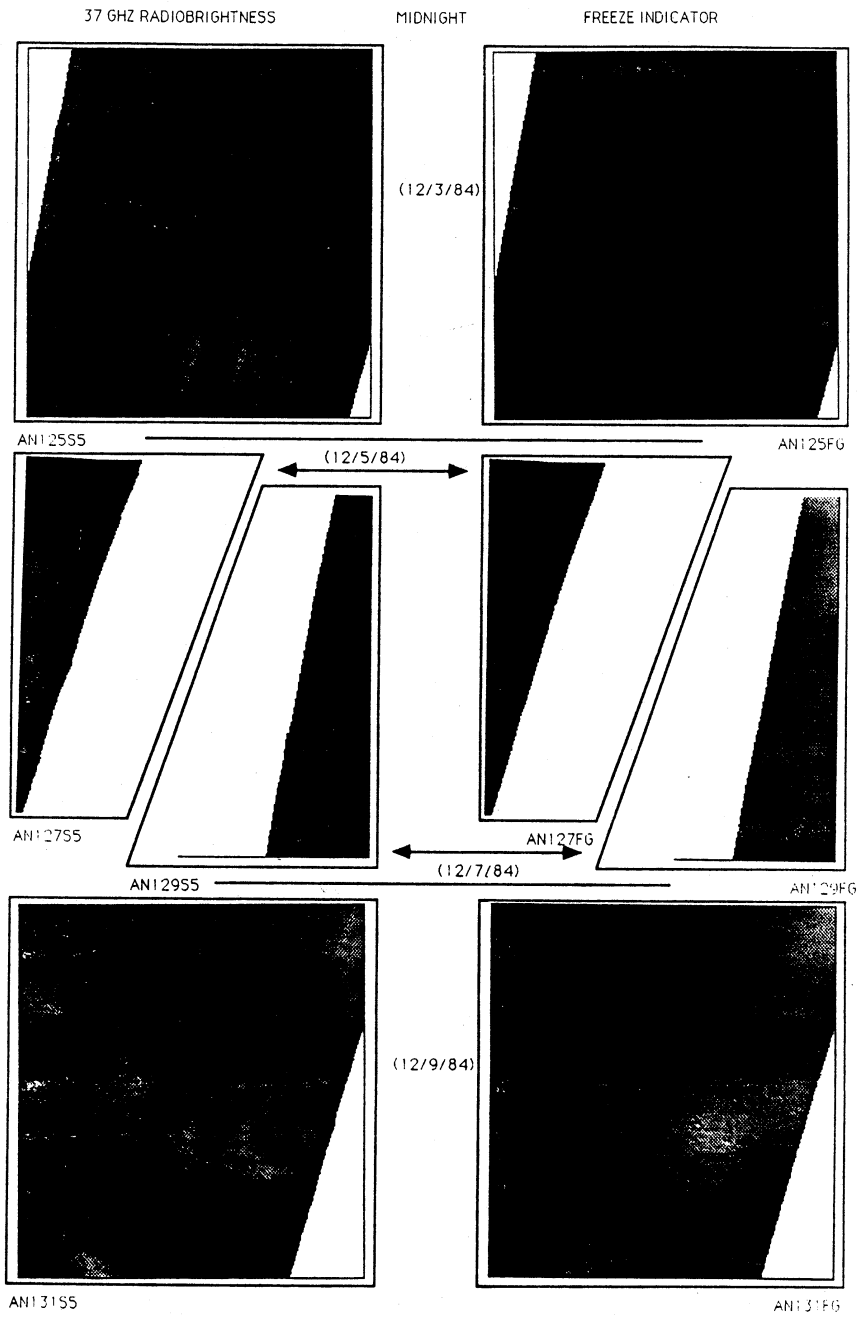

Figure 12(a) Midnight 37GHz and Freeze Indicator image sequences for a 6 day period in December.

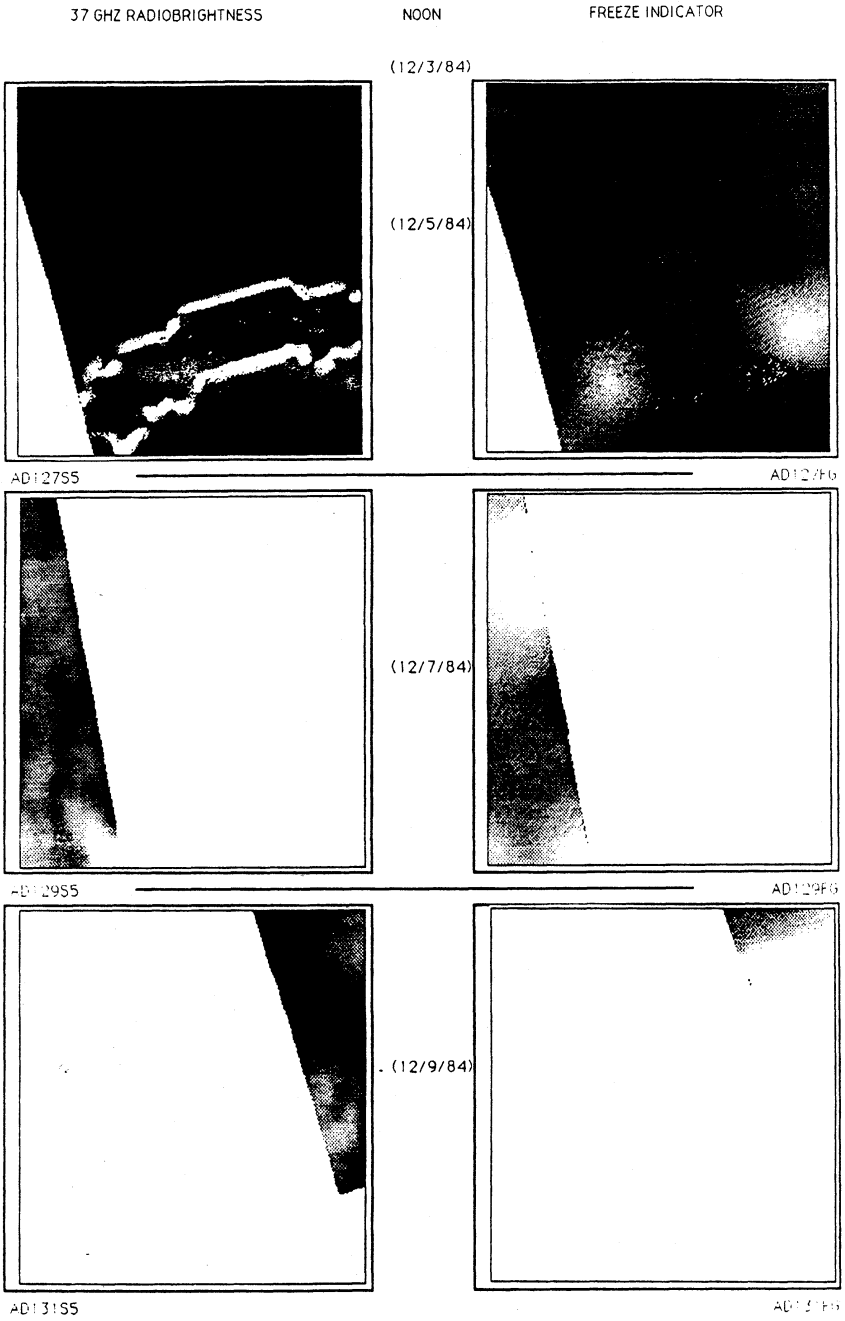

Figure 12(b) Noon 37GHz and Freeze Indicator image sequences for a 6 day period in December. The jagged white lines in the Noon, 12/5/84, image are caused by missing data.

IV References

Burke, W.J., T. Schmugge, and J.F. Paris, 1979, Comparison of 2.8- and 21-cm microwave radiometer observations over soils with emission model calculations, JGR 84, p. 287-294.

Camillo, P.J., and T.J. Schmugge, 1984, Correlating rainfall with remotely sensed microwave radiation using physically based models, IEEE Trans. on Geosc. and Rem. Sens. GE-22, p. 415-423.

Edgerton, A.T., A. Stogryn, and G. Poe, 1971, Microwave Radiometric Investigations of Snowpacks, Final Rept. 1285R-4 of Contract 14-08-001-11828 between Aerojet-General Corp., El Monte, CA, and the U.S. Geological Survey.

England, A.W., 1974, The effect upon microwave emissivity of volume scattering in snow, in ice, and in frozen soil, Proc. URSI Spec Mtg on Microwave Scattering and Emission from the Earth, Berne, Switzerland, 23-26 Sept., 1974.

England, A.W., 1975, Thermal microwave emission from a scattering layer, JGR 80, p. 4484-4496.

England, A.W., 1976, Relative influence upon microwave emissivity of fine-scale stratigraphy, internal scattering, and dielectric properties, Pageoph 114, p. 287-299.

England, A.W., 1977, Microwave brightness spectra of layered media, Geophysics 42, p. 514-521.

England, A.W., 1989, Radiobrightness of diurnally heated, freezing soil, IEEE Geoscience and Remote Sensing, in press.

Hoekstra, P., and A. Delaney, 1974, Dielectric properties of soils at UHF and microwave frequencies, JGR 79, pp.1699-1708.

Moik, J., 1980, Digital Processing of Remotely Sensed Images, NASA SP-431.

Schmugge, T.J., 1983, Remote sensing of soil moisture: Recent advances, IEEE Trans. on Geosc. and Rem. Sens. GE-21, p. 336-344.

Schmugge, T.J., 1987, Remote sensing applications in hydrology, Rev. Geophys. 25, p. 148-152.

Schmugge, T.J., P.E. O'Neill, and J.R. Wang, 1986, Passive microwave soil moisture research, IEEE Trans. on Geosc. and Rem. Sens. GE-24, p. 12-22.

Ulaby, F.T., R.K. Moore, and A.K. Fung, 1981, Microwave Remote Sensing, Active and Passive, Addison-Wesley, p. 186-255.

Wang, J.R., T.J. Schmugge, W.I. Gould, W.S. Glazar, and J.E. Fuchs, 1982, A multi-frequency radiometric measurement of soil moisture content over bare and vegetated fields, Geophys. Res. Let. 9, p. 416-419.

Zuerndorfer, B., A.W. England, C. Dobson, and F.T. Ulaby, 1989a, Mapping freeze/thaw boundaries with SMMR data, J. of Agriculture and Forest Meteorology, in press.

Zuerndorfer, B., A.W. England, and G.H. Wakefield, 1989b, The radiobrightness of freezing terrain, Proc. of IGARSS '89, Vancouver, B.C., July 10-14, 1989, p. 2748-2751.

Radiobrightness of Diurnally Heated, Freezing Soil

A. W. England

Radiation Laboratory

Department of Electrical Engineering

and Computer Science

The University of Michigan

Ann Arbor, MI 48109-2122

August 15, 1989

Abstract

Freezing and thawing soils exhibit unique radiometric characteristics. To examine these characteristics, diurnal insolation is modeled as 1-dimensional heating of a moist soil halfspace during a typical fall at a northern Great Plains site (Bismarck, ND). The 1-dimensional, heat flow equation is non-linear because both the enthalpy and the thermal conductivity of freezing soils are non-linear functions of temperature. The problem is particularly difficult because phase boundaries propagate in time, and because soils that contain clay freeze over a range of temperatures rather than at 0^{o} C--that is, they possess diffuse phase boundaries.

A modified Chernous'ko method was used to integrate the heat flow equation to obtain monthly thermal models during a typical September through December period. Diurnal radiobrightness curves at 10.7, 18, and 37 GHz were computed for each month. The 37 GHz radiobrightness best tracks soil surface temperature, the 10.7-37 GHz spectral gradient of thawed soils is strongly positive, the spectral gradient of frozen soils is slightly negative, and the midnight to noon spectral gradient is shifted by approximately +0.1 K/GHz by diurnal changes in the surface temperature and the thermal gradient. These observations support the use of SMMR's 37 GHz radiobrightness and its 10.7-37 GHz spectral gradient as discriminants in a frozen soil classifier for high latitude prairie.

Introduction

The quantity and state of moisture in soil can be estimated from satellite radiobrightness signatures. There is a large body of literature linking moisture content to radiobrightness [1]-[6]. Whether or not the soil is frozen affects the rate of energy transfer to the atmosphere by limiting evapotranspiration, and affects the rainfall or snowmelt runoff potential by reducing the infiltration capacity of the soil. Zuerndorfer et al. [7] produced freeze/thaw maps of the northern Great Plains

from Nimbus 7 Scanning Multichannel Microwave Radiometer (SMMR) data. This paper is an examination of the theoretical basis for microwave radiometric, frozen soil classification.

Figures 1a and 1b illustrate the observational basis for a frozen soil classifier. A 37 GHz radiobrightness below about 247 K indicates frozen soil, and one above about 247 K indicates thawed soil for Bismarck, ND. However, regions near the Missouri River, Sakakawea and Devils Lakes, the Red River Valley, and in the wakes of a regional rainfall often appear anomalously cold at 37 GHz because of exceptional wetness for the northern Great Plains. The confusing factor is that 37 GHz radiobrightness, while least sensitive to moisture of the SMMR frequencies, is darkened by moisture. A second discriminant -- the 10.7-37 GHz spectral gradient -- resolves the ambiguity because frozen soils are observed to have negative spectral gradients, and moist soils are generally observed to have a positive spectral gradient. Figures 1a and 1b also exhibit an upward shift in the spectral gradient between midnight and noon of about 0.1 K/GHz.

A valid theoretical model should replicate the behavior of the 37 GHz radiobrightness, the dominant characteristics of the 10.7-18-37 GHz spectral gradient, and the diurnal shifts in the spectral gradient during the September through December months in the northern Great Plains. Model parameters will be chosen for prairie near Bismarck, ND.

1-Dimensional Heat Flow

The 1-dimensional heat flow equation for temperature T (Kelvin), depth z (cm), and time t (sec) is [8]

$$\frac{\partial E(T)}{\partial t} = - \frac{\partial F(z,t)}{\partial z} \qquad (1)$$

where E(T) is enthalpy (cal/cm^3) and F(z,t) is heat flux (cal/cm^2-K) (T is a function of z and t). Heat flux is linearly related to the temperature gradient, $\partial T/\partial z$, by

$$F(z,t) = - K(T) \frac{\partial T}{\partial z} \tag{2}$$

where K(T) is thermal conductivity (cal/cm-sec-K). That is,

$$\frac{\partial E(T)}{\partial t} = \frac{\partial}{\partial z}\left(K(T)\frac{\partial T}{\partial z}\right) \tag{3}$$

With respect to a reference temperature, T_o, E(T) is generally the linear function

$$E(T) = \rho\, c_p \{T-T_o\} \tag{4}$$

where ρ is density (gm/cm^3), and c_p is specific heat at constant pressure (cal/gm-K). If K(T) is constant, Equation (3) becomes the parabolic linear differential equation

$$\frac{\partial T}{\partial t} = \kappa \frac{\partial^2 T}{\partial z^2} \tag{5}$$

where constant κ is thermal diffusivity (cm^2/sec)

$$\kappa = \frac{K}{\rho\, c_p} \tag{6}$$

Equation (5) can be solved analytically by either the harmonic or the Laplace methods [8], or by a finite difference numerical method. Watson used the Laplace method [9][10], and Kahle used the finite difference method [11] to develop thermal models for the diurnal insolation of rock and soil. Their models relate day-night differences in thermal infrared temperature to rock and soil type. However, if soils freeze or thaw diurnally, then Equation (3) is not linear and is not amenable to either the Watson or the Kahle methods.

Equation (3) looks simpler with the substitution of variables

$$u = \int_{T_0}^{T} K'(\tau)\, d\tau \tag{7}$$

so that u = u(T) and Equation (3) becomes

$$\frac{\partial E(T)}{\partial t} = \frac{\partial^2 u}{\partial z^2} \tag{8}$$

This 1-dimensional, non-linear, heat flow equation is called Stefan's problem [12], and there are three ways to solve it: The finite difference method [13], the moving boundary method [14], and the isotherm propagation or Chernous'ko method [15]. The finite difference method for non-linear problems suffers from uncertain convergence properties. The moving boundary method involves seeking analytical solutions to the linear regions on either side of moving phase boundaries. This method is particularly awkward if the phase change occurs over a depth zone, as in freezing soils, rather than at a plane interface, or if there are multiple freezing isotherms, as in the periodic heating case. The Chernous'ko method has a problem with the periodic heating case.

Chernous'ko [15] replaced E(T) with the piecewise constant approximation, H(T), (shown schematically in Figure 2a)

$$H(T) = E(T_n) \quad \text{for} \quad T_n \le T < T_{n+1} \tag{9}$$

where T_n denotes isotherm n ordered by increasing depth. While these isotherms can be any temperature, integer values of Kelvin are convenient. The slope of the linear portions of E(T) below 268 K and above 273 K are the ρc_p for frozen and moist soils, respectively. The increased slope between 268 and 273 K results from the latent heat of melting of moisture in the soil (linearity of E(T) in this region is an approximation). In this example, melting occurs over 5 degrees. For sandy soils, the range might be near 1 degree; for some clay soils, it might be more than 10 degrees [16].

In terms of H(T), Equation (9) becomes

$$\frac{\partial H(T)}{\partial t} = \frac{\partial^2 u}{\partial z^2} \tag{10}$$

Locally constant H requires that u be a linear function of z between isotherms T_n and T_{n+1}, i.e.,

$$u = u_n + \frac{u_{n+1}-u_n}{z_{n+1}-z_n}(z - z_n) \tag{11}$$

where z_n is the depth of isotherm T_n.

If the value of H(T) at $z > z_n$ is denoted by H^+, and H(T) at $z < z_n$ is H^-, then Equation (10) can be integrated at constant time along path a-b in Figure 3,

$$\frac{\partial}{\partial t}\int_a^b H(T)\,dz = \left(\frac{\partial u}{\partial z}\right)_{b,t} - \left(\frac{\partial u}{\partial z}\right)_{a,t} \tag{12}$$

to yield

$$\frac{\partial}{\partial t}\left[H^+(b-z_n) + H^-(z_n-a)\right] = \left(\frac{\partial u}{\partial z}\right)_{b,t} - \left(\frac{\partial u}{\partial z}\right)_{a,t} \tag{13}$$

From Equation (11), because z_n is the only function of time on the left of Equation (13),

$$\frac{dz_n}{dt} = \frac{1}{(H^- - H^+)}\left\{\left(\frac{u_{n+1}-u_n}{z_{n+1}-z_n}\right) - \left(\frac{u_n-u_{n-1}}{z_n-z_{n-1}}\right)\right\} \tag{14}$$

Equation (14) is the ordinary, linear differential equation that Chernous'ko used to propagate each isotherm in time.

Equation (14) fails in the periodic heating problem because of an asymmetry in H(T) between heating and cooling. For example, consider the propagation of isotherm z_n where $T_{n-1} < T_n = T_{n+1}$. In this case, $H^+ > H^-$ and

$$\frac{dz_n}{dt} = \frac{-1}{(H^- - H^+)} \left\{ \left(\frac{u_n - u_{n-1}}{z_n - z_{n-1}} \right) \right\} \tag{15}$$

However, if $T_{n-1} > T_n = T_{n+1}$, then $H^+ = H^-$ and dz_n/dz in Equation (14) is undefined. This asymmetry can be ameliorated by substituting the piecewise constant H(T) shown schematically in Figure 2b, i.e.,

$$H(T) = \left\{ \begin{array}{ll} \frac{E(T_n)+E(T_{n+1})}{2} & \text{for } T_n < T < T_{n+1} \\ E(T_n) & \text{for } T = T_n \\ \frac{E(T_{n-1})+E(T_n)}{2} & \text{for } T_{n-1} < T < T_n \end{array} \right\} \tag{16}$$

Isotherm propagation with this alternative approximation for E(T) will be referred to as the modified Chernous'ko method.

Boundary Conditions

Watson [9] and Kahle [11] used boundary conditions for the energy flux, $F_{net}(z)$,

$$F_{net}(0) = F_{sun} + F_{sky} + F_{wind} - F_{ground}$$

$$F_{net}(\infty) = 0 \tag{17}$$

where z = infinity means depths greater than the penetration of the diurnal thermal pulse. The parameters that comprise these boundary conditions for Bismarck, ND, are described in Table 1. F_{sun} is insolation reduced by cloud cover, atmospheric absorption, albedo, and the cosine of the

zenith angle. F_{sky} is sky brightness plus a small correction for cloud cover. F_{wind} is a small correction for sensible heat transfer between ground and air used by Kahle [11]. F_{ground} is gray-body emission from the soil's surface. Topography and evapotranspiration are ignored.

Radiobrightness

Consider thermal microwave emission from volume, dV, within a dielectric halfspace (Fig 4). The energy, dQ, arriving at surface element, dA, is

$$dQ = E\, dV\, e^{-2\beta z/\cos\theta'} \frac{dA}{z/\cos\theta'} \tag{18}$$

where 2β is the power loss coefficient,

$$2\beta = \frac{2\pi\sqrt{\varepsilon'}\tan\delta}{\lambda_o} \tag{19}$$

ε' is the real part of the dielectric constant, $\tan\delta$ is the loss tangent, λ_o is free-space wavelength, and E is volume emissive power for dV at thermal temperature, T(z),

$$E = \varepsilon'\, 2\beta\, T(z). \tag{20}$$

With $dV = z\, d\omega\, dz/\cos\theta'$, and with a first order approximation for T(z), the intensity, dI', below the interface in direction θ' is

$$dI' = \varepsilon'\, 2\beta \left\{T_g + \left(\frac{\partial T}{\partial z}\right)_o z\right\}\ e^{-2\beta\, z/\cos\theta'} dz/\cos\theta' \tag{21}$$

where T_g is soil surface temperature, and I' has been normalized by Planck's coefficient so that its dimension is Kelvin. Integration of Equation (21) yields the upwelling intensity below the interface

$$I' = \varepsilon' \left\{T_g + \frac{\cos\theta'}{2\beta}\left(\frac{\partial T}{\partial z}\right)_o\right\} \tag{22}$$

If reflected sky-brightness and atmospheric absorption and emission are ignored, the normalized intensity above the interface (the radiobrightness, T_b) is $e(\lambda, \theta)\ I'(\theta')/\varepsilon'$, where $e(\lambda, \theta)$ is the directional spectral emissivity and the source of the emission polarization. Because of Snell's Law effects, cos θ' below the interface is relatively near to unity for most satellite incidence angles, θ (typically < 50°). With only a slight loss of generality, we shall assume that θ=0 so that polarization can be ignored, and so that brightness temperature can be written

$$T_b = e(\lambda)\ \{T_g + z_e \left(\frac{\partial T}{\partial z}\right)_o\} \tag{23}$$

where $z_e = (2\beta)^{-1}$ has the dimension of length. z_e should be called the effective emitting depth. It is equivalent to one optical depth in optics, or to half the skin depth in electromagnetics.

The dielectric properties of typical freezing soils at microwave frequencies are given by Hoekstra and Delaney [16]. Figure 5, from their paper, shows the variability in the complex dielectric constant for several moisture percentages in Groodrich clay and in Fairbanks silt. Note that the dielectric properties are essentially constant through freezing for a moisture content of 5%. This insensitivity to temperature for small moisture contents occurs because the water is chemisorbed, or adsorbed, to the clay or sand interfaces within the soil [17] and are not free to rotate with the electromagnetic wave. A reasonable approximation to the complex dielectric properties of moist soil, ε^*, through freezing is

$$\dot{\varepsilon} = \dot{\varepsilon}_{soil} + \frac{(m-0.07)}{(1-m)}\ \rho\ \{f\ \dot{\varepsilon}_{water} + (1-f)\ \dot{\varepsilon}_{ice}\} \tag{24}$$

where $\dot{\varepsilon}_{soil}$ = dielectric constant of 7% moist soil

$$\dot{\varepsilon}_{water} = n^2 + \frac{K_s - K_\infty}{1+(j\omega\tau_1)^{1-\alpha}} + \frac{K_\infty - n^2}{1+j\omega\tau_2} \quad [18][19]$$

$$n^2 = 1.8$$

$$K_s = 295.68 - 1.2283\ T + 2.094\times10^{-3}\ T^2 - 1.41\times10^{-6}\ T^3$$

$K_\infty = 4.2$

$\alpha = 0.012$

$\tau_1 = 5.62 \times 10^{-15}\, e^{0.188/kT}$ sec

$\tau_2 = 4.2 \times 10^{-14}$ sec

T = temperature Kelvin

k = Boltzmann's constant = 8.61735×10^{-5} eV/K

ω = angular frequency, radians/sec

$$\varepsilon^*_{ice} = K_\infty + \frac{K_s - K_\infty}{1 + j\omega\tau}$$

$K_\infty = 3.2$

$K_s = 3.2 + 20715/(T-38)$ [20]

$\tau = 4.76 \times 10^{-16}\, e^{0.577/kT}$ [21].

The Model

Appropriate model parameters for prairie near Bismarck are listed in Table 2. Parametric variables in these models are date and moisture content. While it might be argued that all parameters should be examined parametrically, the extensive computation required is not warranted by any possibility of inverting radiobrightness data to obtain more than moisture content or state.

The initial temperature of the thermal model was estimated from the average, diurnal radiation balance,

$$e\,\sigma\,T_{og}^4 = \frac{1}{24}\int_{24\ hr} (F_{sun} + F_{sky})\,dt \qquad (25)$$

where T_{og} becomes the initial temperature. T_{og} isotherms were placed at each centimeter of depth, and then propagated subject to the boundary conditions. The propagation time interval was assignable, but typically 6 seconds, and each 24 hour iteration began at midnight. The solution

was declared to have converged when the maximum surface temperature difference for each minute between 24 hour iterations was less than 0.001 Kelvins. Convergence required between eight and twelve iterations depending upon the month, the soil moisture content, and the propagation interval.

Observations

Temperature versus depth profiles at midnight, 6:00 a.m., noon, and 6:00 p.m. for Bismarck, ND, are shown in Figure 7. The gross features of these profiles are relatively independent of moisture content and month. Among these four profiles, surface temperatures are coldest at 6:00 a.m. (predawn) and hottest at noon as expected, and thermal pulses at depth are most pronounced at 6:00 p.m. Thermal gradients at the surface are always positive at midnight, 6:00 a.m., and 6:00 p.m., and they are always negative at noon. Note that the effect of freezing and thawing during October through December is a general compression of the temperature profile. That is, the apparent thermal inertia would be greater during freezing and thawing.

Figure 8 shows diurnal surface temperatures for September through December. The September curves, because temperatures are above freezing, look like the curves for diurnally heated, moist soils [9][10][11]. While moisture tends to reduce the day-night temperature difference, the effect is small. The October curves are very different. The daytime peak is lower because of reduced insolation, but nighttime curves are "held up" by the latent heat of fusion of soil moisture. The effects are similarly pronounced in November and December except that daytime peaks appear suppressed. The cause is the same -- daytime radiant heat goes into melting soil ice rather than into raising soil temperature. Again, an observable effect would be a strong increase in the apparent thermal inertia of freezing and thawing soils.

Effective emitting depths, z_e, as functions of microwave frequency, moisture content, and time-of-day are shown in Figure 9. The variability with frequency is caused by the Debye

relaxation processes in water and ice [16][17]. The September curves show the effects of moisture: The emitting depth of moist soil decreases with frequency, decreases with moisture content, and increases with insolation (maximum soil surface temperature) for frequencies below the primary relaxation frequency of water. The curves for October are dramatically different because ice in soil is effectively transparent to microwaves. Note that, for these model parameters, October near Bismarck is cold enough to completely freeze 10% and 15% moist soils, but not sufficiently cold to completely freeze 20% moist soil. The relatively smooth transitions between frozen and thawed emitting depths result from the assigned 3 degree freezing range of soil in this model. A reduced freezing range would cause a more abrupt transition.

The curves for November and December are mutually similar. Their major features are that the widths of the daytime melt period diminish slightly with increased moisture content because more of the daytime insolation must go into melting ice before temperatures rise. The slight increases in emitting depths with water content for the frozen periods occur because ice is more transparent to microwaves than the rock it replaces. The significant features of these curves are that microwave thermal emission originates much deeper in frozen soils than in moist soils, and that, for the SMMR frequencies, frozen soil emitting depths are roughly 1 cm and less. Therefore, frozen soil thermal gradients that are significant over depths of 1 cm should influence the SMMR spectral gradient.

Radiobrightness curves at the 10.7, 18, and 37 GHz SMMR frequencies, as functions of moisture content and time-of-day, are shown in Figure 10. The September (moist soil) brightness decreases with moisture content, and increases with microwave frequency. The frozen soil brightness curves during October through December are generally high and are relatively independent of microwave frequency. Midnight-noon differences are always positive for moist soils, and generally negative for diurnally thawing soils. While none of these soil models remain completely frozen throughout the day, a choice of parameters that avoids midday thawing would exhibit a positive midnight-noon shift in the spectral gradient. Of the three frequencies, the 37

GHz radiobrightness is least affected by moisture content or by freezing and thawing. That is, the 37 GHz radiobrightness most closely follows thermal temperature. It is this property that justifies its use as one of two discriminants in a SMMR, frozen soil classifier [7].

Radiobrightness spectral gradients, as functions of moisture content and time-of-day, are shown in Figure 11. The moist soil model gradients are always strongly positive, and the frozen soil model gradients are weakly negative. This unambiguous correlation is the reason that spectral gradient was chosen as a second discriminant in the SMMR, frozen soil classifier. SMMR observations are not universally unambiguous -- summertime, hot day SMMR data often exhibit negative gradients. However, summertime exceptions are unlikely to confuse a frozen soil classification.

The midnight and noon surface thermal gradients in Figure 7 are typically +1.5 and -3.5 degree/cm, respectively. This -5 degree/cm midnight-noon shift in the thermal gradient contributes about +0.1 K/GHz to the model's +0.5 to +1.4 K/GHz shift in the spectral gradient for the frozen soils shown in Figure 11. The preponderance of the shift is caused by the basic moist soil/frozen soil differences in spectral gradient. Note that the midnight-noon shift for moist soils (September) is negative.

Discrepancies

Model results are highly consistent with the SMMR observations reported by Zuerndorfer et al. [7]. However, there are three discrepancies: The SMMR frozen soil spectral gradient tends to be around -0.3 K/GHz, while the model predicts something like -0.1 K/GHz; the SMMR midnight-noon differences in spectral gradient for thawed soils average +0.2 K/GHz, while the model predicts that thawed soil differences should be weakly negative; and the SMMR moist soil spectral gradient can be negative on hot, summertime days, while the model predicts positive gradients.

While these discrepancies are ancillary to our objective of examining the performance of the 37 GHz radiobrightness and the 10.7-18-37 GHz spectral gradient as discriminants in a frozen soil classifier, they do suggest that the model is incomplete in that it ignores volume scatter darkening by prairie grasses and crop stubble, and by inhomogeneities within the frozen soil. The scattering albedo, ω_0, is a measure of the strength of volume scatter darkening. The parameter was used by Chandrasekhar [22] to describe darkening in planetary atmospheres, and applied by England [23][24] to describe darkening in frozen soils, ice, snow, and dry, planetary regoliths. It has become a parameter in most theories of wave propagation and scattering, e.g., Ishimaru [25]. For single scattering [25],

$$\omega_0 = \frac{N\sigma}{N\sigma + 2\beta} \tag{26}$$

where N is the number of scatterers per unit volume, σ is the scattering cross section for a single scatterer, and 2β is the power loss coefficient defined in Equation (19). For spherical scatterers whose diameters are small fractions of a wavelength (Raleigh scatterers),

$$\sigma \alpha \lambda^{-4} \tag{28}$$

so that ω_0 increases with decreasing wavelength to yield a negative spectral gradient of radiobrightness -- a "law of darkening". This short wavelength darkening is the likely cause of the strongly negative spectral gradient observed in SMMR data for frozen terrain.

The hot-day, negative spectral gradient may occur when heat drives most water from the canopy and from the upper layers of soil. Dry soils have an increased effective emitting depth so that volume scatter darkening may again cause a negative spectral gradient.

The discrepancy between observed and modeled, midnight-noon shifts in moist soil, spectral gradients may be caused by moisture (dew) on the plant canopy at midnight. However, without experimental studies, such explanations are only speculation.

Conclusions

A modified Chernous'ko method for solving Stefan's problem yields an acceptably rapid convergence to a solution for the thermal structure of diurnally insolated, moist and frozen soil. The modification involves an alternative, piecewise constant enthalpy-temperature approximation. With that modification, solutions exhibit the expected symmetry for heating and cooling.

Among the 10.7, 18, and 37 GHz SMMR frequencies, both the SMMR observations and the model show that the 37 GHz radiobrightness best tracks the thermal temperature of the soil's surface, and show that the 10.7-18-37 GHz spectral gradient is always negative for frozen soils. Therefore, the "and" condition, that the 37 GHz radiobrightness be below some threshold and that the spectral gradient be negative, should be an effective classifier of frozen soil.

Acknowledgement

This study was supported by NASA Interdisciplinary Research Program Grant NAG5-852.

References

[1] Burke, W.J., T. Schmugge, and J.F. Paris, "Comparison of 2.8- and 21-cm microwave radiometer observations over soils with emission model calculations," J. Geophys. Res., 84, pp.287-294, 1979.

[2] Wang, J.R., T.J. Schmugge, W.I. Gould, W.S. Glazar, and J.E. Fuchs, "A multi-frequency radiometric measurement of soil moisture content over bare and vegetated fields," Geophys. Res. Let., 9, pp. 416-419, 1982.

[3] Schmugge, T.J., "Remote sensing of soil moisture: Recent advances," IEEE Trans. Geosci. Rem. Sensing, GE-24, pp.12-22, 1983.

[4] Camillo, P.J., and T.J. Schmugge, "Correlating rainfall with remotely sensed microwave radiation using physically based models," IEEE Trans. on Geosci. and Rem. Sens., GE-22, pp. 415-423, 1984.

[5] Schmugge, T.J., P.E. O'Neill, and J.R. Wang, "Passive microwave soil moisture research," IEEE Trans. on Geosci. and Rem. Sens., GE-24, pp. 12-22, 1986.

[6] Schmugge, T.J., "Remote sensing applications in hydrology, Rev. Geophys., 25, pp. 148-152, 1987.

[7] Zuerndorfer, B.W., A.W. England, M.C. Dobson, and F.T. Ulaby, "Mapping freeze/thaw boundaries with SMMR data," in press, J. Agricultural and Forest Meteorology, 1989.

[8] Carslaw, H.S., and J.C. Jaeger, Conduction of Heat in Solids, 2nd Ed., Oxford, 1959.

[9] Watson, K., "Geologic application of thermal infrared images," Proc. of IEEE, pp. 128-137, Jan., 1975.

[10] Watson, K., L.C. Rowan, and T.W. Offield, "Application of thermal modeling in the geologic interpretation of IR images," Remote Sensing, K. Watson and R. Regan ed., Geophysics Reprint Series, no. 3, Society of Exploration Geophysicists, 1983.

[11] Kahle, A.B., "A simple thermal model of the Earth's surface for geologic mapping by remote sensing," J. Geophys. Res., 82, pp. 1673-1680, 1977.

[12] Evans, G.W., "A note on the existence of a solution to a problem of Stefan," Quarterly of Applied Mathematics, 9, pp. 185-193, 1951.

[13] Landau, H.G., "Heat conduction in a melting solid," Quarterly of Applied Mathematics, 8, pp. 81-94, 1950.

[14] Douglas, J., and T.M. Gallie, Jr., "On the numerical integration of a parabolic differential equation subject to a moving boundary condition," Duke Mathematical J., 22, pp.557-571, 1955.

[15] Chernous'ko, F.L., "Solution of non-linear heat conduction problems in media with phase changes," International Chemical Engineering J., 10, pp.42-48, 1970.

[16] Hoekstra, P., and A. Delaney, "Dielectric properties of soils at UHF and microwave frequencies," J. Geophys. Res., 79, pp. 1699-1708, 1974.

[17] Hoekstra, P., and W.T. Doyle, "Dielectric relaxation of surface adsorbed water," J. Colloid and Interface Sci., 36, pp. 513-521, 1971.

[18] Hasted, J.B., "Dielectric properties of water and aqueous solutions," Dielectric and Related Molecular Processes, The Chemical Society, London, pp. 121-162, 1972.

[19] Hasted, J.B., Aqueous dielectrics, Chapman and Hall, London, 302p., 1973.

[20] Cole, R.H., and O. Worz, "Dielectric properties of ice," Physics of Ice, N. Riehl, B. Bullemer, and H. Englehardt ed., Plenum, NY, pp. 456-554, 1969.

[21] Camp, P.R., W. Kiszenick, and D. Arnold, "Electrical conduction in ice," Physics of Ice, N. Riehl, B. Bullemer, and H. Englehardt ed., Plenum, NY, pp. 450-470, 1969.

[22] Chandrasekhar, S., Radiative Transfer, Dover, NY, p. 6, 1960.

[23] England, A.W., "Thermal microwave emission from a scattering halfspace," Radio Science, 9, pp. 447-454, 1974.

[24] England, A.W., "Thermal microwave emission from a scattering layer," J. Geophys. Res., 80, pp. 4484-4496, 1975.

[25] Ishimaru, A., Wave Propagation and Scattering in Random Media, I, Academic, NY, p. 11, 1978.

Table 1. Boundary Parameters	
F_{sun}	Solar irradiance = f_1 So (1-A) M(ϕ) cos ϕ
F_{sky}	Sky irradiance = $\sigma T_{sky}^4 + f_2$
F_{wind}	Sensible heat transfer from air to ground $\rho_a c_a C_d$ (W + 2) (T_{air} - T_{ground})
F_{ground}	e σT_g^4
So	Solar Constant = 0.03313 cal/sec^2
A	Albedo
M(ϕ)	Approximate atmospheric transmissivity 1.0 - 0.2 (cos ϕ)$^{-0.5}$ [9][10]
ϕ	Zenith angle
cos ϕ	cos λ cos δ (-cos(2π hour/24)+sin λ sin δ) if > 0, otherwise cos ϕ = 0
λ	local latitude
δ	declination = - 23.433^o cos(2π month/12)
f_1	≈(1-cl) where cl is average cloud cover. Approximation is that some is regained through f_2.
f_2	Irradiance from clouds, approximated as half the average solar irradiance lost in the cloud term, f_1. (cl/2) So (1-A) {$\int$ M(ϕ) cos ϕ dt}/24
σ	Stefan-Boltzmann constant = 1.3533x10^{-12}
T_{air}	Average air temperature To_{air} - T_{del} cos(2π(hour-2)/24) [11]
To_{air}	Monthly average air temperature (e.g., see Fig. 6) T_o - T_1 cos(2π(month-θ_{lag})/12)
T_{del}	Diurnal variation (from meteorological reports)
T_{sky}	T_{air}(0.61 +0.05 w$^{0.5}$)$^{0.25}$ (Brunt's formula, from Kahle [11])
w	Water vapor pressure, mmHg
ρ_a	Air density at surface = 1.25x10^{-3} gm/cm^3
c_a	Specific heat of dry air = .24 cal/gm-K
C_d	Drag coefficient = 0.002+0.006(Z/5000), Z is elevation in meters [11]
W	Wind velocity in m/sec
e	Thermal infrared emissivity
T_g	Soil surface temp from solution to heat flow equation

Table 2. Parameters for Bismarck, ND	
Latitude	47° N
Months	September through December (i.e., 9 - 12)
Soil moisture	10%, 15%, 20% by weight
Cloud cover, cl	20%
Average winds, w	5 m/sec
Albedo	0.2
Thermal IR emissivity, e	0.95
Freeze interval	270-273 K
Dry soil density	1.5 gm/cm^3
Dry soil specific heat	0.2 cal/gm
Dry soil thermal conductivity	0.0005 cal/cm-sec-deg
7% moist soil dielectric constant	3.3
7% moist soil loss tangent	0.23
Average air temperature, T_o	278.3 K (Fig. 6)
Annual air temp variation, T_1	16.9 K deg
Temp phase lag, θ_{lag}	1.12 months
Diurnal temp variation, T_{del}	5 K deg
Water vapor pressure, w	0.76 mmHg

Captions:

Fig. 1. Frequency gradient versus SMMR 37 GHz brightness temperature, Bismarck, North Dakota. Data were collected from 8/1/84 through 12/31/84. Shown with the Bismarck data are clustering decision thresholds for a frozen, mixed, or thawed surface. Based upon ground truth, the solid boxes are frozen, open boxes are thawed, and x's are mixed pixels (personal communication from Zuerndorfer, modified from Zuerndorfer et al. [7]).

Fig. 2. Enthalpy versus Temperature. E(T) and H(T) are approximations to moist soil enthalpy during freezing. H(T) in 2a represents Chernous'ko's, piecewise constant model. The asymmetry of H(T) at each isotherm produces dissimilar heating and cooling performance. H(T) in 2b is the modified model. The symmetry in H(T) at each isotherm produces the necessary similarity for heating and cooling.

Fig. 3. Integration path at constant time. The piecewise constant approximation to H(T) means that the enthalpies, H^- and H^+, are constant between isotherms.

Fig 4. Schematic of emission from a moist soil. Because of the transmissivity of soil, thermal microwave emission originates below its optical surface. If ϕ is the beam angle out of the page, $\phi = \phi' = 0$. $d\omega$ is the solid angle of the beam, $d\omega = d\theta\, d\phi$.

Fig. 5. The complex dielectric constant at 10 GHz as a function of temperature at three water contents for (a) Goodrich clay and (b) Fairbanks silt (from Hoekstra and Delaney [16]).

Fig. 6. Monthly average air temperatures for Bismarck, ND (from National Weather Service data). "Model" refers to the first order Fourier component.

Fig. 7. Temperature versus depth profiles for Bismarck, ND. Curves represent midnight, 6:00 a.m., noon, and 6:00 p.m. for three moisture contents.

Fig. 8. Diurnal soil surface temperatures at Bismarck, ND. Curves represent moisture contents by weight.

Fig. 9. Effective emitting depth versus time of day. Effective emitting depth is equivalent to optical depth in optics, or to 1/2 the skin depth in electromagnetics. Curves represent effective emitting depths for 3 microwave frequencies -- 10.7, 18, and 37 GHz.

Fig. 10. Radiobrightness versus time of day. Curves represent the brightness for 3 moisture contents and at 3 microwave frequencies.

Fig. 11. Radiobrightness spectral gradient versus time of day. Curves represent 3 moisture contents. The gradients are computed as a least squares regression of the radiobrightness at 10.7, 18, and 37 GHz.

Decision Space

1a Bismarck (Day)

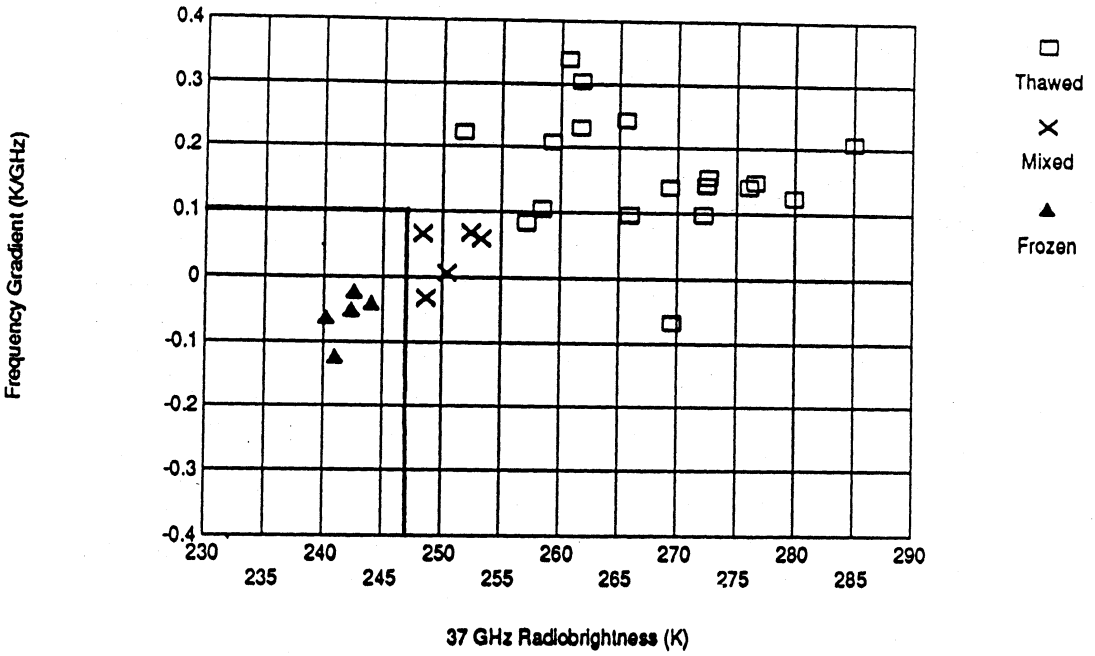

1b Bismarck (Night)

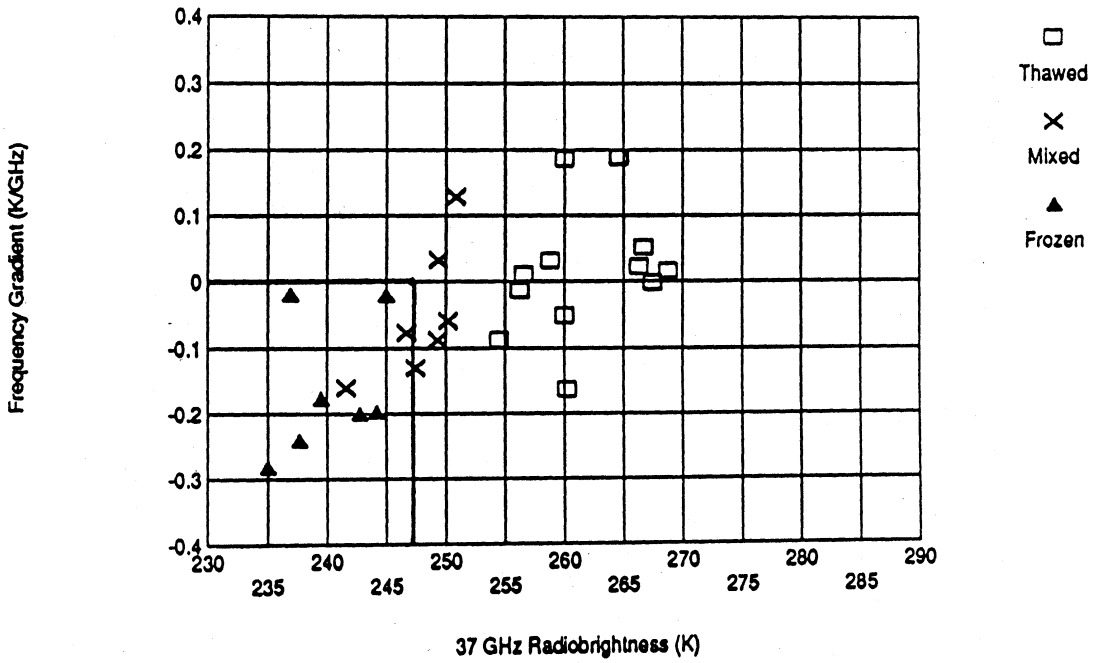

Figure 2a

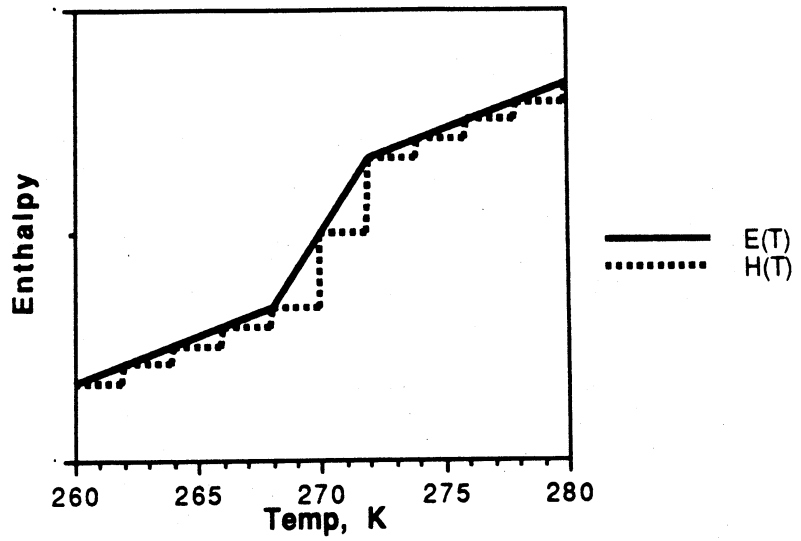

Figure 2b

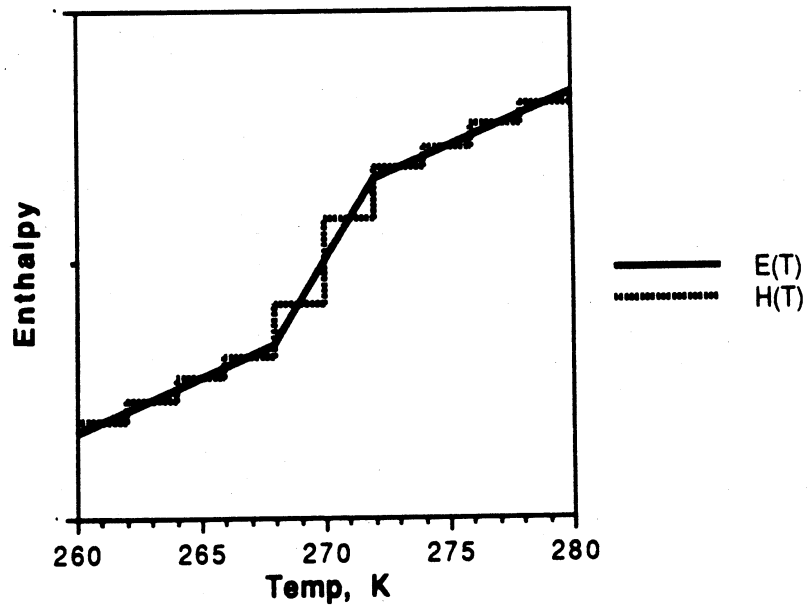

Figure 3

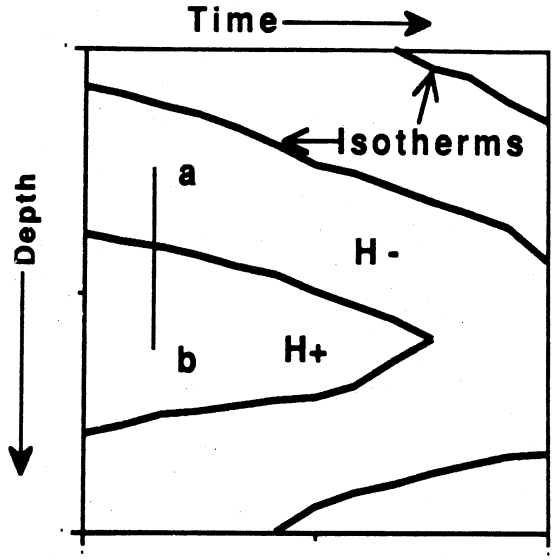

Figure 4

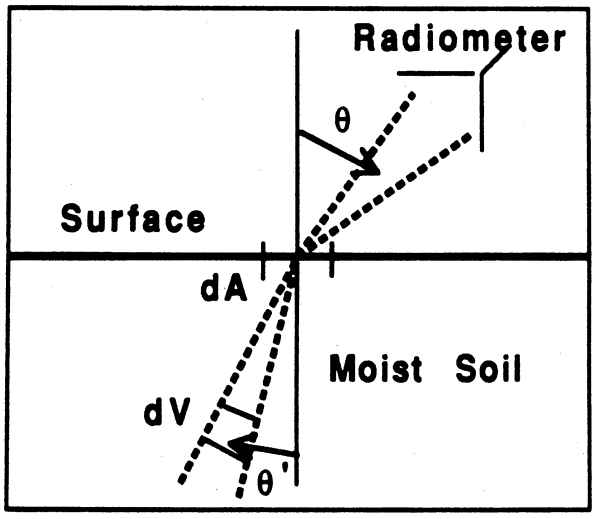

Figure 5a

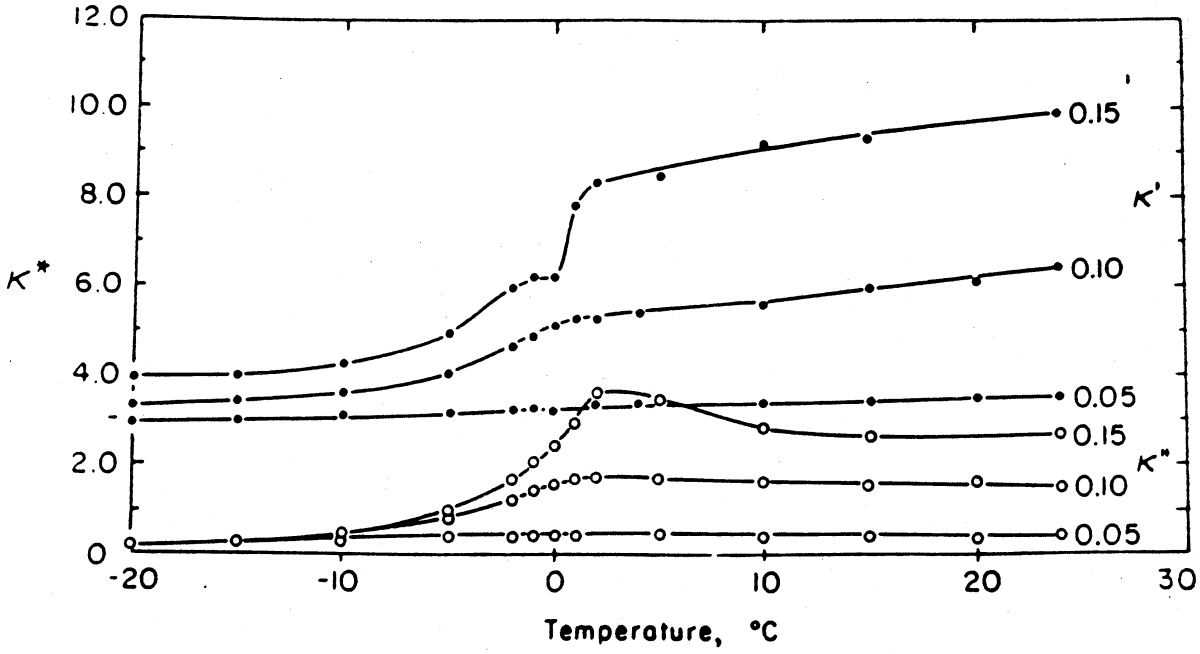

Figure 5b

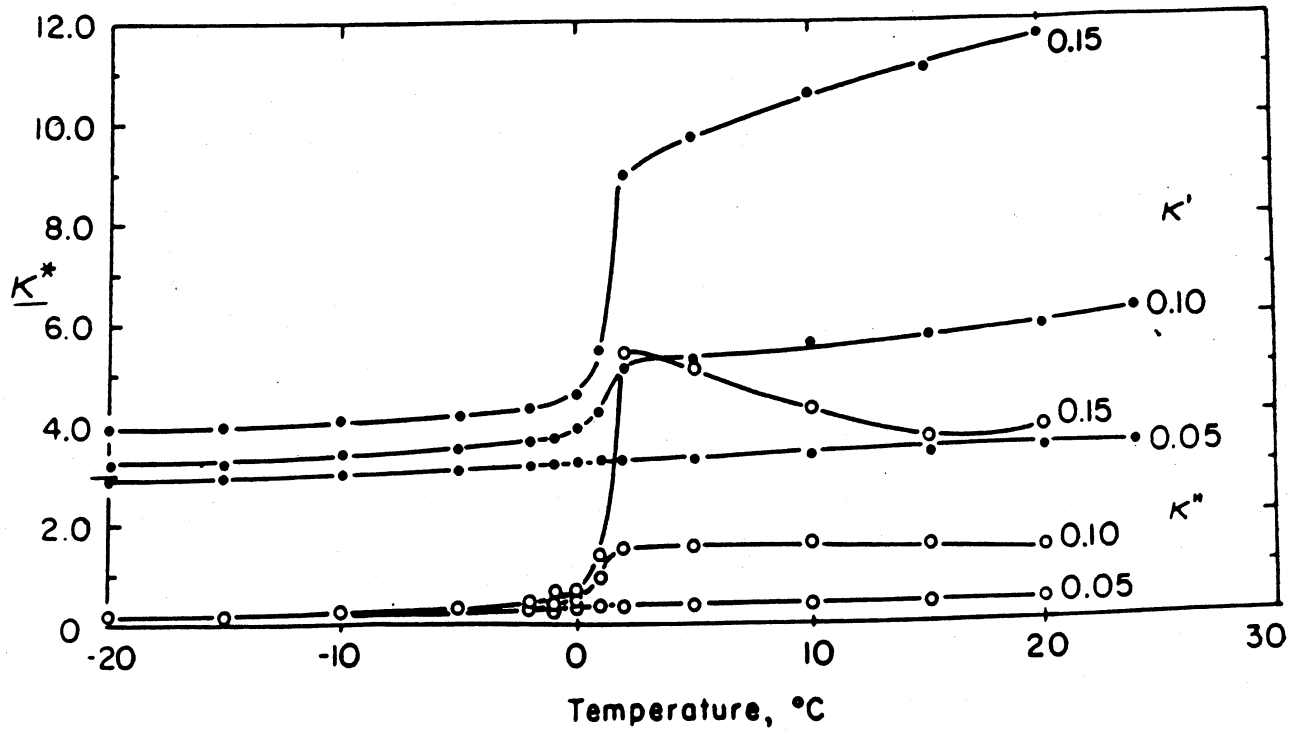

Figure 6

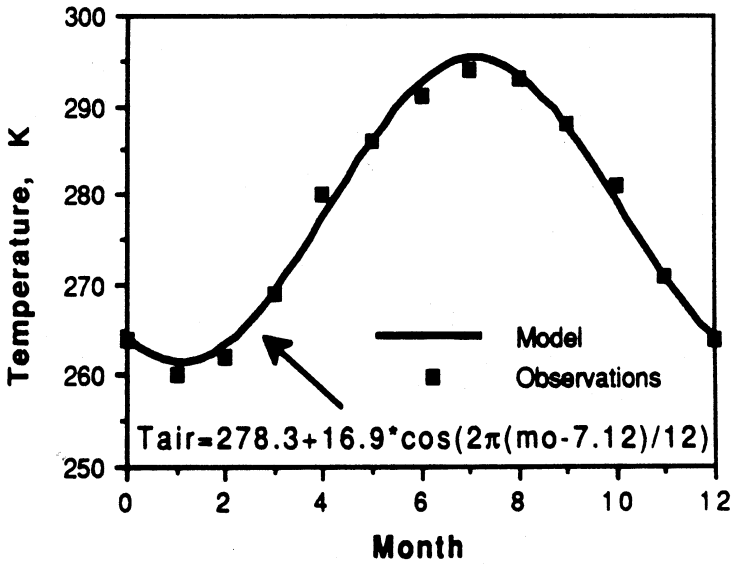
300
290
280
270
260
250
Temperature, K
0
2
4
6
8
10
12
Month
Model
Observations
Tair=278.3+16.9*cos(2π(mo-7.12)/12)

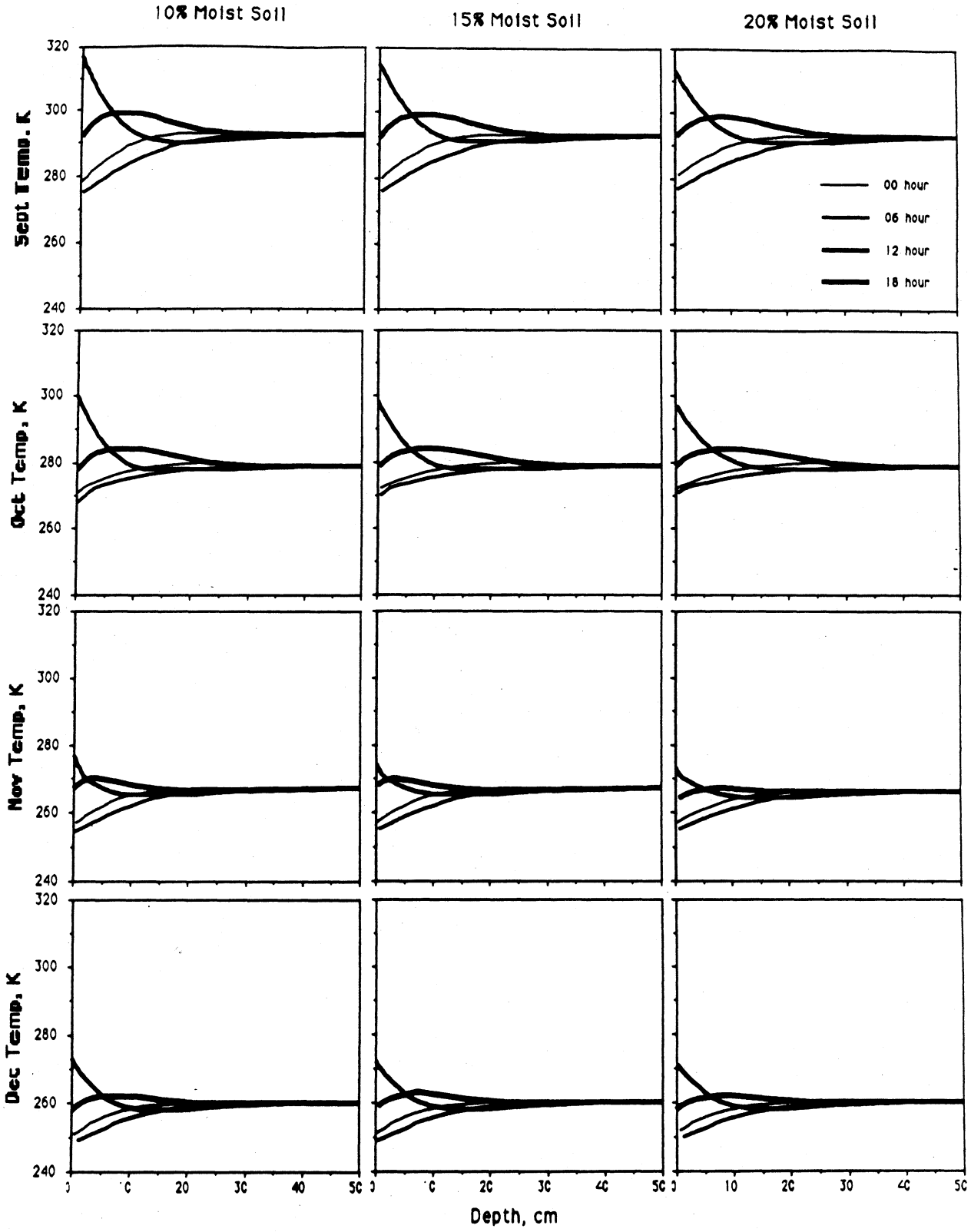
10% Moist Soil
15% Moist Soil
20% Moist Soil
Sept Temp, K
Oct Temp, K
Nov Temp, K
Dec Temp, K
320
300
280
260
240
00 hour
06 hour
12 hour
18 hour
0
10
20
30
40
50
Depth, cm

Fig. 7

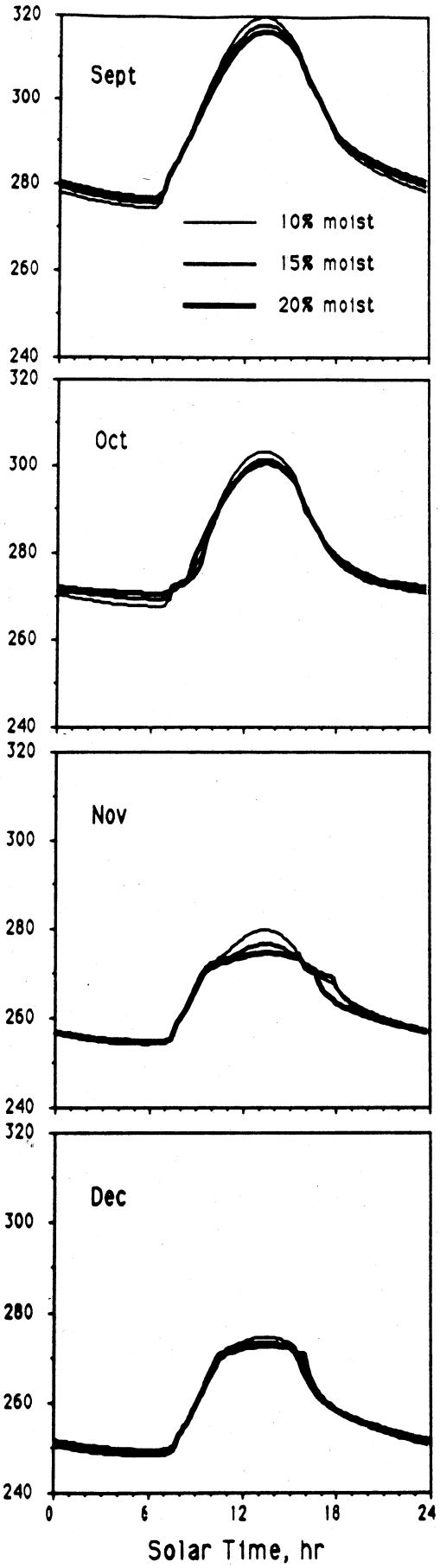
Sept
Oct
Nov
Dec
10% moist
15% moist
20% moist
320
300
280
260
240
0
6
12
18
24
Solar Time, hr

Fig. 8

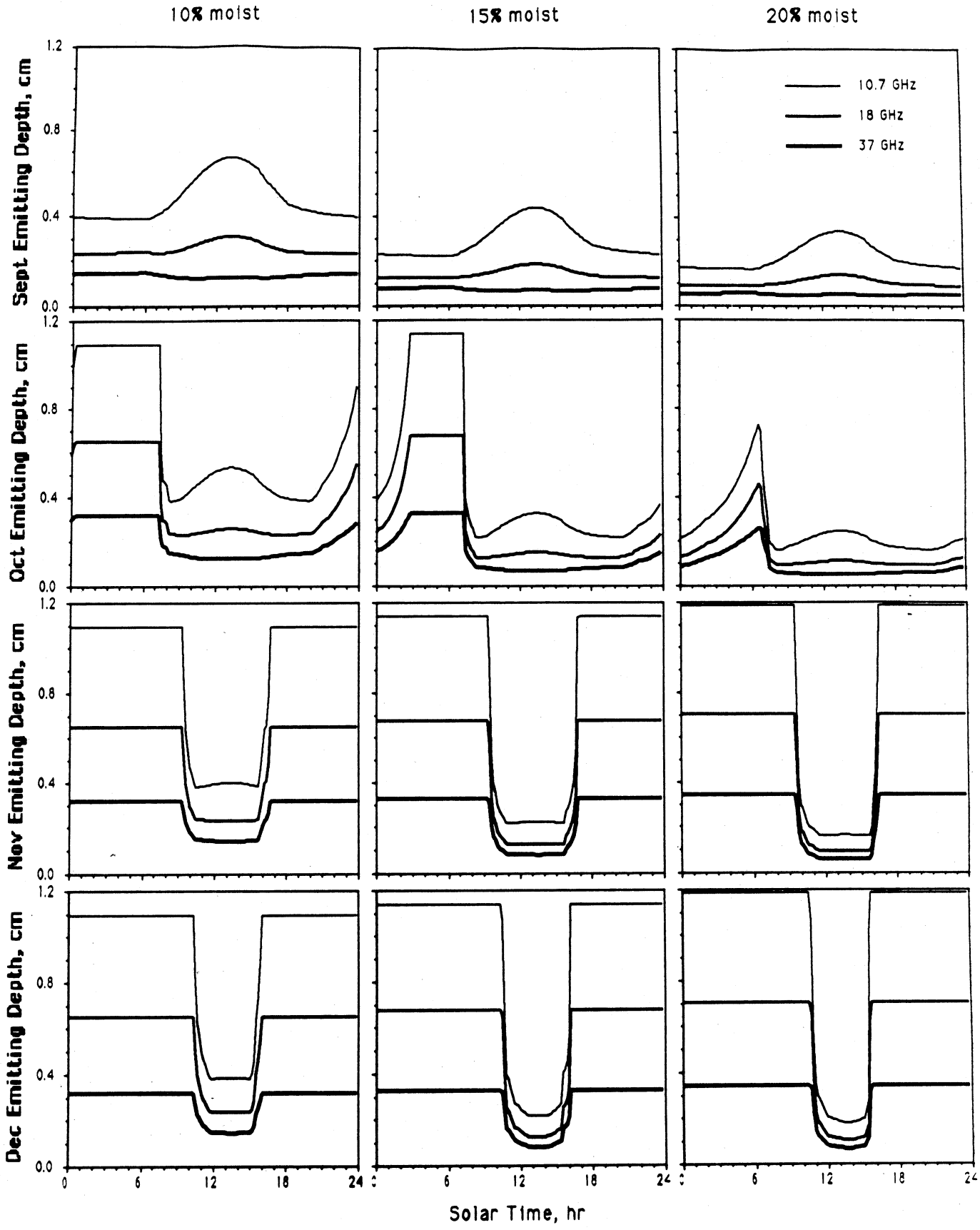
10% moist
15% moist
20% moist
10.7 GHz
18 GHz
37 GHz
Sept Emitting Depth, cm
Oct Emitting Depth, cm
Nov Emitting Depth, cm
Dec Emitting Depth, cm
0.0
0.4
0.8
1.2
0
6
12
18
24
Solar Time, hr

Fig. 9

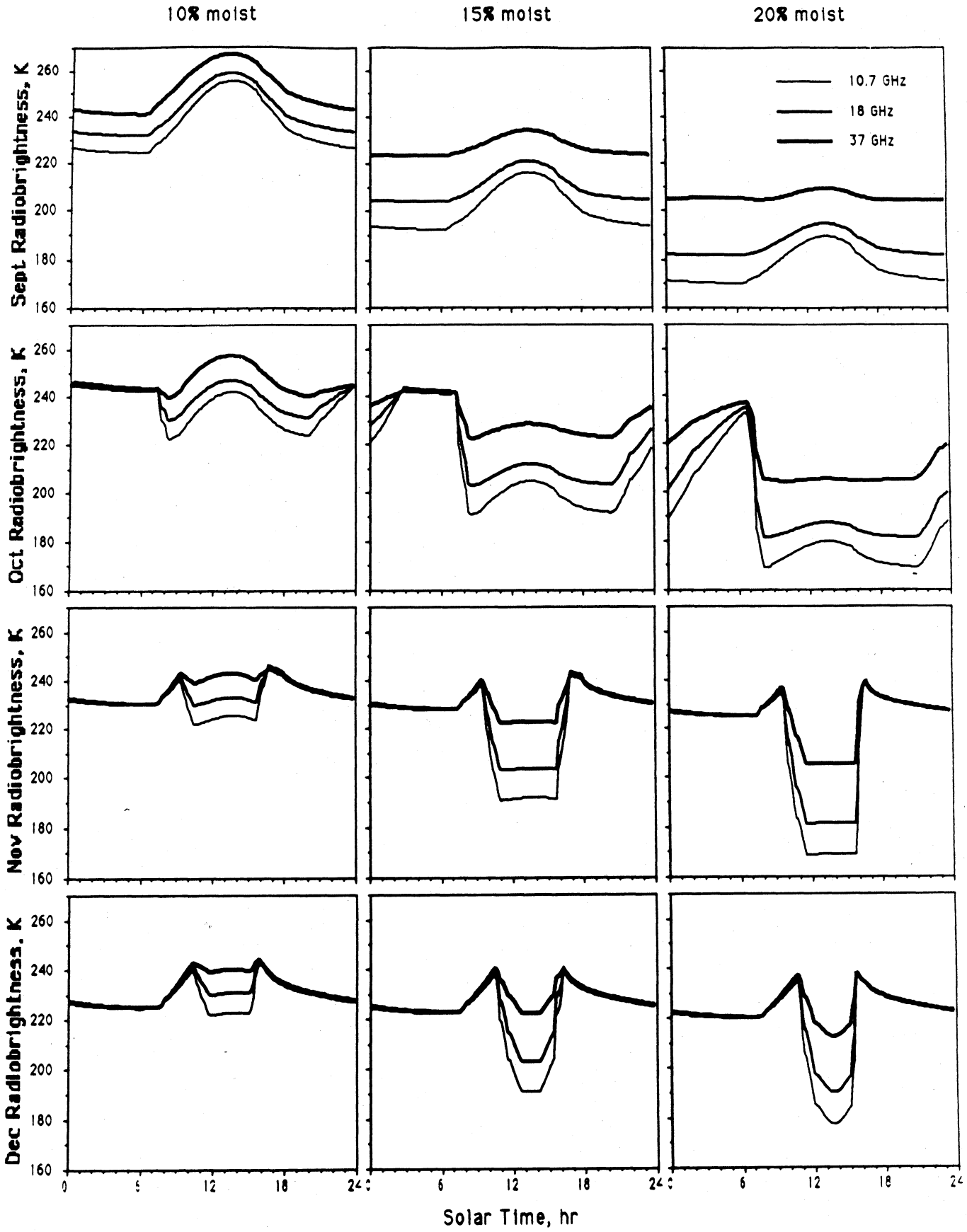
10% moist
15% moist
20% moist
10.7 GHz
18 GHz
37 GHz
Sept Radiobrightness, K
Oct Radiobrightness, K
Nov Radiobrightness, K
Dec Radiobrightness, K
260
240
220
200
180
160
0
6
12
18
24
Solar Time, hr

Fig. 10

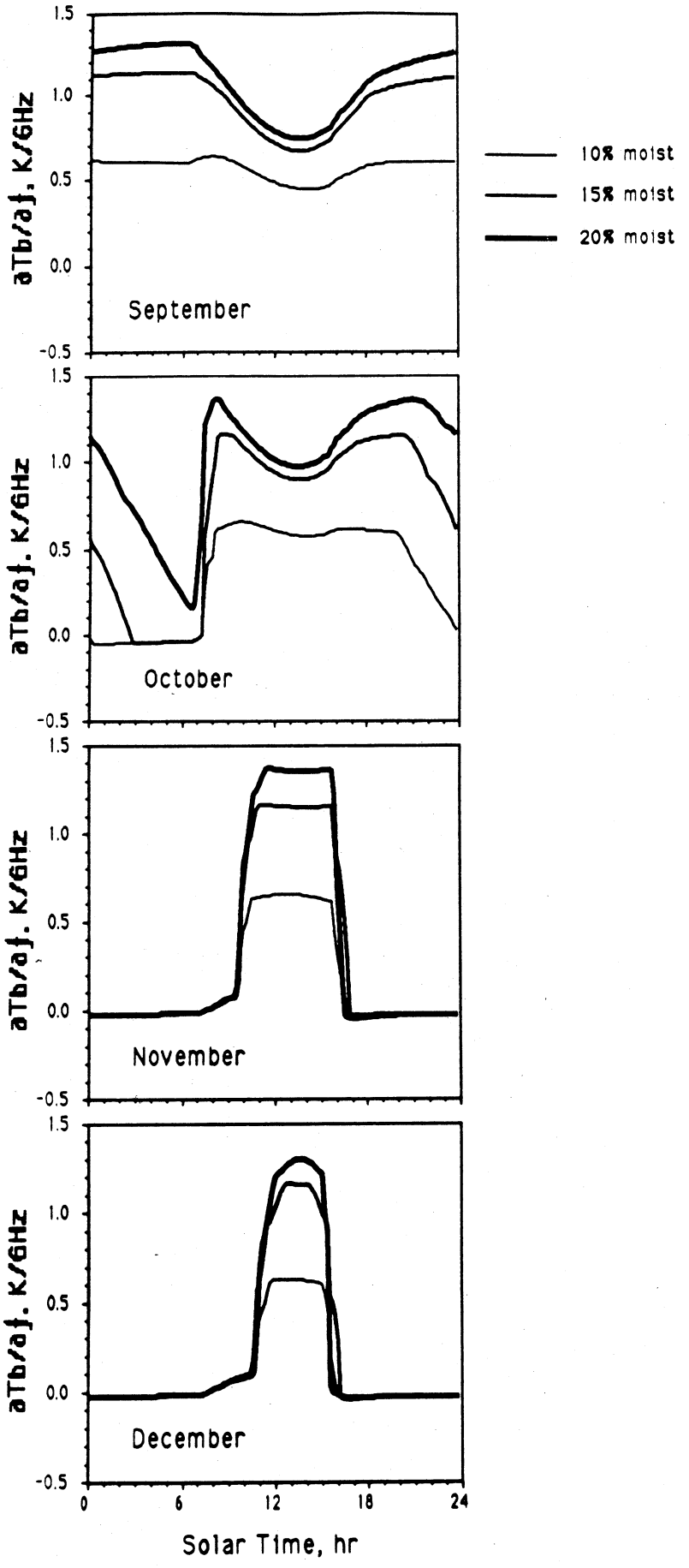
10% moist
15% moist
20% moist
September
October
November
December
aTb/aJ, K/6Hz
Solar Time, hr
1.5
1.0
0.5
0.0
-0.5
0
6
12
18
24

Fig. 11

MAPPING FREEZE/THAW BOUNDARIES WITH SMMR DATA

B. W. Zuerndorfer, A. W. England,
M. C. Dobson, and F. T. Ulaby

Radiation Laboratory
Department of Electrical Engineering
and Computer Science
The University of Michigan
Ann Arbor, MI 48109-2122

ABSTRACT

Nimbus 7 SMMR data are used to map daily freeze/thaw patterns in the upper Midwest for the Fall of 1984. The combination of a low 37 GHz radiobrightness and a negative 10.7, 18, and 37 GHz spectral gradient, $\frac{\partial T_b}{\partial f}$, appears to be an effective discriminant for classifying soil as frozen or thawed. The 37 GHz emissivity is less sensitive to soil moisture than are the lower frequency emissivities so that the 37 GHz radiobrightness appears to track soil surface temperature relatively well. The negative gradient for frozen ground is a consequence of volume scatter darkening at shorter microwave wavelengths. This shorter wavelength darkening is not seen in thawed moist soils.

INTRODUCTION

Soil moisture contributes to the energy exchange between the air and ground through latent heats of fusion and vaporization. Whether as boundary conditions for mesoscale climate modelling, or as inputs to an agricultural productivity model, the amount and state of soil moisture are regional parameters that one would like to estimate through satellite remote sensing. There is a large body of literature that addresses the estimation of soil moisture from remotely sensed radiobrightness (e.g. Burke et al., 1979; Wang et al., 1982; Blanchard and Chang, 1983; Schmugge, 1983; Jackson et al., 1984; Camillo and Schmugge, 1984; Schmugge et al., 1986; and Grody, 1988). We present evidence that moisture state can also be inferred from radiobrightness.

Freezing influences the measured radiobrightness temperature of the ground, T_b, through parameters in the approximation (Ulaby et al., 1981),

$$T_b = e\,T_o + (1-e)\,T_{sky},$$

where e and T_o are the emissivity and surface temperature of the ground, respectively, and T_{sky} is the effective sky brightness. In this approximation, atmospheric transmissivity is ignored. Frozen ground exhibits signatures of (1) lower thermal temperatures, T_o, (2) higher emissivity, e, and, as we will demonstrate, (3) a decrease in brightness temperatures with microwave frequency,

$$\frac{\partial T_b}{\partial f} < 0.$$

Signatures (1) and (2) are frequently ambiguous indicators of frozen ground because the changes in radiobrightness that result from freezing may be either positive or negative, depending upon the soil moisture content. Water molecules in frozen plants and soils are not free to align themselves with microwave electric fields. This constraint upon the rotational freedom of water gives rise to an apparent dryness to microwaves. The consequence is a decrease in the real part of the dielectric constant, ε', and an increase in frozen soil emissivity. For example, the real part of dielectric constants, ε', and corresponding emissivities at nadir, $\varepsilon(0)$, of two, homogeneous, smooth surfaced, 15% moist soils at 10 GHz are (ε' from Hoekstra and Delaney, 1974):

	+ 5° C			- 5° C		
Material	ε'	ε(0)	T_b	ε'	e(0)	T_b
Goodrich Clay	8.2	0.77	221	4.9	0.86	235
Fairbanks Silt	9.6	0.74	214	4.1	0.89	242

Because of increasing emissivity with frequency, a 10° decrease in the clay and silt soil temperatures, from +5° C to -5° C, would cause an increase in T_b of approximately +14 K and +28 K, respectively. The positive direction of change in T_b with soil freezing will cause confusion in discrimination between moist soils which will appear radiometrically warmer when frozen, and dry soils which undergo little molecular change and will appear radiometrically colder.

The shift in emissivity with freezing is most pronounced at the lower microwave frequencies. At 37 GHz, the effect is reduced but not absent. We observe that the 37 GHz radiobrightness correlates relatively well with air temperature (Figure 1). Since soil surface temperature should follow the air temperature, the 37 GHz radiobrightness can be expected to provide a reasonably reliable estimate of soil surface temperature. However, discrimination based only on the 37 GHz radiobrightness would misclassify too often.

Our data suggest a third signature of frozen soil. Freezing reduces the imaginary part of the dielectric constant, ε", proportionally more than it does the real part, ε'. The loss tangent, $\tan\delta=\varepsilon''/\varepsilon'$, is a measure of the attenuation per microwave wavelength. Reduced loss tangent, or lower attenuation, means that thermally emitted photons originate deeper within emitting media. That is, the effective depth of emission, z_e, ($1-e^{-1}$ of the emission originates above z_e) becomes a larger fraction of the free-space wavelength, λ_o (England, 1974, 1975, 1976, and 1977). For example, Goodrich Clay and Fairbanks Silt exhibit an increase of z_e with freezing (dielectric data from Hoekstra and Delaney ,1974) ,

	+ 5° C				- 5° C			
Material	ε'	ε"	tan δ	z_e	ε'	ε"	tan δ	z_e
Goodrich Clay	8.2	3.5	0.43	$0.13\ \lambda_o$	4.9	1.0	0.20	$0.36\ \lambda_o$
Fairbanks Silt	9.6	5.0	0.52	$0.10\ \lambda_o$	4.1	0.02	0.005	$15.7\ \lambda_o$

The effective emission depth of moist soils is typically 10% of the free-space wavelength. Frozen soils have effective emission depths that may be 30% or more of free-space wavelength. The effective emission depth of frozen sandy soils, like the Fairbanks Silt, can be several wavelengths. In the more transparent emitting media, particularly in frozen sandy soil or dry snow, the greater average thermal photon path lengths have two effects: a greater likelihood that thermal gradients affect spectral gradients, and a greater opportunity for volume scattering of photons.

Thermally induced spectral gradients occur because longer wavelength photons tend to originate below the optical surface where thermal temperatures may differ by several degrees from surface temperatures. For the lower loss tangents of frozen soil, this difference in average emitting depth is enough to reflect near surface thermal gradients caused by diurnal heating. That is, a

positive thermal gradient, $\partial T_o/\partial z$, where z is depth in the soil, will yield a negative spectral gradient, $\partial T_b/\partial f$, where f is microwave frequency. SMMR data are collected at midnight and noon. In the absence of changing weather conditions, midnight thermal gradients will be positive and noon thermal gradients will be negative (Figure 2) so that midnight spectral gradients will be negative, and noon spectral gradients will be positive. An average +0.2 Kelvin/f(GHz) shift in the spectral gradient is observed between midnight and noon for SMMR radiometric brightnesses (Figure 3). We are developing a computer model of these gradient effects. For now, thermally induced spectral gradients are noise to be filtered out.

The second consequence of soil freezing is a greater opportunity for volume scattering -- particularly at shorter microwave wavelengths. This occurs because of the greater average photon path lengths in frozen soil, and because plants and soil appear increasingly heterogeneous at shorter wavelengths. This "law of darkening" means that, for an isothermal, volume scattering halfspace,

$$\frac{\partial T_b}{\partial f} < 0$$

(England, 1974).

Frozen terrain may also be snow covered. Dry snow is exceedingly transparent to microwaves so that snow exhibits significant of darkening (Figure 4, Edgerton et al., 1971). That is, both frozen soil and snow tend to exhibit negative spectral gradients.

While neither a low 37 GHz radiobrightness nor a negative spectral gradient is solely adequate as a classifier of frozen soils, particularly at the relatively coarse resolutions of the Nimbus-7 SMMR, a discriminant based upon a combination of these signatures offers considerable promise. Our objective under NASA Interdisciplinary Research Program Grant NAG5-852 has been to determine whether such a discriminant is feasible.

RADIOBRIGHTNESS AND GROUND TEMPERATURES, AND THE CLASSIFICATION DISCRIMINANT

Nimbus 7 SMMR (Scanning Multichannel Microwave Radiometer) radiobrightness data at 6.6 GHz, 10.7 GHz, 18 GHz, and 37 GHz were obtained for August 1, 1984, through December 31, 1984, over an area that included North Dakota, about half of each neighboring state, and part of southern Canada (Figures 7-9). We chose this large, relatively uniform area because of the low spatial resolution of the SMMR instruments -- 150 Km at 6.6 GHz, 100 Km at 10.7 GHz, 60 Km at 18 GHz, and 30 Km at 37 GHz, and because of the importance of soil moisture state to this region's hydrologic processes. The data arrived from the National Space Science Data Center (NSSDC) on 21, high density, SMMR Cell Tapes. Such data are referenced to latitude and longitude in a satellite-centered coordinate system. We produced two types of image products: Single-band, radiobrightness images at the intrinsic resolution of each sensor, and (2) composite, multi-band images at a common resolution based upon local area averaging. Each radiobrightness pixel was referenced to latitude-longitude in a Mercator projection by interpolation and resampling the Cell Tape data. We used a bi-cubic approximation of a sinc function (Moik, 1980) for the interpolation. H and V radiobrightnesses were averaged to produce a single brightness for each pixel for each frequency.

In addition to large area images, local area spatial averages of radiobrightness were calculated for each radiobrightness channel at 7 meteorologic sites within our test region--Miles

City, MT; Bismark, Fargo, and Williston, ND; and Abileen, Huron, and Rapid City, SD. A local area is defined as a 150 Km cell centered on the meteorological site (150 Km is the spatial resolution of the 6.6 GHz channel). Air and ground temperature data for the Fall of 1984 were obtained from NOAA's National Climatic Data Center in Asheville, North Carolina. Air temperature measurements were available for noon and midnight at the meteorologic sites (i.e., simultaneously with the satellite pass), but ground temperature measurements were for 7:00 a.m. and 7:00 p.m. EST, and were not co-located with the meteorologic sites. Ground temperatures are measured at 5 cm depths. Diurnal heating will weakly affect 5 cm temperatures so that there will be some differences for the times of the satellite pass.

Local area averages at the meteorologic sites were used to define the preliminary boundaries in our Freeze Indicator discriminant. For example, Figure 1 illustrated the correlation between 37 GHz radiobrightness and reported air temperature. The nominal line in these figures is a single best fit linear regression in the least squares sense of all local area averages. Individual linear fits will differ slightly as shown in Figure 1(a). We used the nominal line in our discriminant for simplicity, but a more sophisticated discriminant might use the actual least squares fit for the local area and for the time of day. The discriminant boundaries in Figures 1(b) and 1(c) are merely estimates based upon the nominal regression and a compromise between midnight and noon air temperatures that would imply frozen soil (the lower boundary) and thawed soil (the upper boundary). Remember that diurnal temperature gradients will generally cause midnight, sub-surface soil temperatures to be warmer than air temperatures, and noon, sub-surface soil temperatures to be colder.

Similarly, local area averages of spectral gradient versus air temperature were the bases for the spectral gradient decision boundaries shown in Figure 3. Note that the midnight freeze boundary in this example is relatively unambiguous, while a more effective noon freeze boundary would be shifted upwards by 0.2 K/GHz. Again, for simplicity in this preliminary study, we used discriminant boundaries that were time and location independent.

Our 2-parameter Freeze Indicator incorporates the single-band, 37 GHz radiobrightness, and a spectral gradient based upon linear regression of 10.7, 18, and 37 GHz radiobrightnesses for each pixel. Based upon the decision boundaries in Figure 1(b) and 1(c), the likelihood of frozen ground in a 37 GHz pixel, p_{37}, is estimated as

$$p_{37} = \begin{cases} 0 & Tb(37) > Tb_{max} \\ \dfrac{Tb_{max} - Tb(37)}{Tb_{max} - Tb_{min}} & Tb_{min} < Tb(37) < Tb_{max} \\ 1 & Tb(37) < Tb_{min} \end{cases}$$

where T_b (37) is the measured 37 GHz radiobrightness, and the preliminary decision boundaries are

$Tb_{max} = 259$ K

$Tb_{min} = 247$ K

The likelihood of frozen ground based upon spectral gradient decision boundaries in Figure 3(a) and 3(b) is p_{sg}, and is estimated as

$$p_{sg} = \begin{cases} 0 & \frac{\partial Tb}{\partial f} > \left(\frac{\partial Tb}{\partial f}\right)_{max} \\ \dfrac{\left(\frac{\partial Tb}{\partial f}\right)_{max} - \frac{\partial Tb}{\partial f}}{\left(\frac{\partial Tb}{\partial f}\right)_{max} - \left(\frac{\partial Tb}{\partial f}\right)_{min}} & \left(\frac{\partial Tb}{\partial f}\right)_{min} < \frac{\partial Tb}{\partial f} < \left(\frac{\partial Tb}{\partial f}\right)_{max} \\ 1 & \frac{\partial Tb}{\partial f} < \left(\frac{\partial Tb}{\partial f}\right)_{min} \end{cases}$$

where the preliminary decision boundaries are

$$\left(\frac{\partial Tb}{\partial f}\right)_{max} = 0.3 \text{ K/GHz}$$

$$\left(\frac{\partial Tb}{\partial f}\right)_{min} = -0.3 \text{ K/GHz}$$

These boundaries are preliminary in that they were chosen to yield the fewest misclassifications in plots of the type shown in Figure 5(a) and 5(b). More refined discriminants would incorporate area and time specific decision boundaries. This would be relatively straightforward if there were a higher density of weather stations in the test area. As it is, we believe that diurnal temperature modeling well yield effective time dependent boundaries, and, perhaps, requiring sub-region consistency within a classification will yield improved spatially dependent boundaries. These refinements are to be part of our continuing project. However, it is the basic sparseness and lack of control of air and ground data that should prompt some caution about over-interpreting our results.

Our freeze/thaw discriminant, or Freeze Indicator, is the product of p_{37} and p_{sg}, and is applied at the scale of the 10.7 GHz data. Resolution differences between different frequency channels can produce anomalous composite image results if the data were processed directly at their original scale. To avoid these problems, the resolution of the data from each channel is compensated to the (coarse) resolution of the lowest frequency channel used in estimating spectral gradients (i.e. 10.7 GHz and 100 Km resolution). Under certain constraints upon the classification process, these images can be referenced to the higher resolution, 37 GHz format for better location of freeze/thaw boundaries (Zuerndorfer, et al., 1989). The effort needed to do this would be justified as a part of an improved classification process. Figures 7 through 12 include images of the Freeze Indicator for various times during the test period. Black in these images indicates a high likelihood of frozen ground.

OBSERVATIONS

Figure 6(a) and 6(b) show normalized brightness temperatures for midnight and noon, respectively, in the northern Great Plains during the Fall of 1984. Normalized brightnesses are the average regional brightness at each microwave frequency divided by the average regional air temperature. Normalized brightness thus has the dimension of emissivity. Note that there is little systematic ordering among the 10.7, 18, and 37 GHz normalized brightnesses during August through most of November. However, during the latter half of November through December, the normalized brightnesses at midnight are uniformly ordered, 10.7 GHz brightnesses are high, 18 GHz brightnesses are middle, and 37 GHz brightnesses are low. That is, they exhibit negative average spectral gradients. The noon normalized brightnesses for December exhibit a similar trend, but with exceptions. These are, we believe, illustrations of the law of darkening for frozen soils. Soils at midnight in December for the northern Great Plains are very likely to be frozen.

Performance of the freeze/thaw discriminant is demonstrated in Figures 7-9 where Freeze Indicator (FI) images are compared with ground and air temperature measurements for midnight on 9/20/84, 10/24/84, and 12/9/84. Midnight FI images are shown as better examples of the potential of a freeze discriminant. Noon FI images are generally less consistent with meteorologic reports because of the contribution of the noontime positive diurnal spectral gradient to the negative frozen ground spectral gradient that we discussed in the last section. Areas not covered by the satellite in a particular pass are shown in white. Tables 1-3 are summaries of the meteorologic reports.

On the night of September 20 (Fig. 7), air temperatures throughout the region were near 60^{o} F and had been above freezing for several days. The FI image shows weak, probably false indications of freezing in the prairies of ND, southern Canada, and the rolling glacial terrain east of the Red River Valley in Minnesota. While the dry air of the northern prairies permits nighttime radiation cooling of the ground to temperatures below that of the air, the more likely explanation for the weak freeze indication is short wavelength scattering by the tall prairie grasses in the northern great plains, and by woodland areas in Minnesota. However, there are no strong indications of freezing in the FI image.

On the night of October 24 (Fig. 8), air temperatures hovered about freezing throughout the area, but had been below freezing at Williston for several days, and generally above freezing toward the east (see the temperatures for Fargo, Aberdeen, and Huron in Table 2). The FI image shows a strong freeze indication in northwestern ND which is consistent with the temperature patterns. Similarly, the definite thaw indication along the Red River Valley is consistent with the warmer temperatures reported and the generally more moist soil in the Valley.

On the night of December 9 (Fig. 9), air temperatures were generally below freezing except at Rapid City, SD, and had been below freezing for several days. There was no more than trace snow on the ground anywhere in the region. The FI image shows strong freeze indications throughout most of the region with weaker indications near Rapid City, and in the Aberdeen-Fargo sub-region (Aberdeen is not shown on the December 9 map because its temperature report was missing for that date). Again, the FI image is consistent with the temperature record.

37 GHz radiobrightness and FI image sequences were produced at midnight and noon for six-day periods in September, October, and December (Figures 10-12). SMMR coverage is based on a 48 hour cycle--midnight (0000 local hours on the date shown), noon (1200 hours on the same date), and then midnight again 36 hours later. However, orbit precession causes gaps in the cycle and variations in the coverage footprint. Within these constraints, our objective was to observe, if possible, weather dynamics reflected in the FI images.

The 37 GHz sequence beginning on September 16 (Figure 10 and Table 1) shows the moist area associated with the Missouri River, Sakakawea and Devils Lakes in ND, and the Missouri River and Lake Oahe in SD. Rain during the night of September 21 appears as a regional darkening of the 37 GHz image for midnight on the 22nd. Note that the rain is not picked up in the FI image.

The October sequence (Figure 11) is dominated by a cold front passing through the area from the northwest with rain and snow beginning on October 19. The region is warmer and drier by the 26th. The moisture pattern dominates the 37 GHz image, but only the apparent freeze pattern, which generally lags the cold front, is shown in the FI image. Note that strong freeze indications follow the cold front but weaken in the south with warming on the 26th.

The December sequence (Figure 12) is characterized by cold temperatures and snow from December 2 through December 5, followed by daytime warming into the 40's (and even 58^{o} at Rapid City, SD) by the 9th. The FI images reflect this general coldness, but also show daytime thawing toward the end of the period.

CONCLUSIONS

Freeze Indicator images based upon a preliminary, 2-parameter discriminant--37 GHz radiobrightness and 10.7, 18, and 37 GHz spectral gradient--show relatively good correlation with the expected state of moisture in northern Great Plains soils during the Fall of 1984. The discriminant is preliminary in the sense that both theoretical and experimental work needs to be done to fully exploit the diurnal radiobrightness signatures of frozen soils. The concept underlying the preliminary discriminant is that frozen soil will exhibit volume scatter darkening at shorter microwave wavelengths much like the effect observed in dry snow. Few other phenomena cause negative microwave spectral gradients. However, one such phenomenon is diurnal insolation which should cause negative spectral gradients at midnight, but positive spectral gradients at noon. We are in the process of tayloring our discriminant to allow for these diurnal gradients.

Freeze Indicator images based upon SMMR data effectively map temporal variations in the freeze/thaw pattern for the northern Great Plains at the time scale of days. These patterns are synchronized with weather patterns, but are not identical. We intend to expand our test data set to include several complete seasons. The product would be, in essence, a movie of freeze/thaw patterns as weather fronts sweep through the Great Plains throughout several seasons. The development of these data from SMMR archives should provide one aspect of a meso-scale climatic baseline for the region.

REFERENCES

Blanchard, B.J., and A.T.C. Chang, 1983, Estimation of soil moisture from Seasat SAR data, Water Res. Bull. 19, p. 803-810.

Burke, W.J., T. Schmugge, and J.F. Paris, 1979, Comparison of 2.8- and 21-cm microwave radiometer observations over soils with emission model calculations, JGR 84, p. 287-294.

Camillo, P.J., and T.J. Schmugge, 1984, Correlating rainfall with remotely sensed microwave radiation using physically based models, IEEE Trans. on Geosc. and Rem. Sens. GE-22, p. 415-423.

Edgerton, A.T., A. Stogryn, and G. Poe, 1971, Microwave Radiometric Investigations of Snowpacks, Final Rept. 1285R-4 of Contract 14-08-001-11828 between Aerojet-General Corp., El Monte, CA, and the U.S. Geological Survey.

England, A.W., 1974, The effect upon microwave emissivity of volume scattering in snow, in ice, and in frozen soil, Proc. URSI Spec Mtg on Microwave Scattering and Emission from the Earth, Berne, Switzerland, 23-26 Sept., 1974.

England, A.W., 1975, Thermal microwave emission from a scattering layer, JGR 80, p. 4484-4496.

England, A.W., 1976, Relative influence upon microwave emissivity of fine-scale stratigraphy, internal scattering, and dielectric properties, Pageoph 114, p. 287-299.

England, A.W., 1977, Microwave brightness spectra of layered media, Geophysics 42, p. 514-521.

Grody, N.C., 1988, Surface identification using satellite microwave radiometers, IEEE Transactions on Geoscience and Remote Sensing, V. 26, p. 850-859.

Hoekstra, P., and A. Delaney, 1974, Dielectric properties of soils at UHF and microwave frequencies, JGR 79, pp.1699-1708.

Moik, J., 1980, Digital Processing of Remotely Sensed Images, NASA SP-431.

Schmugge, T.J., 1983, Remote sensing of soil moisture: Recent advances, IEEE Trans. on Geosc. and Rem. Sens. GE-21, p. 336-344.

Schmugge, T.J., 1987, Remote sensing applications in hydrology, Rev. Geophys. 25, p. 148-152.

Schmugge, T.J., P.E. O'Neill, and J.R. Wang, 1986, Passive microwave soil moisture research, IEEE Trans. on Geosc. and Rem. Sens. GE-24, p. 12-22.

Ulaby, F.T., R.K. Moore, and A.K. Fung, 1981, Microwave Remote Sensing, Active and Passive, Addison-Wesley, p. 186-255.

Wang, J.R., T.J. Schmugge, W.I. Gould, W.S. Glazar, and J.E. Fuchs, 1982, A multi-frequency radiometric measurement of soil moisture content over bare and vegetated fields, Geophys. Res. Let. 9, p. 416-419.

Watson, K., L.C. Rowan, and T.W. Offield, 1983, Application of thermal modeling in the geologic interpretation of IR images, Remote Sensing, SEG Reprint Series, no. 3, p. 345-369.

Zuerndorfer, B., A.W. England, and G.H. Wakefield, 1989, The radiobrightness of freezing terrain, Proc. of IGARSS '89, Vancouver, B.C., July 10-14, in press.

TABLE 1

Year 1984	Site	Air Temp (°F) 00	Air Temp (°F) 12	Cloud Cover (x/10) 00	Cloud Cover (x/10) 12	Precip. (in.) 00	Precip. (in.) 12	Precip. (in.) 24h	Precip. (in.) Rem	Snow Pack (in.) 24h
9/15	Aberdeen	40	63	2	3	0	0	0		0
	Bismark	39	64	0	0	0	0	0		0
	Fargo	46	63	8	0	0	0	T		0
	Huron	44	64	0	3	0	0	0		0
	Miles City	50	65	2	2	0	0	0		0
	Rapid City	44	63	4	2	0	0	0		0
	Williston	48	60	6	0	0	0	0		0
9/16	Aberdeen	46	65	1	3	0	0	0		0
	Bismark	53	67	0	2	0	0	0		0
	Fargo	47	69	0	0	0	0	0		0
	Huron	50	64	5	10	0	0	0		0
	Miles City	58	74	0	3	-	-	0		0
	Rapid City	52	70	3	6	0	0	0		0
	Williston	55	68	0	3	0	0	0		0
9/17	Aberdeen	57	71	2	8	0	0	0		0
	Bismark	56	83	0	1	0	0	0		0
	Fargo	57	73	0	3	0	0	0		0
	Huron	58	73	10	3	0	0	0		0
	Miles City	61	80	0	0	-	-	0		0
	Rapid City	64	84	0	0	0	0	0		0
	Williston	56	74	0	3	0	0	0		0
9/18	Aberdeen	64	81	0	0	0	0	0		0
	Bismark	57	80	0	0	0	0	0		0
	Fargo	64	81	0	0	0	0	0		0
	Huron	62	84	0	0	0	0	0		0
	Miles City	60	80	0	0	-	-	0		0
	Rapid City	63	90	0	0	0	0	0		0
	Williston	67	73	0	0	0	0	0		0
9/19	Aberdeen	59	84	0	1	0	0	0		0
	Bismark	55	86	0	0	0	0	0		0
	Fargo	65	90	0	0	0	0	0		0
	Huron	68	90	0	0	0	0	0		0
	Miles City	67	76	0	0	-	-	0		0
	Rapid City	60	90	0	0	0	0	0		0
	Williston	57	72	0	0	0	0	0		0
9/20	Aberdeen	62	65	0	9	0	0	0		0
	Bismark	58	63	0	9	0	0	0		0
	Fargo	54	62	0	6	0	0	0		0
	Huron	62	71	0	2	0	0	0		0
	Miles City	63	72	7	2	-	-	T		0
	Rapid City	59	67	2	6	0	0	0		0
	Williston	54	51	8	9	0	.01	0.15	(R)	0
9/21	Aberdeen	59	82	2	2	0	0	0.1		0
	Bismark	58	81	8	7	0	0	0.3	(R)	0
	Fargo	59	77	10	9	0	0	0		0
	Huron	60	83	0	0	0	0	0		0
	Miles City	66	56	10	10	-	-	0.18	(R)	0
	Rapid City	60	83	2	1	0	0	0.07	(R)	0
	Williston	57	54	10	10	.02	.01	0.3	(R)	0
9/22	Aberdeen	61	65	8	2	T	0	T		0
	Bismark	52	60	3	1	0	0	0		0
	Fargo	72	66	9	0	T	0	0.02		0
	Huron	66	66	10	2	.05	0	.011	(R)	0
	Miles City	46	52	4	6	-	-	0		0
	Rapid City	45	60	3	4	0	0	0		0
	Williston	45	44	10	9	0	0	0		0

TABLE 2

Year 1984	Site	Air Temp (°F) 00	Air Temp (°F) 12	Cloud Cover (x/10) 00	Cloud Cover (x/10) 12	Precip. (in.) 00	Precip. (in.) 12	Precip. (in.) 24h	Precip. (in.) Rem	Snow Pack (in.) 24h
10/19	Aberdeen	37	44	10	8	.01	0	.1	(R)	0
	Bismark	36	40	10	10	0	0	.04	(S)	0
	Fargo	40	38	10	10	.07	0.2	.77	(R)	0
	Huron	38	45	10	7	0.1	0	.01		0
	Miles City	28	39	7	4	-	-	T		0
	Rapid City	26	42	2	7	0	T	T		T
	Williston	27	34	2	10	-	-	.1	(S)	0
10/20	Aberdeen	36	44	-	10	0	0	T		0
	Bismark	35	38	9	10	T	.01	.1	(R)	0
	Fargo	37	42	10	10	T	.01	.12	(R)	0
	Huron	35	41	0	10	0	0	T		0
	Miles City	31	33	10	10	-	-	.01	(S)	0
	Rapid City	26	43	0	0	0	0	T	(S)	0
	Williston	33	33	10	10	.02	0	.08	(S)	T
10/21	Aberdeen	37	41	-	10	0	0	T		0
	Bismark	36	37	10	10	0	0	.03	(S)	0
	Fargo	38	39	10	9	0	T	.07	(R)	0
	Huron	35	44	2	6	0	0	T		0
	Miles City	29	32	8	9	-	-	T		T
	Rapid City	33	38	10	10	T	0	T	(S)	T
	Williston	32	33	10	9	.01	0	T	(S)	T
10/22	Aberdeen	34	41	7	8	0	0	T		T
	Bismark	33	39	10	8	0	0	0		T
	Fargo	36	38	10	10	T	0	T		0
	Huron	31	42	0	3	0	0	0		0
	Miles City	25	38	0	7	-	-	0		0
	Rapid City	24	43	3	8	0	0	0		0
	Williston	27	32	7	10	0	T	T	(S)	0
10/23	Aberdeen	35	46	10	4	0	0	0		0
	Bismark	36	43	10	3	0	0	0		0
	Fargo	34	39	10	10	0	0	0		0
	Huron	32	46	3	5	0	0	0		0
	Miles City	23	37	1	0	-	-	0		0
	Rapid City	29	42	0	0	0	0	0		0
	Williston	27	40	10	0	0	0	0		0
10/24	Aberdeen	31	54	0	4	0	0	0		0
	Bismark	33	48	0	7	0	0	0		0
	Fargo	33	49	0	8	0	0	0		0
	Huron	36	57	0	1	0	0	0		0
	Miles City	35	44	5	10	-	-	0		0
	Rapid City	36	57	0	3	0	0	0		0
	Williston	30	42	5	7	0	0	T		0
10/25	Aberdeen	38	37	10	10	0	0	0		0
	Bismark	34	39	10	10	0	0	0		0
	Fargo	38	42	10	10	0	0	0		0
	Huron	43	40	8	10	0	0	0		0
	Miles City	33	44	10	10	-	-	T		0
	Rapid City	34	54	1	1	0	0	0		0
	Williston	30	42	10	10	T	0	T		0
10/26	Aberdeen	46	56	0	4	0	0	0		0
	Bismark	41	57	3	10	0	0	0		0
	Fargo	43	53	0	7	0	0	0		0
	Huron	46	61	0	0	0	0	0		0
	Miles City	44	52	0	10	-	-	T		0
	Rapid City	53	65	0	5	0	0	0		0
	Williston	39	50	6	10	0	0	T	(R)	0

TABLE 3

Year 1984	Site	Air Temp (°F) 00	Air Temp (°F) 12	Cloud Cover (x/10) 00	Cloud Cover (x/10) 12	Precip. (in.) 00	Precip. (in.) 12	Precip. (in.) 24h	Precip. (in.) Rem	Snow Pack (in.) 24h
12/2	Aberdeen	17	10	10	4	T	0	T	(S)	2
	Bismark	14	19	10	10	T	T	.01	(S)	1
	Fargo	8	3	10	10	T	T	T	(S)	T
	Huron	19	14	10	1	.01	T	.07	(S)	6
	Miles City	13	11	10	9	-	-	.01	(S)	4
	Rapid City	19	19	4	4	0	0	T	(S)	T
	Williston	11	8	10	8	T	0	T	(S)	1
12/3	Aberdeen	4	17	0	4	0	0	T	(S)	2
	Bismark	15	15	10	7	T	T	T	(S)	1
	Fargo	0	10	0	0	0	T	0.1		T
	Huron	5	14	0	0	0	0		T(S)	6
	Miles City	-3	-2	10	1	-	-	0		4
	Rapid City	11	27	0	1	0	0	0		T
	Williston	9	9	10	8	T	T	T	(S)	1
12/4	Aberdeen	13	10	10	0	0	0	0.02	(S)	2
	Bismark	8	15	10	1	T	0	T		1
	Fargo	9	15	10	0	0	0	0		T
	Huron	5	12	6	2	T	0	T	(S)	5
	Miles City	-1	7	0	10	-	-	0		4
	Rapid City	15	24	2	0	0	0	0		T
	Williston	-5	10	0	10	0	0	0		1
12/5	Aberdeen	14	7	3	5	T	0	T	(S)	2
	Bismark	19	-1	4	0	0	0	T	(S)	1
	Fargo	11	-1	10	10	0	0	T	(S)	T
	Huron	15	15	4	7	0	T	T		4
	Miles City	24	13	10	10	-	-	T	(S)	3
	Rapid City	26	19	8	7	0	T	T	(S)	T
	Williston	8	-5	3	3	T	0	T	(S)	1
12/6	Aberdeen	-14	3	0	0	0	0	0		2
	Bismark	-11	20	0	8	0	0	T		1
	Fargo	-8	8	0	3	0	0	0		T
	Huron	-6	11	0	4	0	0	0		4
	Miles City	9	23	0	9	-	-	0		3
	Rapid City	6	44	1	1	0	0	0		T
	Williston	-7	24	0	9	0	0	T		1
12/7	Aberdeen	18	42	7	4	0	0	0		2
	Bismark	30	43	9	8	0	0	0		1
	Fargo	12	43	7	9	0	0	0		T
	Huron	19	42	3	0	0	0	0		3
	Miles City	35	44	4	0	-	-	0		2
	Rapid City	43	61	10	0	0	0	0		0
	Williston	34	43	3	6	0	0	0		1
12/8	Aberdeen	30	36	2	3	0	0	0		T
	Bismark	31	42	7	2	0	0	0		T
	Fargo	30	43	2	5	0	0	0		0
	Huron	31	42	0	4	0	0	0		1
	Miles City	29	33	3	3	-	-	0		1
	Rapid City	33	51	0	10	0	0	0		0
	Williston	31	37	7	8	0	0	0		T
12/9	Aberdeen	-	46	-	7	0	0	0		T
	Bismark	31	43	2	3	0	0	0		T
	Fargo	29	40	0	9	0	0	0		0
	Huron	35	39	7	7	0	0	0		T
	Miles City	26	35	5	4	-	-	0		1
	Rapid City	43	58	6	0	0	0	0		0
	Williston	28	37	0	2	0	0	0		0

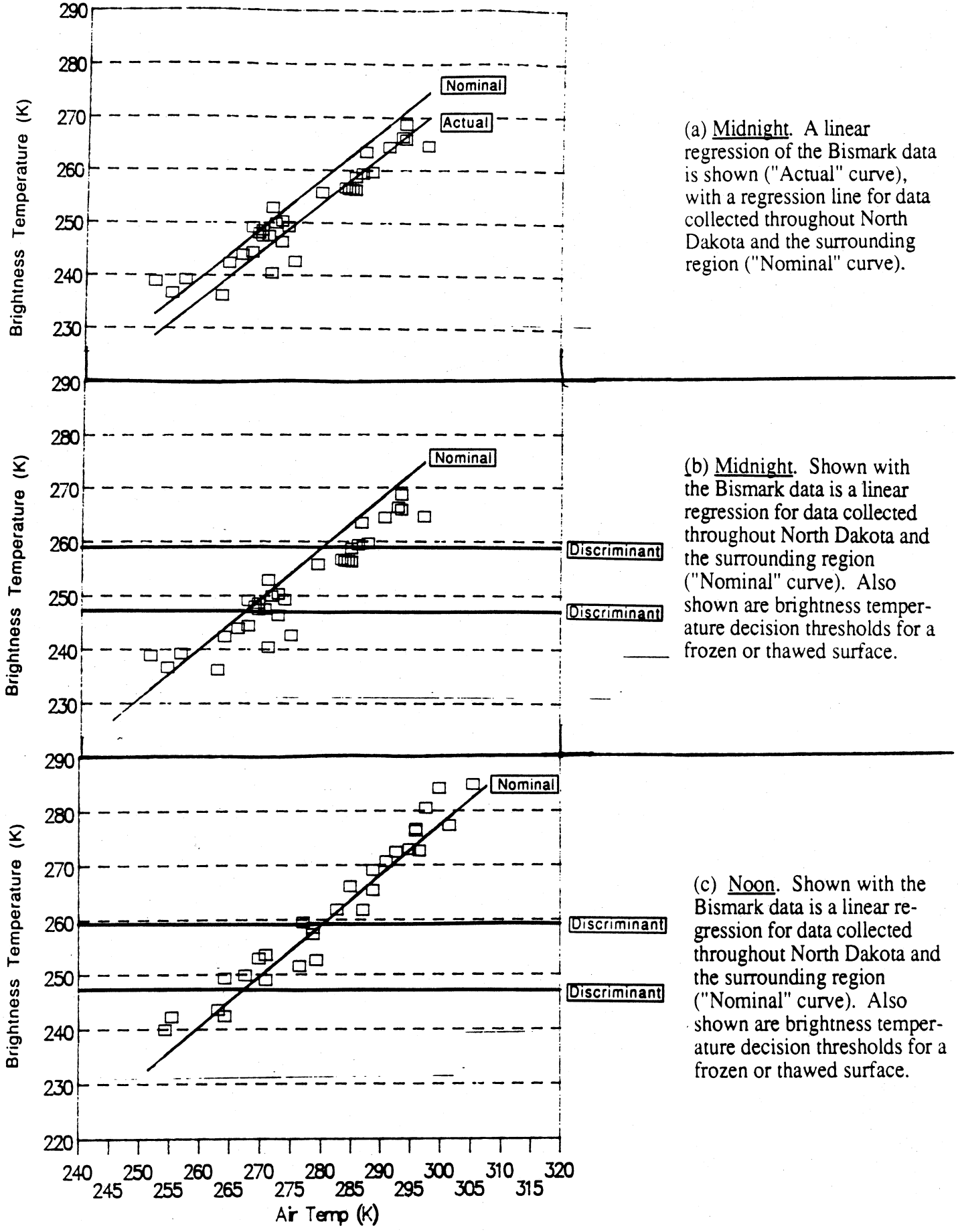

(a) Midnight. A linear regression of the Bismark data is shown ("Actual" curve), with a regression line for data collected throughout North Dakota and the surrounding region ("Nominal" curve).

(b) Midnight. Shown with the Bismark data is a linear regression for data collected throughout North Dakota and the surrounding region ("Nominal" curve). Also shown are brightness temperature decision thresholds for a frozen or thawed surface.

(c) Noon. Shown with the Bismark data is a linear regression for data collected throughout North Dakota and the surrounding region ("Nominal" curve). Also shown are brightness temperature decision thresholds for a frozen or thawed surface.

Figure 1. 37 GHz SMMR brightness temperature versus measured surface air temperature, Bismark, North Dakota. Data were collected from 8/1/84 to 12/31/84.

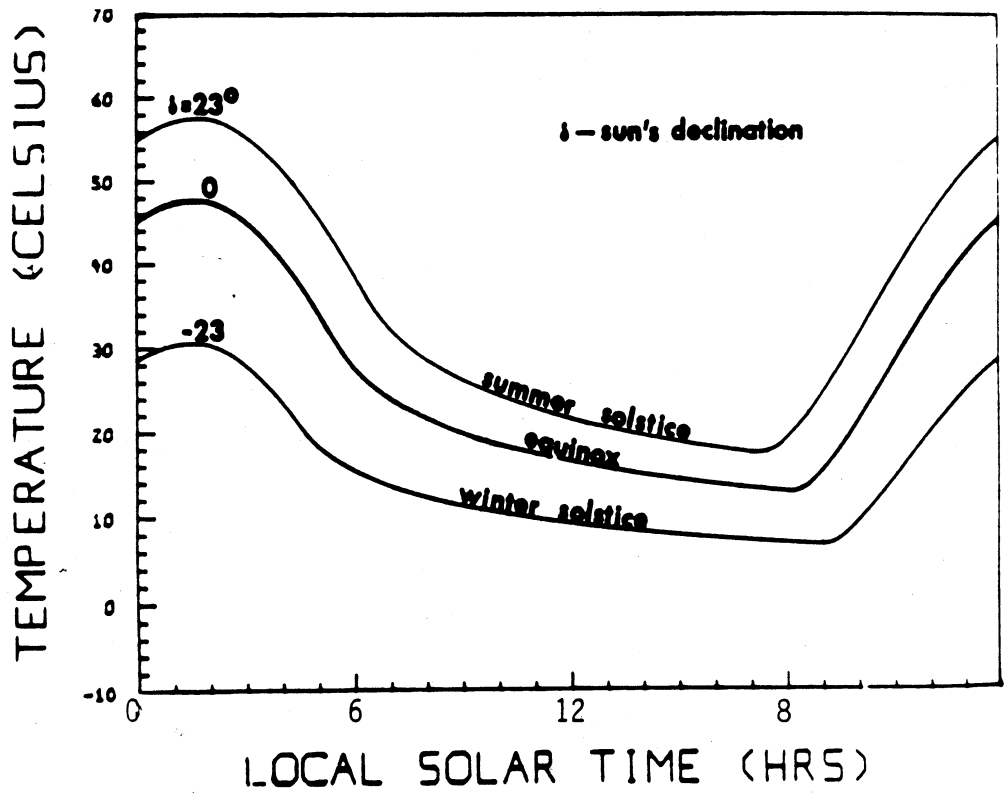

Figure 2. Diurnal surface temperature variation for different seasons at 30° N (from Watson, et al., 1983). Subsurface temperatures will exhibit a reduced amplitude and a phase lag with respect to the surface temperature. That is, midnight thermal gradients will be negative, and noon thermal gradients will be positive.

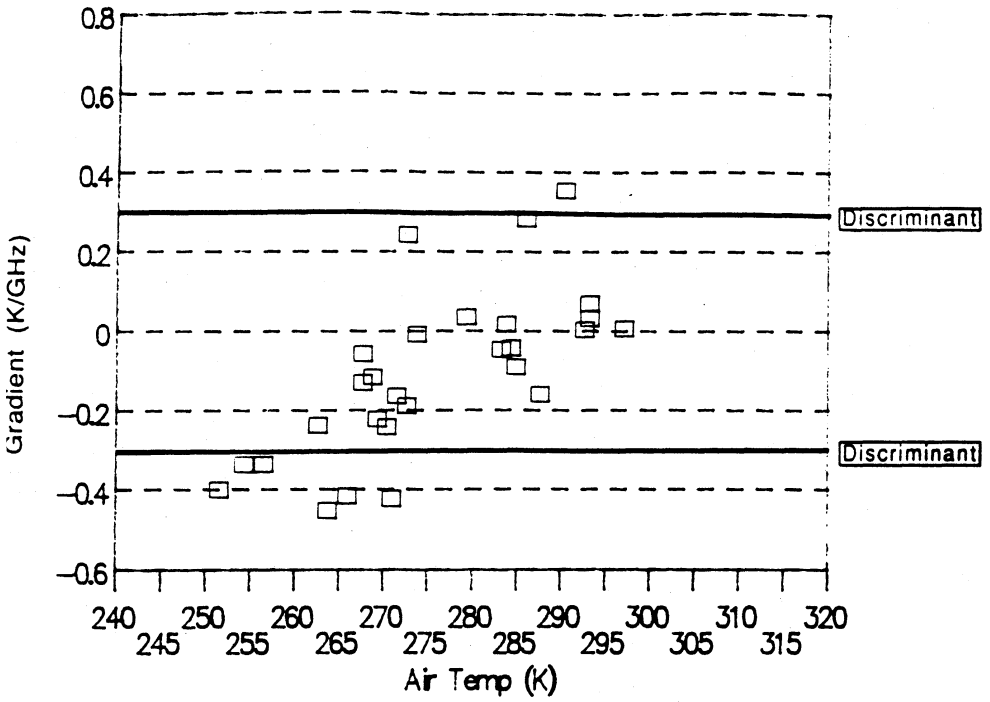

(a) Midnight

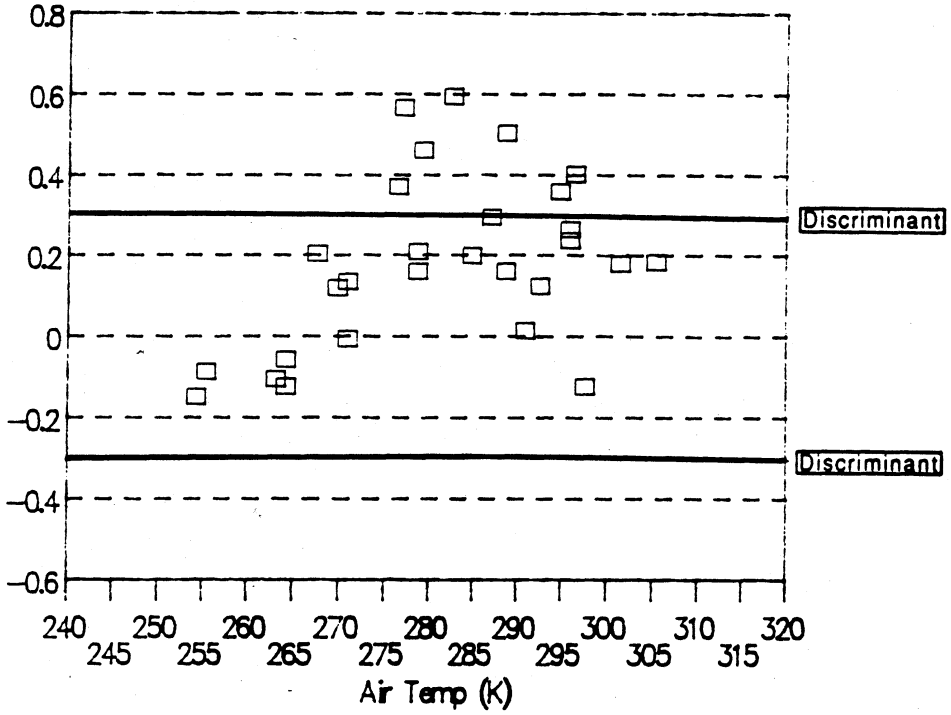

(b) Noon

Figure 3. Frequency gradient versus measured surface air temperature, Bismark, North Dakota. Data were collected from 8/1/84 to 12/31/84. The frequency gradient is the frequency regression slope for simultaneous SMMR brightness temperatures at 37GHz, 18 GHz, and 10.7 GHz. Shown with the Bismark data are frequency gradient decision thresholds for a frozen or thawed surface.

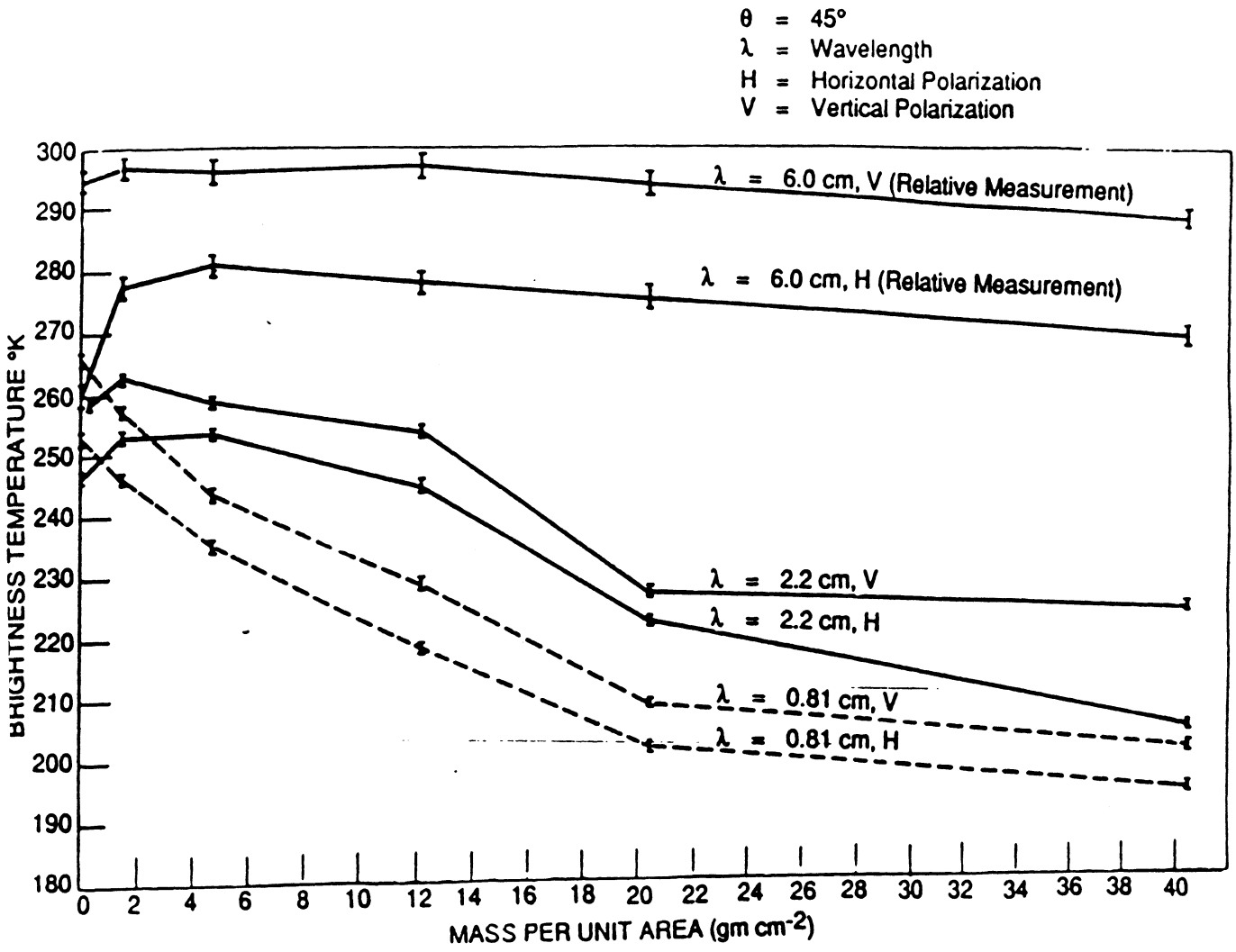

Figure 4. Brightness temperature versus equivalent dry snow, Crater Lake, Oregon, 22 March 1970 (Edgerton et al., 1971). Note the short wavelength darkening evident for thick snowpacks.

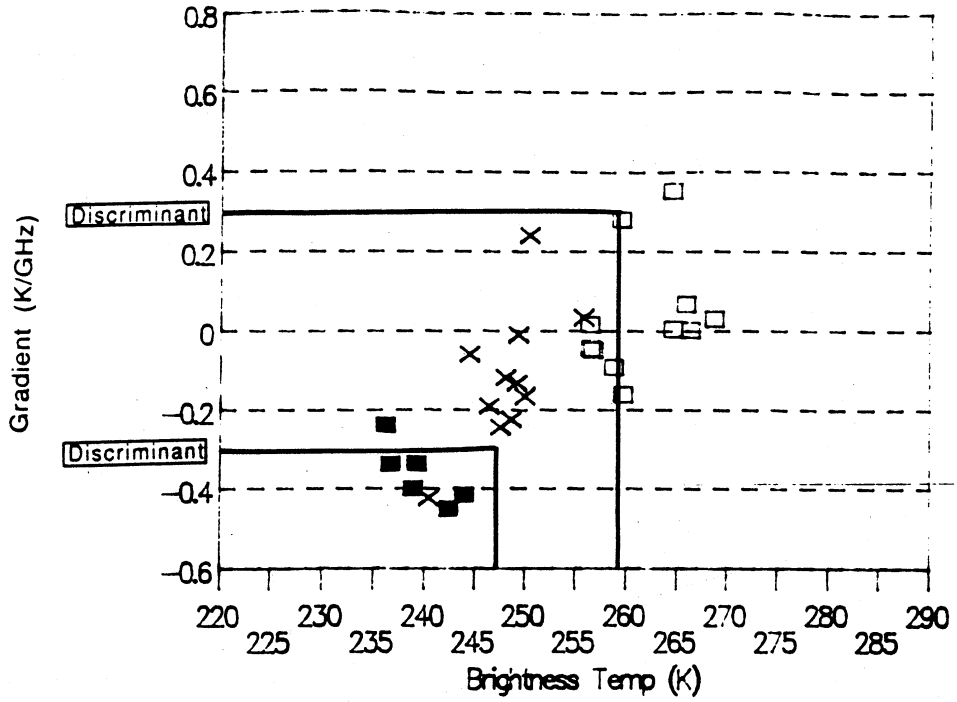

(a) Midnight

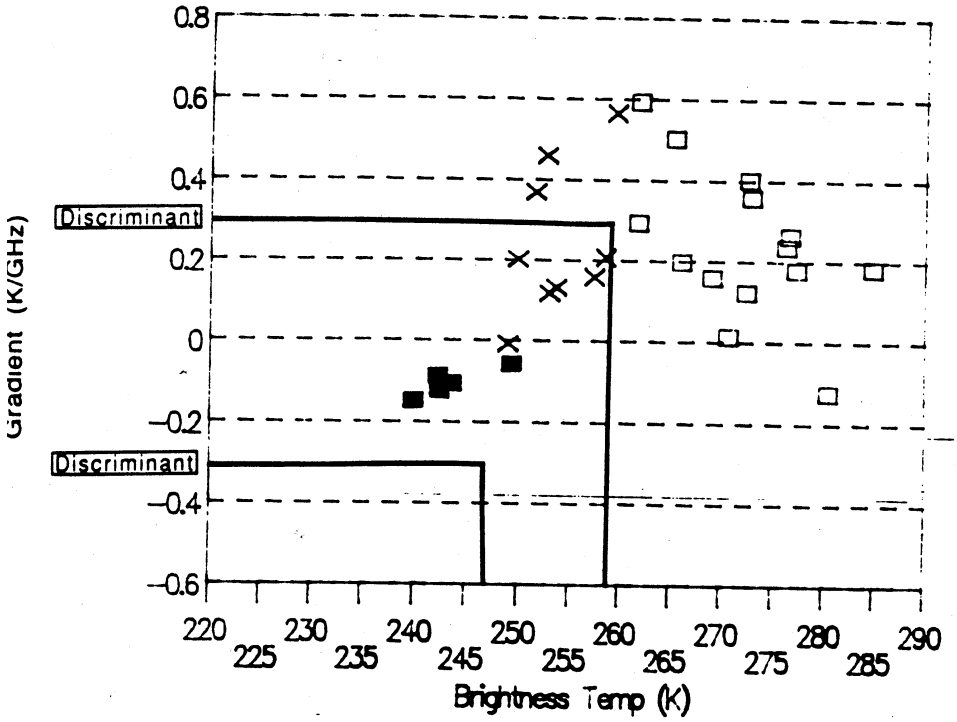

(b) Noon

Figure 5. Frequency gradient versus SMMR 37 GHz brightness temperature, Bismark, North Dakota. Data were collected from 8/1/84 to 12/31/84. Shown with the Bismark data are clustering decision thresholds for a frozen, mixed, or thawed surface. Based upon ground truth, the solid boxes are frozen, open boxes are thawed, and x's are mixed pixels.

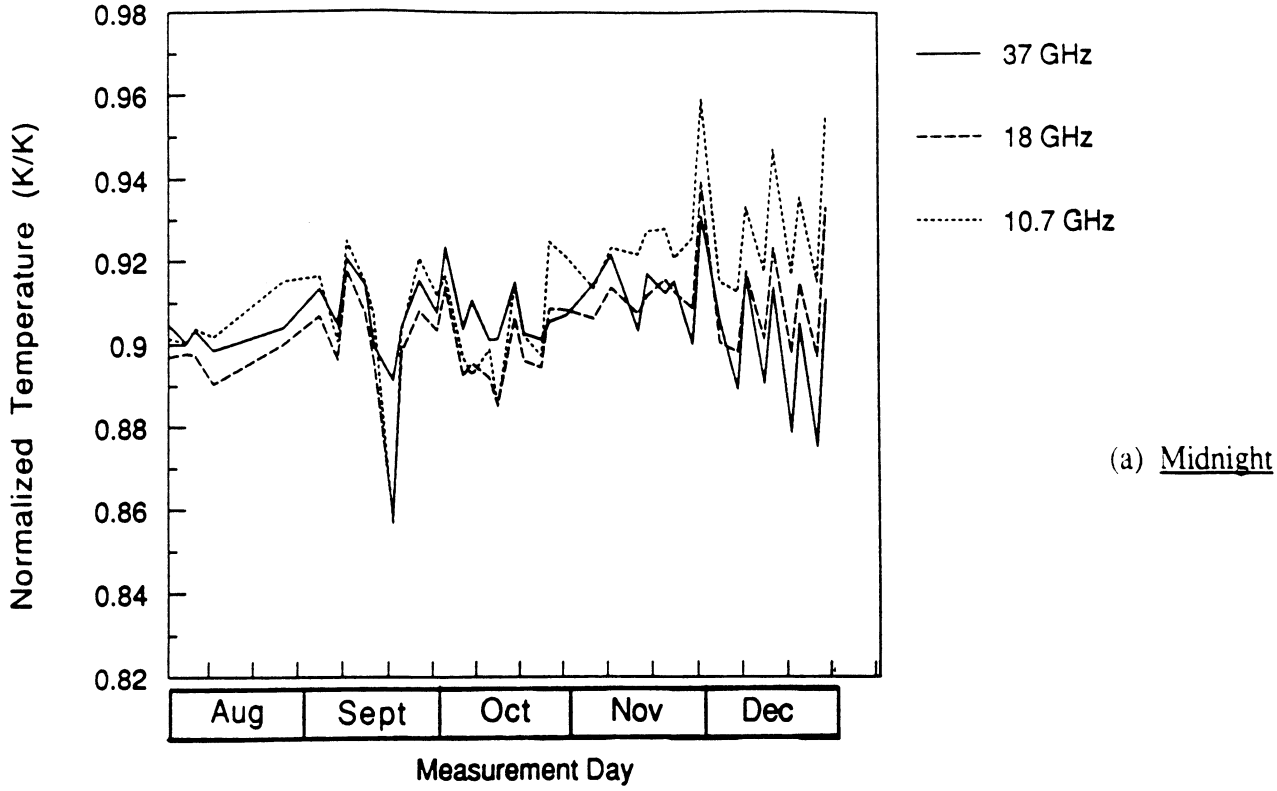

(a) Midnight

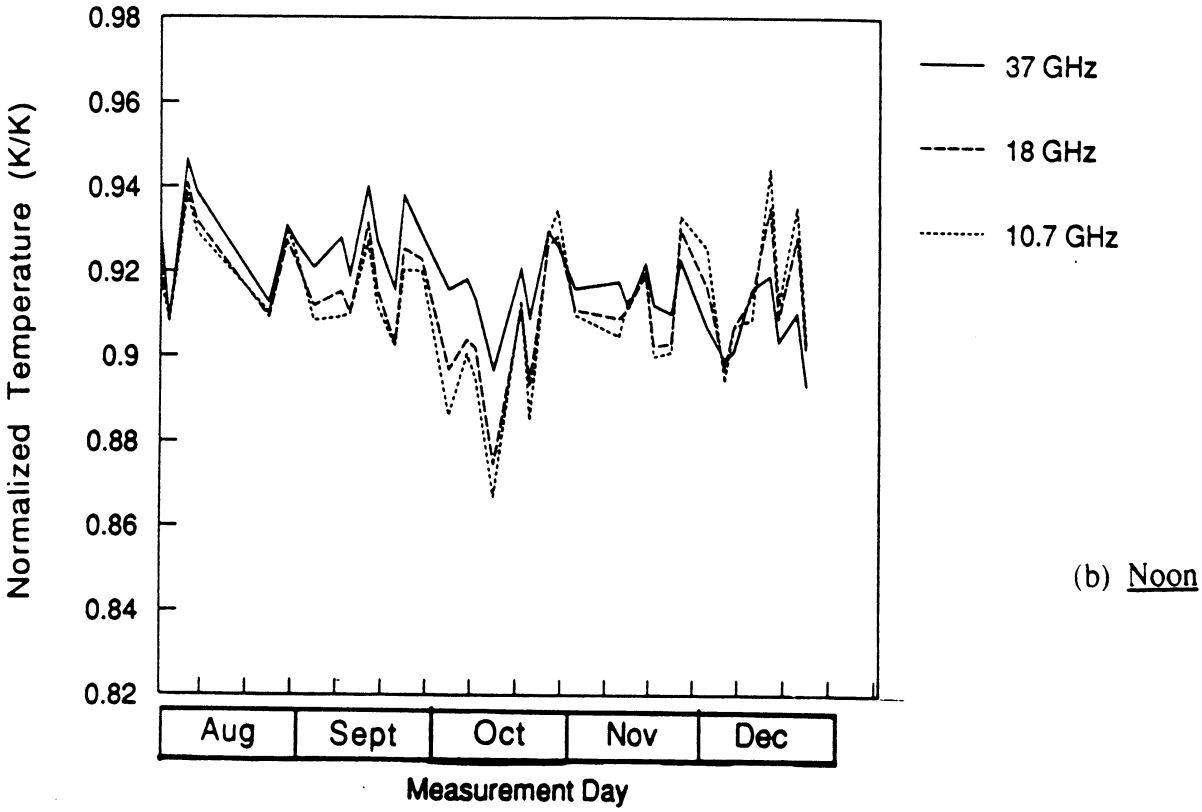

(b) Noon

Figure 6. 37 GHz, 18 GHz, and 10.7 GHz SMMR normalized brightness temperatures versus calender day. Measurements were made at irregular intervals from 8/1/84 to 12/31/84. The normalized brightness temperature of a single SMMR frequency channel is the average brightness divided by the average surface air temperature, averages are calculated over North Dakota and the surrounding region.

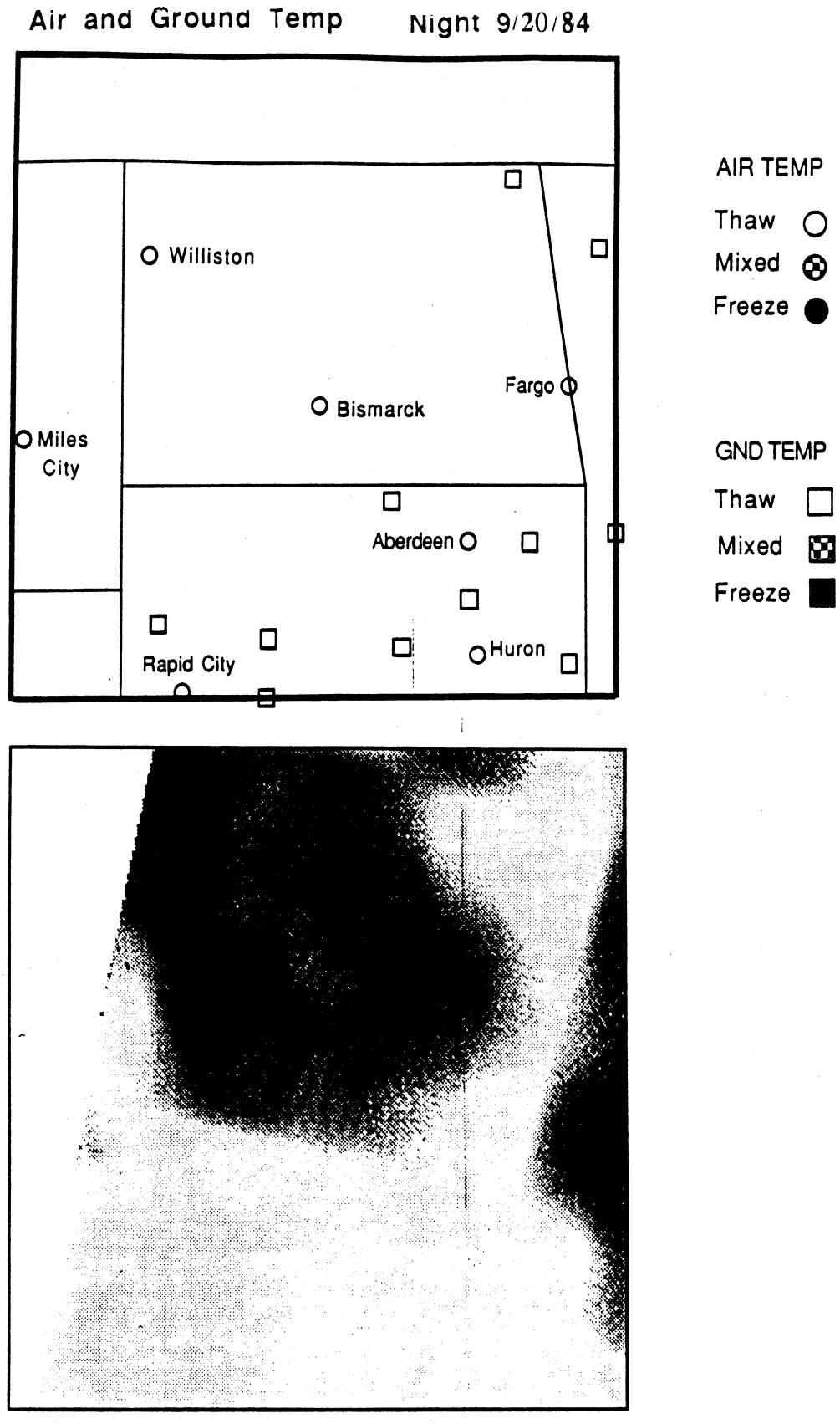

Figure 7. A comparison of reported air and ground temperatures with the Freeze Indicator for midnight, September 20, 1984.

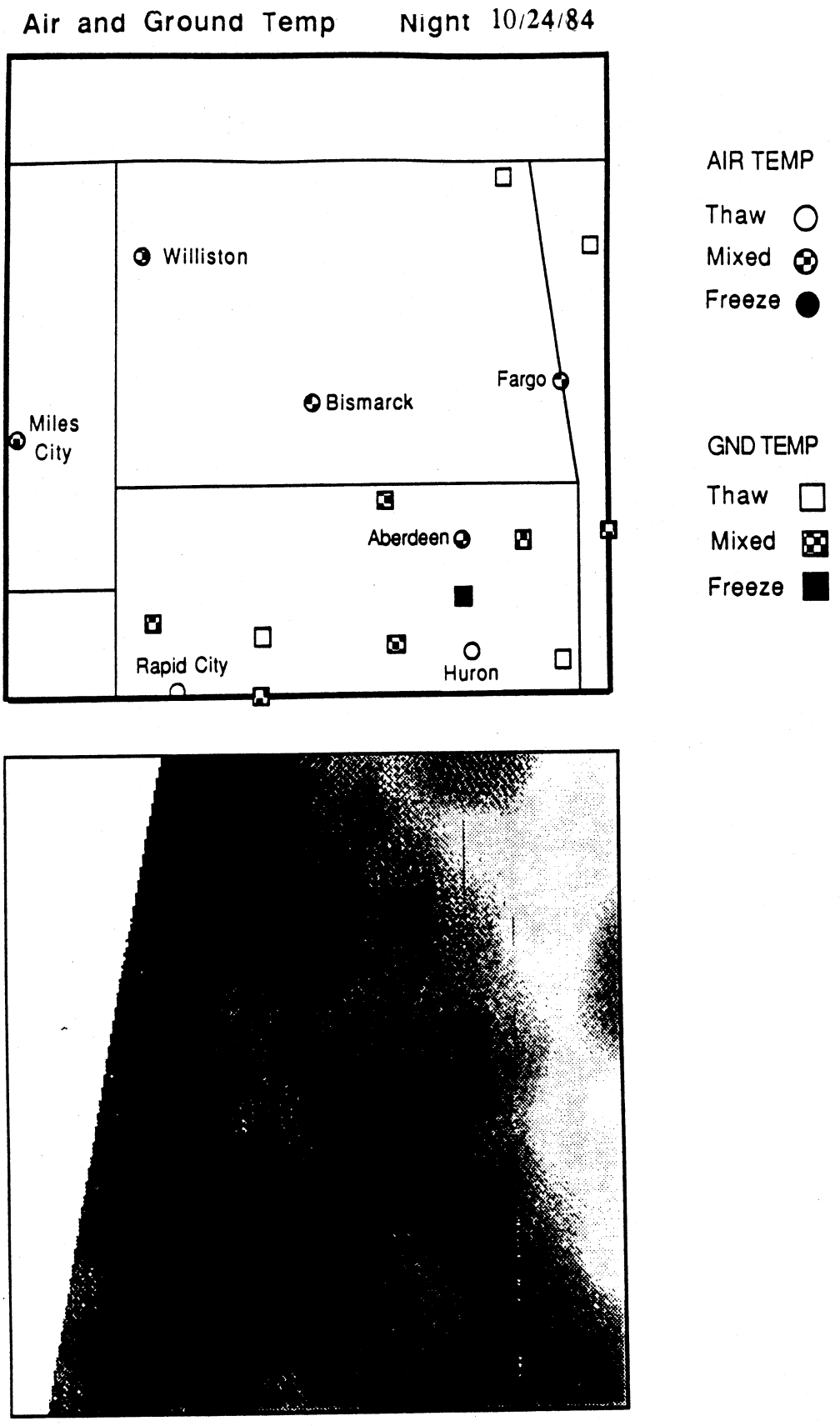

Figure 8. A comparison of reported air and ground temperatures with the Freeze Indicator for midnight, October 24, 1984.

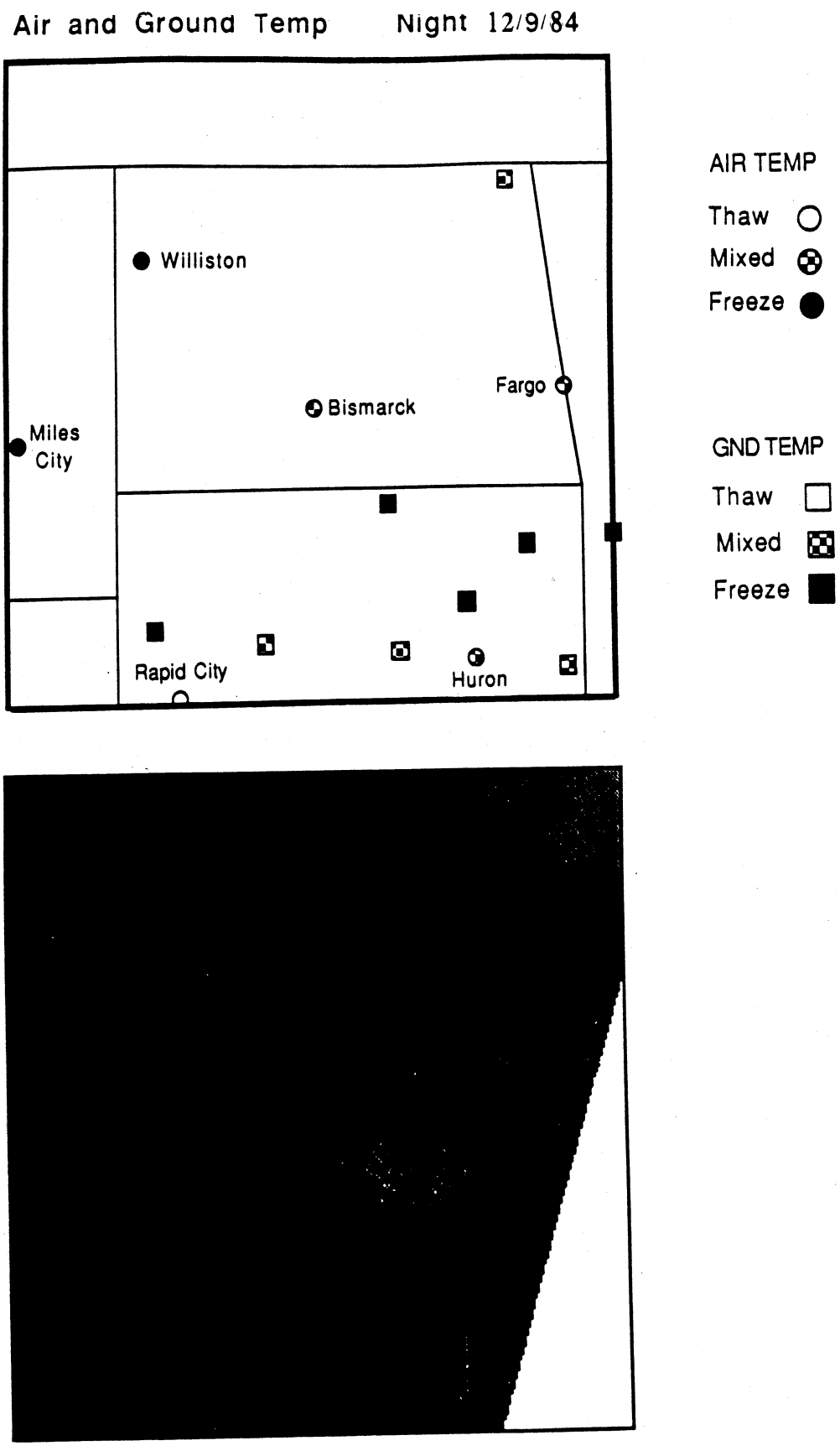

Figure 9. A comparison of reported air and ground temperatures with the Freeze Indicator for midnight, December 9, 1984.

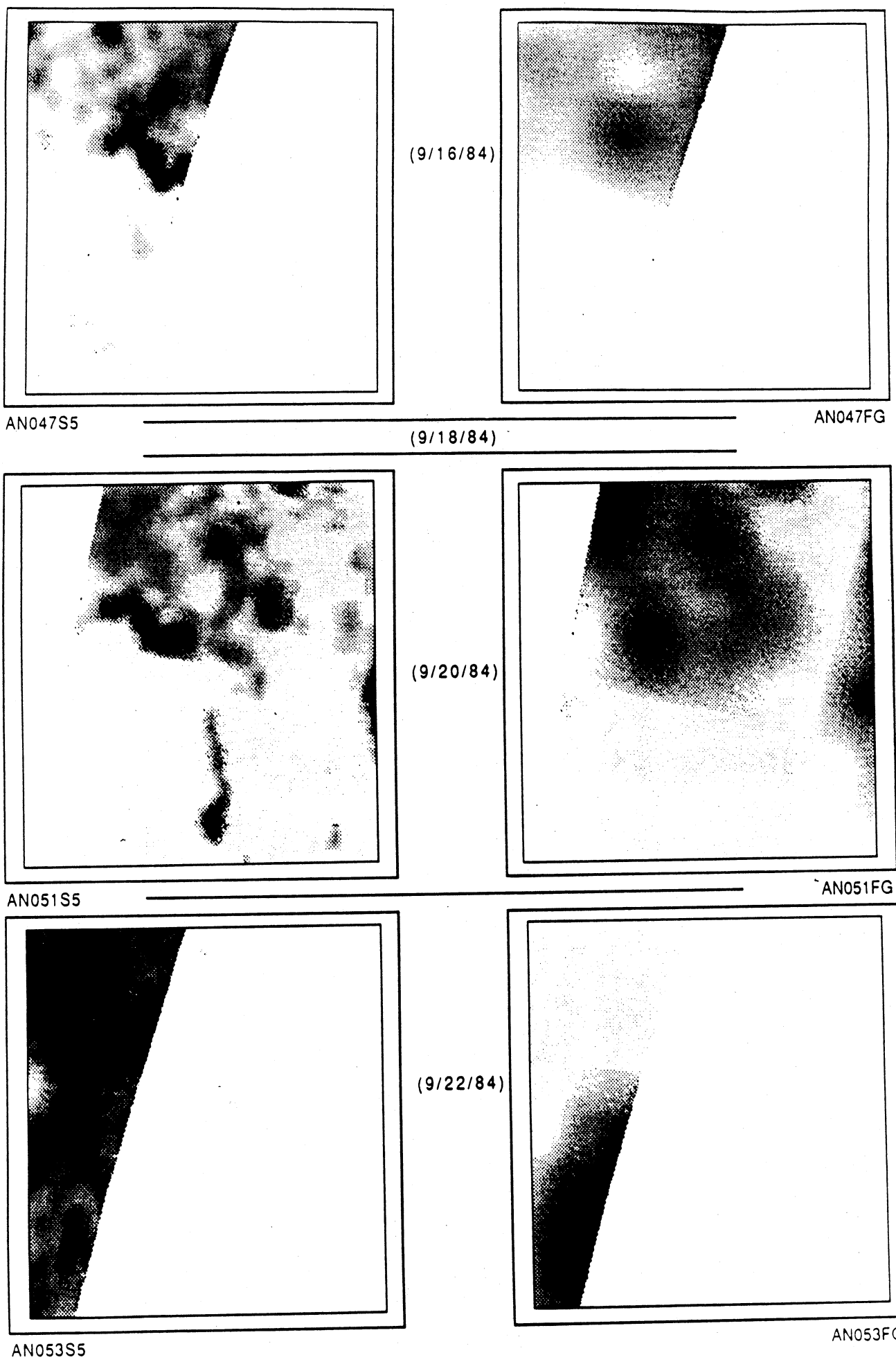

gure 10(a). Midnight 37 GHz and Freeze Indicator image sequences for a 6 day period in September.

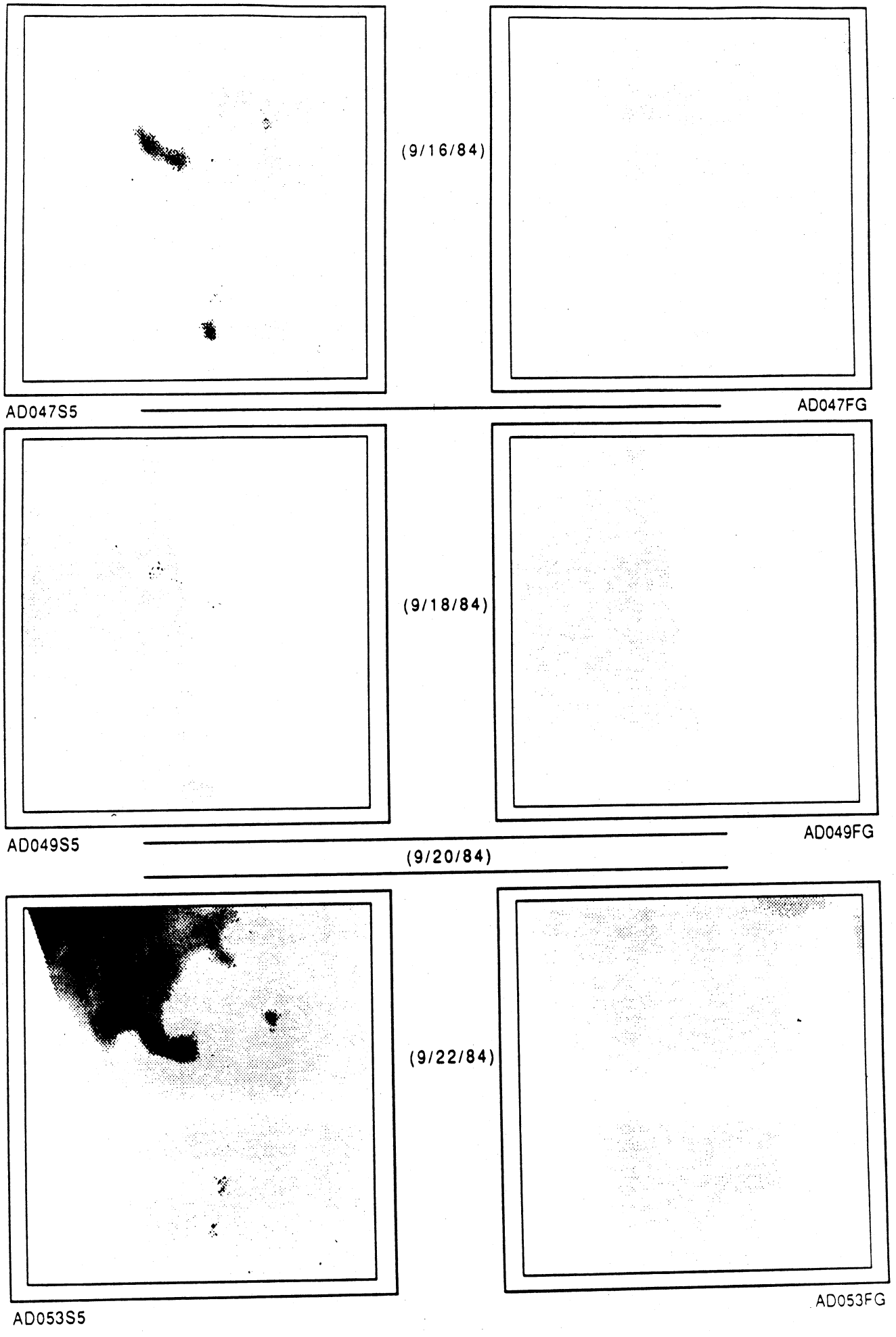

Figure 10(b). Noon 37 GHz and Freeze Indicator image sequences for a 6 day period in September.

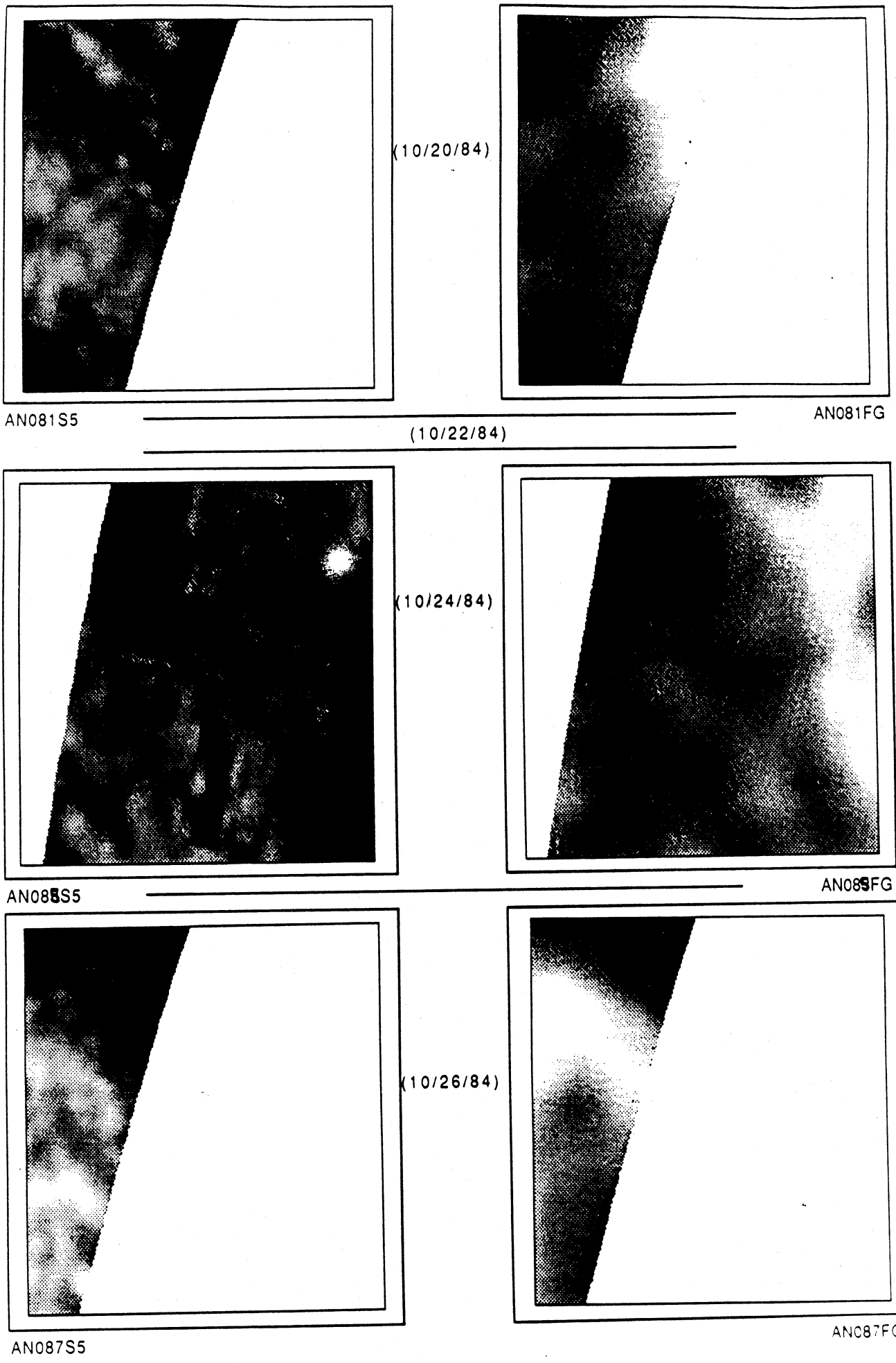

Figure 11(a). Midnight 37 GHz and Freeze Indicator image sequences for a 6 day period in October.

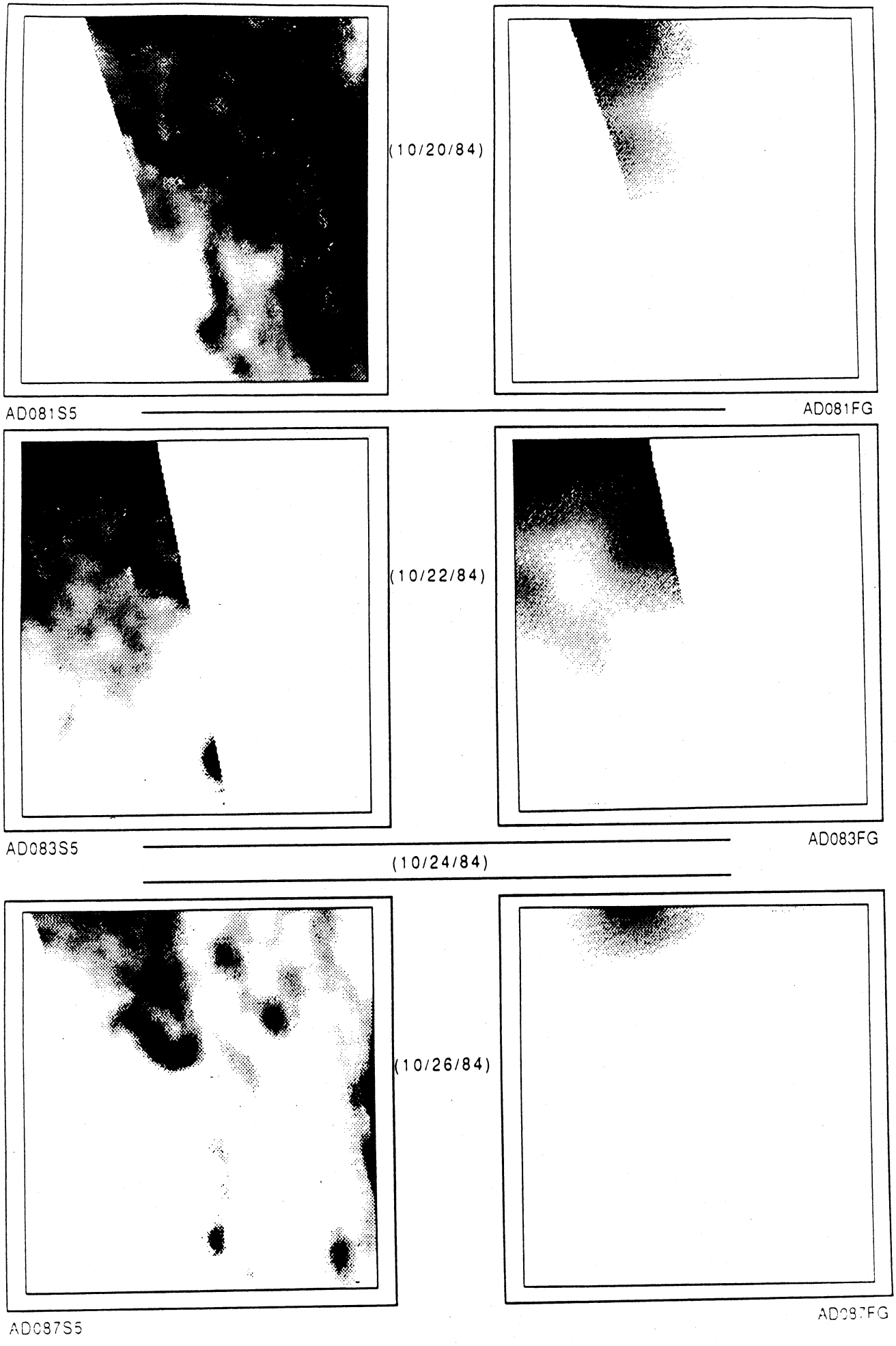

Figure 11(b). Noon 37 GHz and Freeze Indicator image sequences for a 6 day period in October.

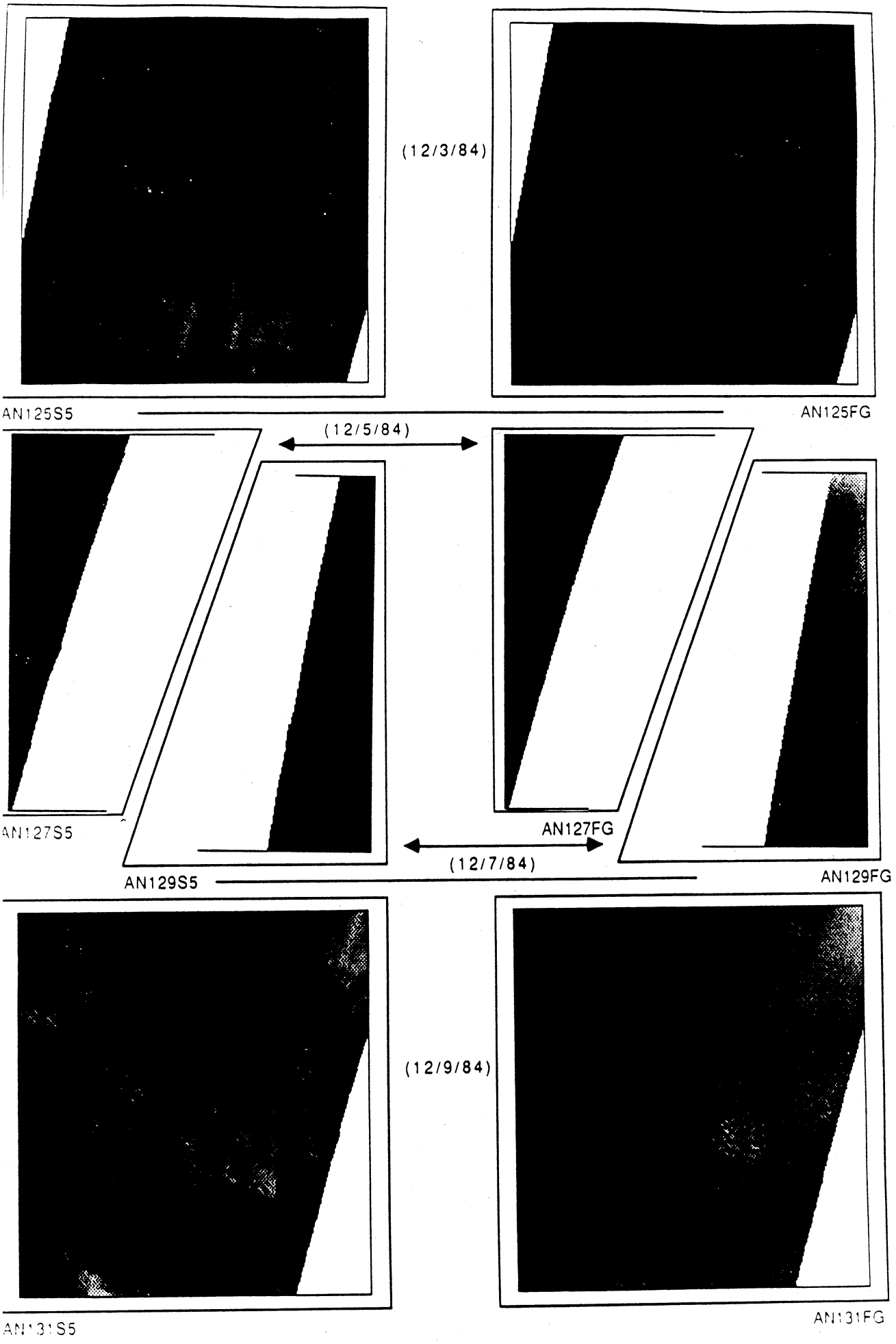

Figure 12(a). Midnight 37 GHz and Freeze Indicator image sequences for a 6 day period in December.

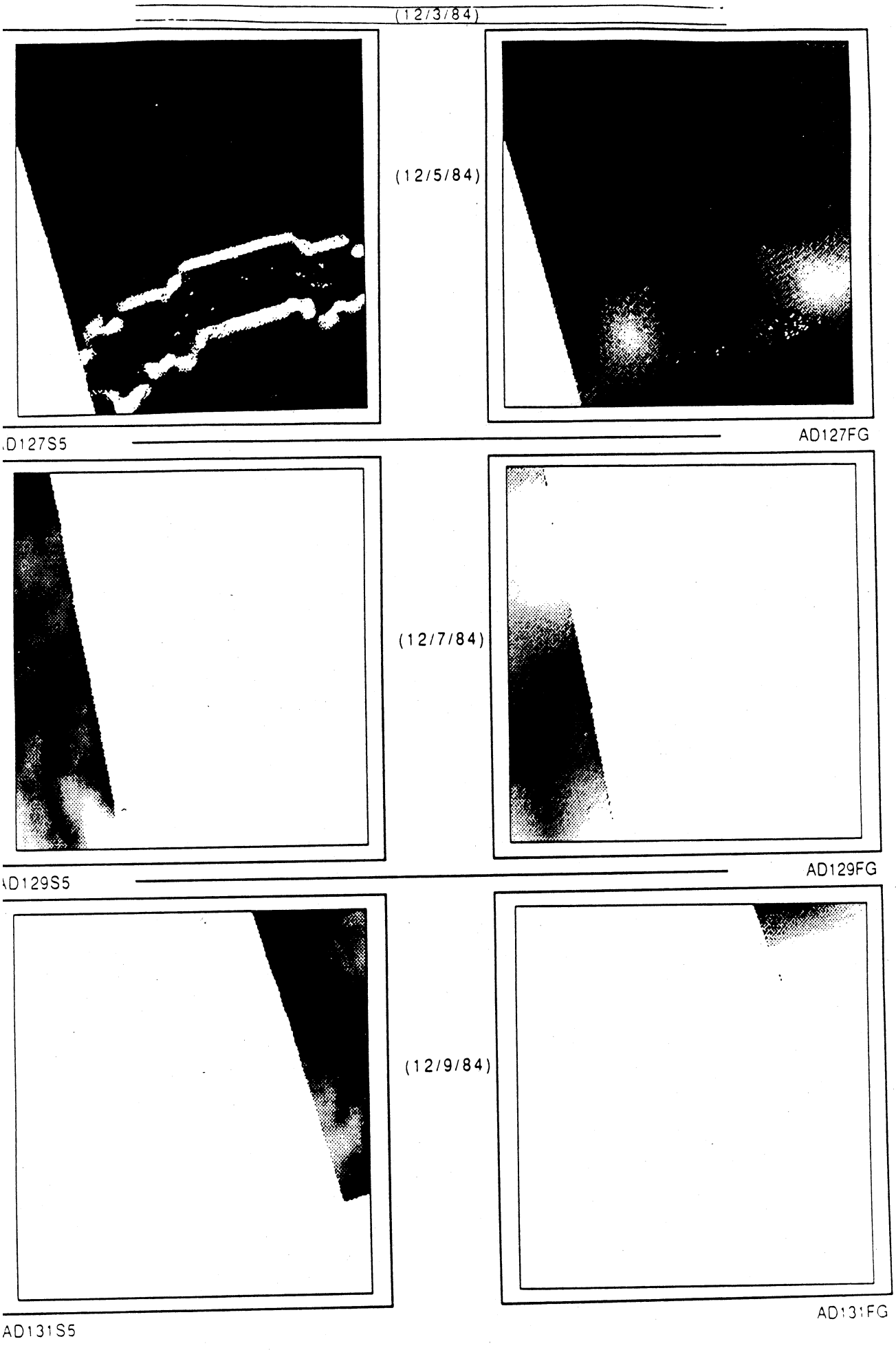

Figure12(b). Noon 37 GHz and Freeze Indicator image sequences for a 6 day period in December. The jagged white lines in the Noon, 12/5/84, image are caused by missing data.

RADIOBRIGHTNESS OF PERIODICALLY HEATED, TWO-PHASE MEDIA

A. W. England

Radiation Laboratory
Department of Electrical Engineering and Computer Science
The University of Michigan
Ann Arbor, MI 48109
(313)-763-5534

December 19, 1988

Abstract

Soils that contain liguids or gases that freeze during diurnal insolation will appear radiometrically distinctive. That is, they will appear to have anomalously high thermal inertias caused by the latent heats of fusion or sublimation. The effect should be observable in the diurnal variation of the radiobrightness of freezing moist soils, or in the radiobrightness of Mars soils that are saturated with CO_2 ice.

The 1-dimensional, heat flow equation for moist soils,

$$\frac{\partial E(T)}{\partial t} = \frac{\partial}{\partial z} K(T) \frac{\partial T}{\partial z}$$

is non-linear because both the enthalpy, E(T), and the thermal conductivity, K(T), are non-linear functions of T at freeze/thaw phase boundaries. Furthermore, diurnal insolation may cause phase boundaries at more than one depth, z. The problem is particularly difficult because these phase boundaries propagate and, occasionally, cancel themselves, and because soils that contain clay freeze over a range of temperatures rather than at 0^o C--that is, they possess diffuse phase boundaries.

The problem of periodic heating of two-phase media has come to be known as Stefan's problem. There are several numerical techniques for its solution. The Chernous'ko method was most readily modified for diffuse phase boundaries, and was developed as a modeling tool for examining the radiobrightness of diurnally heated soils. These models exhibit diurnal radiobrightness spectral gradients similar to those computed from the 10.7, 18, and 37 GHz radiobrightness temperatures from the Scanning Multichannel Microwave Radiometer (SMMR) on Nimbus-7 (reported in a separate abstract, England, et al), and may explain the anomalously flat radiobrightness spectrum of Mars.

The Radiobrightness Measurement of Apparent Thermal Inertia

A. W. England
Radiation Laboratory
Department of Electrical Engineering and Computer Science
The University to Michigan
Ann Arbor, MI 48109
(313)-936-1340

Abstract

Thermal inertia is a measure of a material's resistance to change in temperature. If a material's thermal conductivity, K, and its volumetric heat capacity, ρc, are independent of temperature, then its thermal inertia, P, is $(K\rho c)^{1/2}$. Thermal inertia, as a geologic mapping tool, has been estimated from the differences in pre-dawn and afternoon thermal infrared (TIR) brightnesses. Materials that have high thermal inertias exhibit low day-night, TIR brightness differences. Discrimination among geologic materials based upon thermal inertia has been demonstrated both by aircraft experiments, and by the Heat Capacity Mapping Mission (HCMM) satellite experiment.

In principle, thermal inertia can as easily be estimated from day-night differences in microwave radiobrightness temperatures. The advent of the Special Sensor Microwave/Imager (SSM/I) class of satellite instruments, with their 6:00 am and 6:00 pm daily coverage over most of the Earth, invites thermal inertia mapping. However, the spatial scales of appropriate microwave targets are very different from the spatial scales of HCMM targets. HCMM had a spatial resolution of 600 m, and SSM/I resolutions vary from 15 km at 85.5 GHz to 69 km at 19.35 GHz.

For the coarse resolutions of the SSM/I instrument, appropriate thermal inertia targets would have to be regionally extensive such as soil moisture or snow wetness. To test thermal inertia's sensitivity to soil moisture, thermal models of diurnally heated, prairie soils containing 10%, 15% and 20% by weight moisture were developed for a typical September through December period near Bismarck, North Dakota. Thermal profiles from these models were incorporated in radiobrightness models for each of the SSM/I frequencies to produce expected diurnal radiobrightnesses and spectral gradients for the study period. This combination of models has also been used to explain the day-night shift in the spectral gradient of radiobrightness that is observed in Scanning Multichannel Microwave Radiometer (SMMR) data, and to guide development of an algorithm for classifying frozen soils.

Prior to the onset of night-time freezing, the day-night radiobrightness differences show only weak sensitivity to moisture content. However, once diurnal freezing and thawing begins, the latent heat of fusion of moisture in soil greatly enhances the soil's apparent thermal inertia, and this enhancement is strongly dependent upon the quantity of available moisture. This enhanced sensitivity of apparent thermal inertia to moisture content is most evident in the October and November profiles. The full effects of freezing and thawing are not realized during September because soils are only partially frozen during a clear, September night, nor are they realized in December because soil surfaces are only partially thawed during a typical December day. Furthermore, the models assume a snow-free surface and, thus, are less appropriate for late fall in North Dakota.

AN OPTIMIZED APPROACH TO MAPPING FREEZING TERRAIN WITH SMMR DATA

B. Zuerndorfer, A. W. England, F. T. Ulaby

Radiation Laboratory
Department of Electrical Engineering and Computer Science
The University of Michigan
Ann Arbor, MI 48109
(313)-763-5534

November 17, 1989

Abstract

Soil moisture contributes to the energy exchange between the air and the ground through latent heats of fusion and vaporization. Consequently, the processes of thawing frozen ground or of evaporating soil moisture cause soil thermal inertias to appear anomalously high. There is a large body of literature about deriving soil moisture from radiobrightness. Moisture state can also be inferred from radiobrightness [1]. Frozen soil classification is based upon a combination of 37 GHz radiobrightness and spectral gradient, $\partial T_b(f)/\partial f$, where $T_b(f)$ is the radiobrightness at frequency f. Frozen soils appear cold at 37 GHz, and exhibit a negative spectral gradient that is largely caused by volume scatter darkening at the shorter wavelengths.

This two parameter "freeze indicator" has been applied to data from the Scanning Multichannel Microwave Radiometer (SMMR) on Nimbus-7. For these data, the spectral gradient is a linear, least-square fit to the 10.7, 18, and 37 GHz radiobrightnesses. Conceptually, a surface is classified as frozen only if both the 37 GHz radiobrightness and the spectral gradient are sufficiently low. A freeze map is generated by displaying the freeze indicator for each pixel location. However, data processing is complicated by the very different spatial resolutions of the different SMMR frequency channels. Resolution compensation (equalization) must be performed prior to classification so that spatial averaging is similar at all frequencies. Assuming that no a priori surface information is available, common practice for resolution compensation is to degrade the high frequency (fine resolution) data to the resolution of the low frequency (coarse resolution) data. As a result, fine resolution information is lost.

Under certain constraints, fine resolution information can be recovered in the location estimate of the freeze/thaw boundaries [2]. If the constraints are met, the coarse resolution freeze/thaw boundaries can be registered to fine resolution, 37 GHz boundaries (i.e., to 37 GHz radiobrightness threshold crossings). These 37 GHz boundaries become better estimates of freeze/thaw boundary locations than those at coarse resolution.

In this paper, we show that boundary registration can be optimized through clustering. Specifically, 37 GHz radiobrightnesses and spectral gradients from SMMR measurements are grouped into frozen and thawed clusters for an area that includes North Dakota, about half of each neighboring state, and part of Canada for the Fall of 1984. From the intersection of the clusters, fine resolution 37 GHz radiobrightness boundaries are defined that register with the freeze map boundaries. In addition, fine resolution, 37 GHz radiobrightness boundary widths (regions of boundary uncertainty) are also defined.

[1] Zuerndorfer, B. W., England, A. W., Dobson, C. M., and Ulaby, F. T. (1989). "Mapping freeze/thaw boundaries with SMMR data," *J. Agriculture and Forest Meteorology*, under review.

[2] Zuerndorfer, B. W., England, A. W., and Wakefield, G. H. (1989). "The radiobrightness of freezing terrain," *1989 IEEE Int. Geosci. and Remote Sensing Symp.*, Vancouver, Canada.

THE RADIOBRIGHTNESS OF FREEZING TERRAIN

B. Zuerndorfer, A. W. England, and G. H. Wakefield

Radiation Laboratory
Department of Electrical Engineering and Computer Science
The University of Michigan
Ann Arbor, MI 48109

ABSTRACT

The combination of a low 37 GHz radiobrightness and a negative 10.7, 18, and 37 GHz spectral gradient appears to be an effective discriminant for classifying frozen ground. The spatial resolution of lower frequency, satellite borne, microwave radiometers is typically relatively coarse, e.g., 100 Km for the 10.7 GHz channel of SMMR. With certain restrictions, scale-space theory can be used to map freeze/thaw boundaries that are identified at the poorest resolution of a multiband image to images having the highest resolution. That is, the process permits classification at lower resolution, but boundary location at higher resolution.

INTRODUCTION

Soil moisture contributes to the energy exchange between the air and the ground through latent heats of fusion and vaporization. The processes of thawing frozen ground or of evaporating soil moisture cause soil thermal inertias to appear anomalously high. Microscale and mesoscale climate models benefit from estimates of the amount and state of soil moisture as part of their boundary conditions.

There is a large body of literature about deriving soil moisture from radiobrightness [e.g. Burke et. al., 1979; Wang et. al., 1982; Blanchard and Chang, 1983; Schmugge, 1983; Jackson et. al., 1984; Camillo and Schmugge, 1984; Schmugge et. al., 1986; and Grody, 1988]. In addition, there is strong evidence that moisture state can also be inferred from radiobrightness. Using data from the Nimbus-7 Scanning Multichannel Microwave Radiometer (SMMR) for a test area that included North Dakota and parts of the surrounding states and southern Canada, Zuerndorfer et. al. [1989] showed that a combination of low 37 GHz radiobrightness and a negative spectral gradient of radiobrightness offers an encouraging Freeze Indicator, or discriminant, for classifying frozen terrain.

A fundamental problem with the Freeze Indicator algorithm developed by Zuerndorfer et. al. [1989] is that radiobrightness measurements from different frequency channels having different spatial resolutions are required to estimate a spectral gradient. To make each radiobrightness value refer to a common area on the ground, data from each channel is compensated to a common, coarse resolution (i.e., the resolution of the lowest frequency SMMR channel that contributes to the gradient estimate). As a result, identified freeze/thaw boundaries are localized only to the accuracy of the resolution of the lowest frequency channel that was used.

In this paper, we present a technique for using the fine resolution in the high frequency channel to improve the localization of freeze/thaw boundaries. By using Gaussian convolution, or Gaussian filtering, to perform resolution compensation, it becomes possible to register boundaries observed at coarse resolution to those observed at fine resolution. In the sections that follow, we review the Freeze Indicator work of Zuerndorfer et. al. [1989], and discuss the use of Gaussian filtering for resolution compensation and its application to freeze/thaw boundary mappings.

FREEZE INDICATOR

Freezing influences the measured radiobrightness temperature, T_b, of the ground, as observed by a satellite microwave radiometer, through parameters in the approximation [Ulaby et. al., 1981],

$$T_b = e\,T_o + (1 - e)\,T_{sky},$$

where e and T_o are the emissivity and surface temperature of the ground, respectively, and T_{sky} is the effective sky brightness. Atmospheric transmissivity is ignored in this approximation. Frozen ground exhibits signatures of (1) lower thermal temperatures, T_o, (2) higher emissivity, e, and (3) a decrease in brightness temperatures with microwave frequency,

$$\frac{\partial T_b}{\partial f} < 0.$$

Signatures (1) and (2) are well understood, but are generally ambiguous indicators of frozen ground. Ambiguities arise because changes in radiobrightness that result from freezing the ground may be either positive or negative, depending upon the soil moisture content. A typical dry soil emissivity of 0.8 will yield a 8° radiobrightness decrease for a 10° decrease in thermal temperature (enough to completely freeze the ground), with relatively little change in soil emissivity. However, in moist soils, freezing causes an increase in soil emissivity, and a subsequent increase in radiobrightness.

Water molecules in frozen plants and soils are not free to align themselves with microwave electric fields. This constraint upon the rotational freedom of water gives rise to an apparent dryness of frozen plants and soils. The consequence is a decrease in the real part of the dielectric constant, ε', and an increase in soil emissivity. For example, the real part of dielectric constants, ε', and corresponding emissivities at nadir, e(0), of two, homogeneous, smooth surfaced, 15% moist soils at 10 GHz are (ε' from Hoekstra and Delaney [1974]):

	+ 5° C			- 5° C		
Material	ε'	e(0)	T_b	ε'	e(0)	T_b
Goodrich Clay	8.2	0.77	221	4.9	0.86	235
Fairbanks Silt	9.6	0.74	214	4.1	0.89	242

Because of increasing emissivity with freezing, a 10° decrease in the clay or silt soil temperatures, from +5° C to -5° C, would cause an increase in T_b of approximately +14 K or +28 K, respectively. The positive direction of change in T_b with soil freezing will cause confusion in discrimination between soils that are frozen and cold, and soils that are warm and dry.

The shift in emissivity with freezing is most pronounced at the lower microwave frequencies. At 37 GHz, the effect is reduced, although not absent. Because the 37 GHz radiobrightness is less dependent upon soil moisture, it does exhibit a stronger correlation with air temperature than do the lower frequency radiobrightnesses. This higher correlation also occurs because air and surface temperatures tend to agree, while air and subsurface temperatures (i.e., those temperatures that influence longer wavelength radiobrightness) often differ. That is, the 37 GHz radiobrightness offers a more reliable estimate of sub-zero soil surface temperatures than do lower frequency radiobrightnesses. However, discrimination based only on 37 GHz radiobrightness would misclassify too often.

Zuerndorfer et. al. [1989] suggest a third signature of frozen soil. Freezing reduces the imaginary part of the dielectric constant, ε'', proportionally more than it does the real part, ε'. The loss tangent, $\tan\delta = \varepsilon''/\varepsilon'$, is a measure of the attenuation per microwave wavelength. Reduced loss tangent, or lower attenuation, means that thermally emitted photons originate deeper within emitting media. That is, the effective depth of emission, z_e, ($1-e^{-1}$ of the emission originates above z_e) becomes a larger fraction of the free-space wavelength, λ_0 [England, 1974, 1975, 1976, and 1977]. For example, Goodrich Clay and Fairbanks Silt exhibit the following increase of z_e with freezing (data from Hoekstra and Delaney [1974]):

	+ 5° C				-5°C			
Material	ε'	ε''	tan δ	z_e	ε'	ε''	tan δ	z_e
Goodrich Clay	8.2	3.5	0.43	0.13 λ_0	4.9	1.0	0.20	0.36 λ_0
Fairbanks Silt	9.6	5.0	0.52	0.10 λ_0	4.1	0.02	0.005	15.7 λ_0

The effective emission depth of moist soils is typically 10% of the free-space wavelength. Frozen soils have effective emission depths that may be 30% or more of free-space wavelengths. The effective emission depth of frozen sandy soils, like the Fairbanks Silt, can be several wavelengths. In the more transparent emitting media, such as frozen soil or dry snow, the greater average thermal photon path length has the effect of providing a greater opportunity for volume scattering of photons.

Volume scattering occurs because soils and plants appear increasingly heterogeneous at the scales of shorter microwave wavelengths. These heterogeneities scatter thermally emitted photons before they escape through the soil surface, and the scattering is increasingly severe at shorter wavelengths. This "law of darkening" means that for an isothermal volume scattering halfspace,

$$\frac{\partial T_b}{\partial f} < 0$$

[England, 1974]. Frozen terrain may also be snow covered. Because snow is exceedingly transparent and relatively heterogeneous to microwaves, snow exhibits significant of darkening [Edgerton et. al., 1971]. That is, both frozen soil and snow can cause negative spectral gradients.

Neither a low 37 GHz radiobrightness nor a negative spectral gradient is solely adequate as a discriminant for classifying frozen soils at the relatively coarse resolutions of the Nimbus-7 SMMR. However, a 2-parameter, freeze signature comprised of the 37 GHz radiobrightness and the 10.7, 18, and 37 GHz spectral gradient, offers a promising initial discriminant for the classification of frozen soil. The preliminary decision boundaries that the soil is frozen are:

(1) $T_b(37\ \text{GHz}) < 247\ \text{K}$,

(2) 3-frequency, spectral gradients $< \frac{-0.3\text{K}}{f(\text{GHz})}$.

BOUNDARY LOCALIZATION

In the Freeze Indicator of Zuerndorfer et. al. [1989], spectral gradients were estimated using linear regressions of SMMR 37 GHz, 18 GHz, and 10.7 GHz radiobrightness measurements. The nominal resolutions of these channels are 30 Km, 60 Km, and 100 Km, respectively. Without compensating for the resolution differences between the channels, the spectral gradient estimates can be in error. For example, a non-zero gradient estimate can result from surfaces that have radiobrightnesses that are spatially variant but are constant with frequency. To avoid anomalous gradient estimates, the image data were compensated to a common resolution -- that is, the (coarse) resolution of the lowest frequency channel used in gradient estimation. (Such resolution compensated data is available with the SMMR data [NASA, 1978], and was used in the Freeze Indicator results of Zuerndorfer et. al. [1989]). However, at this poorer spatial resolution, the Freeze Indicator does a relatively poor job of locating freeze/thaw boundaries. That is, the fine resolution information of the 37 GHz channel is lost.

To better use the fine resolution information of the 37 GHz channel, we note that freeze/thaw boundaries exist in images generated from only the higher resolution, 37 GHz data. However, as previously discussed, these boundaries are ambiguous because of classification errors between frozen and dry soils. We would like to identify those boundaries in 37 GHz images that correspond to the boundaries between frozen and thawed surfaces that were classified at coarse resolutions.

Our boundary identification and localization process for SMMR data requires three steps. First, the uncompensated 10.7 GHz, 18 GHz, and 37 GHz SMMR data is read and compensated to the resolution of the 10.7 GHz channel. Due to the inverse relation between spatial resolution and spatial filter bandwidth [Bracewell, 1986], resolution compensation can be achieved by spatial filtering. We use Gaussian filtering for resolution compensation of the 18 GHz and 37 GHz channels (i.e., 37 GHz and 18 GHz data are synthesized at the resolution of the 10.7 GHz channel by Gaussian filtering). The Gaussian filter bandwidths used in resolution compensation are calculated from the uncompensated resolutions of each channel. Second, resolution compensated data are used in the Freeze Indicator algorithm to classify frozen soil surfaces, and to identify freeze/thaw boundaries in images generated from compensated (coarse resolution) 37 GHz data. In our preliminary work, freeze/thaw boundaries for the 37 GHz parameter in the Freeze Indicator are located where the 37 GHz brightness crosses a threshold of 247 K, corresponding to a nominal T_b for a -5° C surface in the test area (i.e., a frozen surface). Third, freeze/thaw boundaries identified in compensated (coarse resolution) 37 GHz images are registered to boundaries observed in uncompensated (fine resolution) 37 GHz images. This is done by tracking boundary locations in 37 GHz images as the amount of resolution compensation is reduced. The resulting boundary locations that are registered in the uncompensated 37 GHz images are used as estimated locations of freeze/thaw boundaries on the surface.

In the boundary identification process, resolution compensation is achieved by Gaussian filtering. Only Gaussian filtering can guarantee that all boundaries observed in the (coarse resolution) compensated 37 GHz images can be registered to boundaries observed in the (fine resolution) uncompensated 37 GHz images. This result follows from scale-space filtering theory in computer vision [Witkin, 1983; Yuille and Poggio, 1986].

Figures 1-4 demonstrate preliminary results of our boundary identification process. Figure 1 shows the Freeze Indicator map of the test area of Zuerndorfer et. al. [1989] for SMMR data of midnight September 20, 1984. A geographical map of the test area -- North Dakota and the surrounding regions -- is included. The Freeze Indicator shows dark pixels for surfaces that are more likely frozen. Figure 2 shows the 37 GHz radiobrightness map of the same region, where the resolution has been compensated to that of the 10.7 GHz channel. Regions of darker pixels represent surface regions of lower radiobrightness. Shown as white pixels are the estimated freeze/thaw boundaries. Figure 3 shows a 37 GHz radiobrightness map of the region at a resolution corresponding to the 18 GHz channel. Figure 4 shows an uncompensated 37 GHz radiobrightness map. Figures 2-4 all show the freeze/thaw boundary.

Based upon the Freeze Indicator map of Figure 1, the dark regions in the 37 GHz radiobrightness map of Figure 2 would be classified as frozen. The localization improvement afforded by the higher resolution data is apparent in tracking the freeze/thaw boundaries from Figures 2-4 (i.e., as resolution in improved). In addition, new regions and boundaries appear as resolution improves, as in the dark islands in the northeast corner of Figure 4. These new regions are distinct from those classified at coarse resolution, and cannot be ascertained from the Freeze Indicator. Thus, classification of the new regions must be determined by other means.

CONCLUSIONS

In Zuerndorfer et. al. [1989], a multiple frequency, Freeze Indicator algorithm was developed which shows promise as a classifier of frozen soil. However, the common (coarse) resolution needed in the classification process results in a Freeze Indicator that has coarse resolution and, subsequently, poor localization of freeze/thaw boundaries. Use of scale-space theory permits the mapping of freeze/thaw boundaries from the coarse resolution of the compensated images to the finer resolution of the 37 GHz image.

A significant limitation to the improvements available in freeze/thaw boundary localization is the performance of the Freeze Indicator in correctly classifying surfaces. Work in determining frozen soil using radiometer data is in its preliminary stages. For the results presented in this paper, simple threshold crossings were used to determine freeze/thaw boundaries in the high frequency radiobrightness maps. Such criteria may not be optimal. As work on the Freeze Indicator develops, a better understanding of freeze/thaw boundaries will ensue and, subsequently, produce better criteria for determining freeze/thaw boundaries in the higher frequency, finer resolution maps.

REFERENCES

Blanchard, B.J., and A.T.C. Chang, 1983, Estimation of soil moisture from Seasat SAR data, Water Res. Bull. 19, pp. 803-810.

Bracewell, R. N., 1986, The Fourier Transform and Its Applications, McGraw-Hill.

Burke, W.J., T. Schmugge, and J.F. Paris, 1979, Comparison of 2.8- and 21-cm microwave radiometer observations over soils with emission model calculations, JGR 84, pp. 287-294.

Camillo, P.J., and T.J. Schmugge, 1984, Correlating rainfall with remotely sensed microwave radiation using physically based models, IEEE Trans. on Geosc. and Rem. Sens. GE-22, pp. 415-423.

Edgerton, A.T., A. Stogryn, and G. Poe, 1971, Microwave Radiometric Investigations of Snowpacks, Final Rept. 1285R-4 of Contract 14-08-001-11828 between Aerojet-General Corp., El Monte, CA, and the U.S. Geological Survey.

England, A.W., 1974, The effect upon microwave emissivity of volume scattering in snow, in ice, and in frozen soil, Proc. URSI Spec Mtg on Microwave Scattering and Emission from the Earth, Berne, Switzerland, 23-26 Sept., 1974.

England, A.W., 1975, Thermal microwave emission from a scattering layer, JGR 80, pp. 4484-4496.

England, A.W., 1976, Relative influence upon microwave emissivity of fine-scale stratigraphy, internal scattering, and dielectric properties, Pageoph 114, pp. 287-299.

England, A.W., 1977, Microwave brightness spectra of layered media, Geophysics 42, pp. 514-521.

Grody, N.C., 1988, Surface identification using satellite microwave radiometers, IEEE Transactions on Geoscience and Remote Sensing, V. 26, pp. 850-859.

Hoekstra, P., and A. Delaney, 1974, Dielectric properties of soils at UHF and microwave frequencies, JGR 79, pp.1699-1708.

Moik, J., 1980, Digital Processing of Remotely Sensed Images, NASA, NASA SP-431.

NASA, 1978, The Scanning Multichannel Microwave Radiometer (SMMR) experiment, The Nimbus-7 Users Guide, The Landsat/Nimbus Project, Goddard Space Flight Center, NASA, p. 213-245.

Schmugge, T.J., 1983, Remote sensing of soil moisture: Recent advances, IEEE Trans. on Geosc. and Rem. Sens. GE-21, pp. 336-344.

Schmugge, T.J., 1987, Remote sensing applications in hydrology, Rev. Geophys. 25, pp. 148-152.

Schmugge, T.J., P.E. O'Neil, and J.R. Wang, 1986, Passive microwave soil moisture research, IEEE Trans. on Geosc. and Rem. Sens. GE-24, pp. 12-22.

Ulaby, F.T., R.K. Moore, and A.K. Fung, 1981, Microwave Remote Sensing, Active and Passive, Addison-Wesley.

Wang, J.R., T.J. Schmugge, W.I. Gould, W.S. Glazar, and J.E. Fuchs, 1982, A multi-frequency radiometric measurement of soil moisture content over bare and vegetated fields, Geophys. Res. Let. 9, p. 416-419.

Witkin, A., 1983, Scale-space filtering, Proc. Int. Joint. Conf. Artif. Intell., Karlsruhe, West Germany, p. 1019-1021.

Yuille, A., and T. Poggio, 1986, Scaling theorems for zero crossings, IEEE Trans. Patt. Anal. Mach. Intell., Vol. PAMI-8, No. 1, p. 15-25.

Zuerndorfer, B.W., A.E. England, M.C. Dobson, and F.T. Ulaby, 1989, Mapping freeze/thaw boundaries with SMMR data, submitted to J. Agriculture and Forest Meteorology.

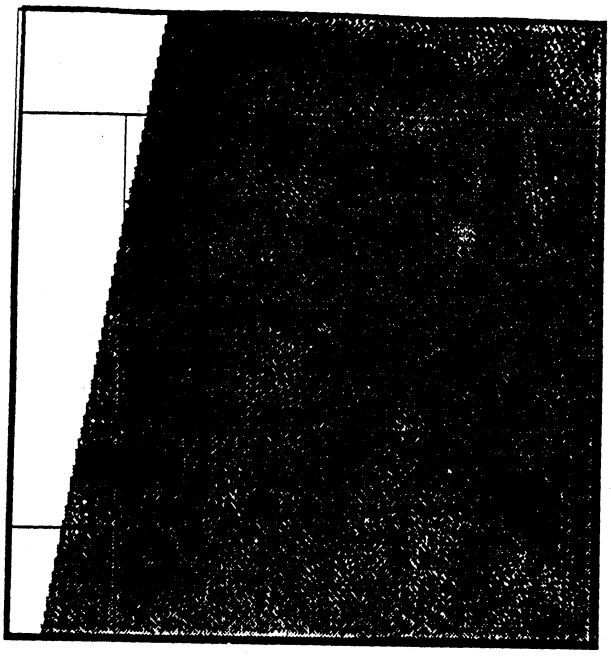

Figure 1. Freeze Indicator map of the test site, including a geographical map.

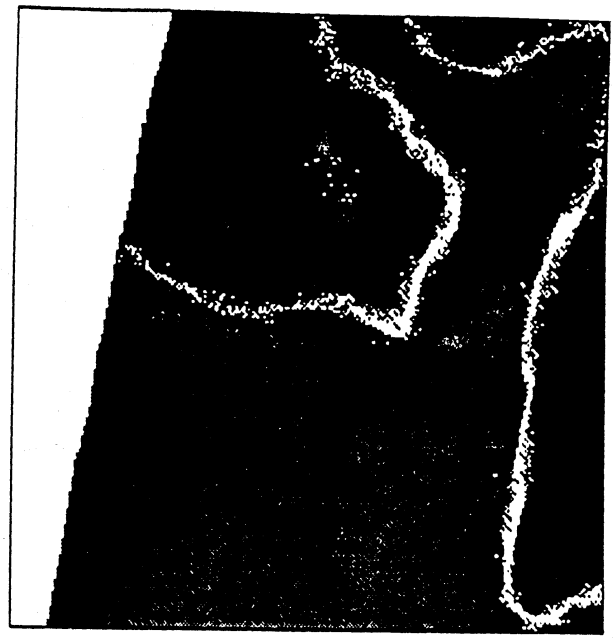

Figure 2. 37 GHz radiobrightness map of the test site at the (coarse) resolution of the SMMR 10.7 GHz channel.

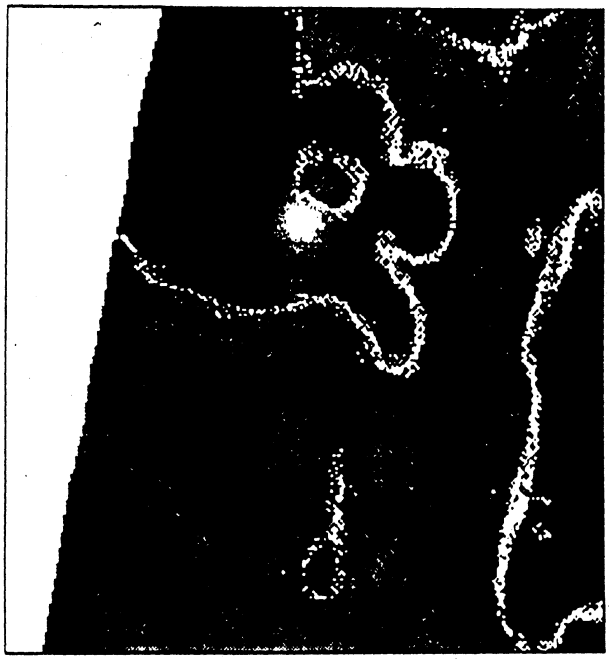

Figure 3. 37 GHz radiobrightness map of the test site at the (medium) resolution of the SMMR 18 GHz channel.

Figure 4. 37 GHz radiobrightness map of the test site at the (fine) resolution of the SMMR 37 GHz channel.

Recovery of Fine Resolution Information in Multispectral Processing[1]

Brian Zuerndorfer, Gregory H. Wakefield, and Anthony W. England

Department of Electrical Engineering and Computer Science
University of Michigan, Ann Arbor, MI 48109-2122

Email address: bwz @ caen.engin.umich.edu

ABSTRACT

In this paper, we consider multiple-sensor processing and develop a unified method for representing multiple-sensor data. When resolution varies between sensors, such a multiple-sensor system can be viewed as samples of a scale-space signal representation. We show that if the spatial transfer function of the sensors are Gaussian, then scale-space filtering can be used to recover small scale (fine resolution) information through extrapolation in scale. As an example of multiple-sensor processing, we consider multispectral processing of remote sensing in which images of surface scenes are simultaneously generated at different (center) frequencies.

INTRODUCTION

Scale-space filtering was introduced in the early 1980's as a technique for signal analysis over multiple scales [1,2]. The origins of scale-space filtering lie in the edge detection concerns of computer vision but have since been applied to other problems in computer vision [3,4] as well as a model for multiresolution systems [5]. In this latter context, scale-space analysis provides a mathematical framework for data integration in multiresolution systems that are characterized by classes of sensors varying along a dimension called *scale*. For example, multispectral analysis in remote sensing requires integration of data from constant-Q bandlimited sensors that vary in center frequency [6]. A simple approximation of such a multiresolution system is that of a multiscale system in which a single parameter, e.g., bandwidth, characterizes the primary differences among each of the bandlimited sensors. Under this approximation, the data from each sensor represents *samples* of the scale-space representation of the imaged object.

Formally, scale-space filter theory describes the effects of filter scale on functions e(x,s) of the form [1,2,7],

$$e(x,s) \equiv O\{r(x,s)\},$$

where O{.} is a linear operator and r(x,s) is a filter output signal given by,

$$r(x,s) \equiv h(x,s)*i(x).$$

The function i(x) is the input signal and h(x,s) is a family of filters which is parameterized by a continuous variable s. This variable s is inversely proportional to filter bandwidth and denotes the *scale* of the filter.

1 Work supported by NSF MIP-8657884 and the Shell Oil Company Foundation

Scale-space filtering represents the signal i(x) by the two-dimensional function r(x,s) and draws inferences about variations of i(x) from the threshold crossing contours of e(x,s). The location of these threshold crossings, x(s), is dependent on scale and calculated from

$$e(x(s),s) = \gamma(x(s)), \tag{1}$$

for some specified *threshold function* $\gamma(.)$. The threshold crossings form contours in the x-s plane. In the nomenclature of scale-space theory, the x-s plane is the *scale-space*, the function e(.,.) is the *scale-space image*, and the threshold crossing contours, x(s), are the *fingerprints*.

Although Zuerndorfer and Wakefield [7] have shown that the requirements can be relaxed while still preserving major points of the theory, the strongest theorems of scale-space signal representation [2,8] assume Gaussian kernels of the form

$$h(x,s) = \frac{1}{s\sqrt{2\pi k}} \exp\left[-\frac{1}{2}\left(\frac{x^2}{s^2 k}\right)\right], \tag{2}$$

and a Laplacian operator for O{.}. In this case, the fingerprints present a continuous track of the inflection points of the signal i(.) as it is filtered over scale. The inflection points can be used for locating "edges" in the signal [9].

Given the use of Gaussian kernels, Gaussian filtering can be used to degrade the resolution (broaden the PSF) of fine-resolution sensors in multiresolution systems to match that of a coarse-resolution sensor. Alternatively, given the features of a signal measured by a coarse-resolution sensor, it is useful to register their locations with signal features measured by fine-resolution sensors. Modelled as a multiscale system, these two problems represent *interpolation* and *extrapolation*, respectively, of the sampled fingerprints. In the following, we present a formal development of extrapolation in scale-space and then apply extrapolation to multispectral processing of remote sensing [6].

EXTRAPOLATION IN SCALE-SPACE

Extrapolation concerns determining the threshold crossing contours, x(s), given by,

$$h(x(s),s)*i_I(x(s)) \equiv r(x(s),s) = \alpha(x(s)), \tag{3}$$

where $\alpha(.)$ is a threshold function. The function $i_I(.)$ is an *indicator* composed of a linear combination of single sensor data,

$$i_I(.) \equiv \sum_{j=1}^{N} a_j i_j(.),$$

where $i_j(.)$ is the ideal output signal from the j^{th} sensor, and the a_j's are coefficients. The function $i_I(.)$ is the image output from the j^{th} sensor for a device having infinitesimal spatial resolution. Without loss of generality, the sensor data are ordered by increasing scale of the sensor. Comparing (3) with (1), the operator $O\{.\}$ in (3) is the identity.

The fingerprints x(s) in (3) are estimates of boundary locations in $i_I(.)$. True boundaries occur between surface regions having different $i_I(.)$ values, so that boundaries occur at x values where $i_I(.)$ crosses the threshold function,

$$i_I(x) = \alpha(x). \tag{4}$$

The threshold function $\alpha(.)$ is a linear function of x.

In general, $i_I(.)$ cannot be processed directly due to the finite PSF of the sensor. However, in the absence of noise, the threshold crossings of r(.,s) approach those of $i_I(.)$ as $s \to 0$, since the kernel h(.,s) approximates a delta function as $s \to 0$. To better approximate boundary locations, we seek x(s) for as small a scale as possible. If s_j is the finest scale at which data from the j^{th} channel is available, and $s_1 < \ldots < s_N$, then x(s) can only be determined for $s \geq s_N$. However $s_1 < s_N$, and the boundary estimate is improved if there exists a threshold function $\beta(.)$ such that,

$$h(u(s),s) * i_1(u(s)) \equiv p(u(s),s) = \beta(u(s)), \tag{5}$$

where u(s) are the fingerprints derived from (5), and

$$u(s) \approx x(s) \text{ for } s_N \geq s \geq s_1. \tag{6}$$

Note that u(s) for a particular threshold function $\beta(.)$ need only approximate x(s) over part of a single contour, and that different threshold functions are used to approximate x(s) for different contours.

To demonstrate the signal and threshold requirements to achieve (6), consider the Taylor expansion of x(s) about s_0,

$$x(s) = x(s_0) + (s - s_0)x'(s_0) + \frac{(s - s_0)^2}{2} x''(s_0) + \ldots . \tag{7}$$

By the implicit function theorem [10],

$$x'(s_0) = \frac{r_s(x_0, s_0)}{\alpha_x(x_0) - r_x(x_0, s_0)} \tag{8a}$$

$x''(s_0)$ = (8b)

$$\frac{(r_{xx}(x_0,s_0) - \alpha_{xx}(x_0))(x'(s_0))^2 + 2r_{xs}(x_0,s_0)x'(s_0) + r_{ss}(x_0,s_0)}{\alpha_x(x_0) - r_x(x_0,s_0)},$$

where $x_0 \equiv x(s_0)$; subscripted variables indicate partial differentiation. In (3) the threshold function $\alpha(.)$ is a linear, so that $\alpha_x(.) = A$ for some constant A, and $\alpha_{xx}(.) = 0$. By solution to the heat equation, the use of a Gaussian kernel yields, $r_s(x_0, s_0) = s_0 r_{xx}(x_0, s_0)$. As a result, (8a) can be written as,

$$x'(s_0) = -\frac{s_0 r_{xx}(x_0, s_0)}{r_x(x_0, s_0)}, \tag{9a}$$

and (8b) can be written as,

$x''(s_0)$ = (9b)

$$-\frac{r_{xx}(x_0,s_0)(x'(s_0))^2 + 2s_0 r_{xxs}(x_0,s_0)x'(s_0) + s_0^2 r_{xxss}(x_0,s_0)}{A - r_x(x_0,s_0)}.$$

Repeating the steps above for u(s) yields,

$$u(s) = u(s_0) + (s - s_0)u'(s_0) + \frac{(s - s_0)^2}{2} u''(s_0) + \ldots, \tag{10}$$

where,

$$u'(s_0) = -\frac{s_0 p_{xx}(u_0, s_0)}{p_x(u_0, s_0)}, \tag{11a}$$

$u''(s_0)$ = (11b)

$$\frac{p_{xx}(u_0,s_0)(u'(s_0))^2 + 2s_0 p_{xxs}(u_0,s_0)u'(s_0) + s_0^2 p_{xxss}(u_0,s_0)}{B - p_x(u_0,s_0)},$$

and $u_0 \equiv u(s_0)$. The threshold function $\beta(.)$ is linear, so that $\beta_x(.) = B$ for some constant B. Thus, for u(s) to approximate x(s), it is necessary that,

$$x'(s_0) = u'(s_0) \text{ and } x''(s_0) = u''(s_0)$$

or,

$$\frac{h(x,s) * \frac{d^n}{dx^n} i_I(x)}{A - h(x,s) * \frac{d}{dx} i_I(x)} = \frac{h(x,s) * \frac{d^n}{dx^n} i_1(x)}{B - h(x,s) * \frac{d}{dx} i_1(x)} \quad \text{for } n=1,2,3. \tag{12}$$

EXAMPLES

We apply the results of the previous section to a multi-spectral system that integrates data from N sensors, where each sensor operates at a different (center) frequency. In this system, each sensor receives energy using an aperture, e.g., devices such as lenses in optical applications, antennas in microwave application, and arrays in sonar applications that collect radiated energy that is emitted or reflected from a subject of interest. In this system, as the j^{th} sensor is scanned over a subject, the output signal is the convolution of the spatially varying radiation intensity of the subject with the radiation pattern (antenna pattern) of the aperture. The radiation intensity of the subject is equivalent to the scale-space input for the j^{th} sensor, $i_j(.)$. The radiation pattern of the aperture is equivalent to a scale-space filter impulse response of the j^{th} sensor $h(.,s_j)$, where the scale of the impulse response, s_j, is the width (beamwidth) of the radiation pattern; s_j is proportional to the wavelength of the sensor. In this system, true regional boundaries occur at level crossings of $i_I(.)$, and are approximated by the fingerprints x(s).

A class of functions for which (12) holds is that where different sensor inputs, $i_j(.)$, are scaled versions of each other. In this case, the indictor is given by,

$$i_f(x) = \left(\sum_j a_j\right) K(x) \tag{13a}$$

and the finest scale (highest frequency) input signal is given by,

$$i_1(x) = a_1 K(x), \tag{13b}$$

for an arbitrary function K(.). The significance of such functions can be seen in multiplicative models,

$$i_j(x) = I(x) R_j(x),$$

as are often used in image processing and remote sensing. In active remote sensing systems, I(.) and R_j(.) are surface illumination and reflection functions, respectively. In passive systems, I(.) and R_j(.) are surface temperature and surface emissivity, respectively. In both systems, R_j(.) is a function of the surface type and is dependent on frequency. As a result, the indicator is given by,

$$i_f(x) = \sum_j I(x) R_j(x). \tag{14}$$

An example of a surface satisfying (13a) and (13b) is one consisting of a single surface type, and a spatially varying illumination intensity or surface temperature.

Another class of functions that satisfies (12) is quadratic functions. In remote sensing applications, such signals occur in passive systems where surface temperature and surface emissivity change linearly in the vicinity of a boundary [11]. In this case, I_j(.) and R_j(.) are linear,

$$I(x) = \alpha_I x + \beta_I$$

$$R_j(x) = \alpha_{Rj} x + \beta_{Rj}$$

so that,

$$i_f(x) = \left(\sum_j a_j\right) x^2 + \left(\sum_j b_j\right) x + \left(\sum_j c_j\right) \tag{16a}$$

and

$$i_1(x) = a_1 x^2 + b_1 x + c_1 \tag{16b}$$

where,

$$a_j = \alpha_I \alpha_{Rj}$$

$$b_j = \alpha_I \beta_{Rj} + \beta_I \alpha_{Rj}$$

$$c_j = \beta_I \beta_{Rj}.$$

A simplified example of a one-dimensional surfaces model that satisfies (16a) and (16b) is shown in Figures 1-4 (this model is derived from [11]). In the figures, the indicator is composed of data from two sensors,

$$i_f(x) = i_1(x) - i_2(x), \tag{17}$$

where the scale of sensor 1 is less than the scale of sensor 2. In Figures 1-4, the functions i_1(.) and i_2(.) are quadratic in the vicinity of regional boundaries. The surface type changes at x=125, so that i_1(.) and i_2(.) exhibit different behavior in the vicinity of boundaries for x<125 and x>125 (Figure 1). A threshold level is selected to locate a boundary around the surface region with a low i_f(.) value. The corresponding fingerprint is shown in Figure 2. Figure 3 shows the i_1(.) function and threshold function, and the corresponding fingerprint is shown in Figure 4. Comparing the fingerprints of Figures 2 and 4 shows that the fingerprint of i_1(.) (Figure 4) is a reasonable match to the fingerprint of i_f(.) (Figure 2), particularly at smaller scales. Since the fingerprints of i_f(.) cannot be calculated at small scales, the fingerprints of i_1(.) can be used to approximate the fingerprints of i_f(.) at small scales.

CONCLUSION

For the cases of Gaussian filtering and linear threshold crossings, we've demonstrated that extrapolation of scale can be performed in multispectral processing for signals that satisfy (12). The fingerprints of extrapolated signals approximate the actual multispectral fingerprints at small scales, and can be used when the multispectral fingerprints are not available.

In showing the approximation of extrapolation fingerprints to multispectral fingerprints, only three terms of the Taylor expansion were exploited (i.e., (12) was satisfied for 3 terms). It can be shown that N>3 terms of a Taylor expansion can be used if (12) is satisfied for N terms. As a result, in the absence of noise, extrapolation fingerprints that match the actual multispectral fingerprints at N>3 terms of a Taylor expansion will provide a better approximation at small scales.

REFERENCES

[1] A. Witkin; "Scale-space filtering," *Proc. Int. Joint Conf. Artif. Intell.*; Karsruhe, West Germany; 1983; PP. 1019-1021.

[2] A. Yuille and T. Poggio; "Scaling theorems for zero crossings," *IEEE Trans. Patt. Anal. Mach. Intell.*, Vol. PAMI-8, No. 1; Jan. 1986; PP. 15-25.

[3] S. Barnard; "Stochastic stereo matching over scale," *Proc. DARPA Image Understanding Workshop*; 1988.

[4] A. Witkin, D. Terzopoulis, and M. Kass; "Signal matching through scale space," *Int. J. Computer Vision*, Vol. 1.; 1988; PP. 134-144.

[5] B. Zuerndorfer, A. England, and G. Wakefield; "The radiobrightness of freezing terrain," *Proc. Int. Geosci. Remote Sensing Symp.*, Vancouver, B.C.; 1989; PP. 2748-2751.

[6] J. Richards; *Remote Sensing Digital Image Analysis*; Springer-Verlag, Berlin; 1986.

[7] B. Zuerndorfer and G. Wakefield; "Extensions of scale-space filtering to machine sensing," submitted to *IEEE Trans. Patt. Anal. Mach. Intell.*.

[8] J. Babaud, A. Witkin, M. Baudin, R. Duda; "Uniqueness of the Gaussian kernel for scale-space filtering", *IEEE Trans. Patt. Anal. Mach. Intell.*, Vol. PAMI-8, No. 1; Jan 1986; PP. 26-33.

[9] D. Marr and E. Hildreth; "Theory of edge detection," *Proc. R. Soc. London B*, Vol. 207; 1980; PP. 187-217.

[10] C. Goffman; *Calculus of Several Variables*; Harper & Row; New York; 1965.

[11] B. Zuerndorfer, A. England, F. Ulaby, and C. Dobson; "Mapping freeze/thaw boundaries with SMMR data", submitted to *J. Agriculture and Forest Meteorology*.

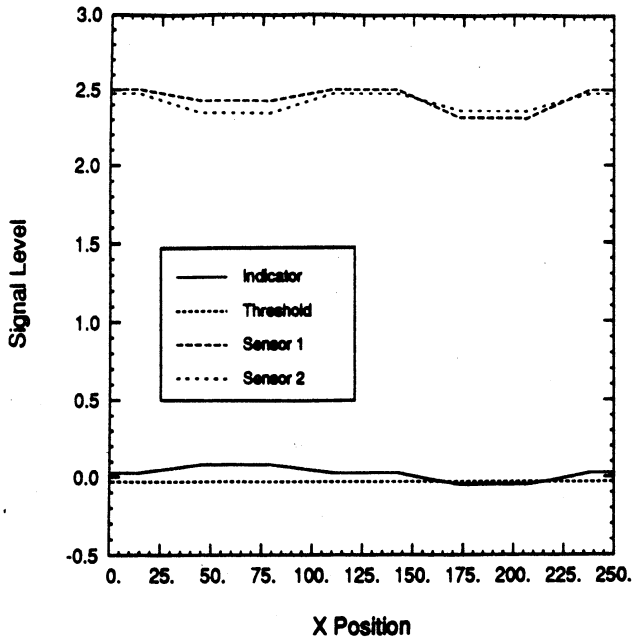

Figure 1. Sensor input signals, indictor, and threshold.

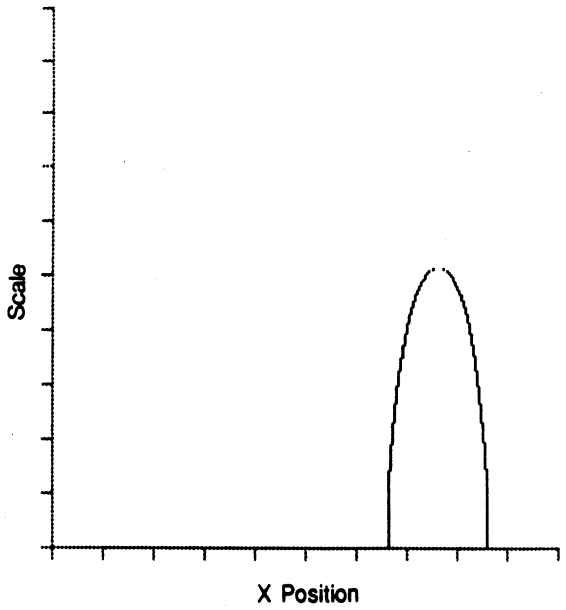

Figure 2. Indicator fingerprints.

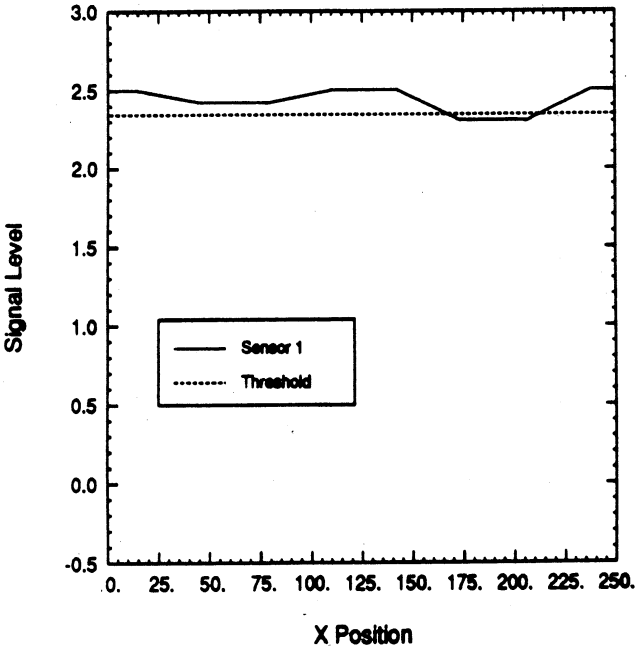

Figure 3. High frequency (fine scale) sensor input signal and threshold.

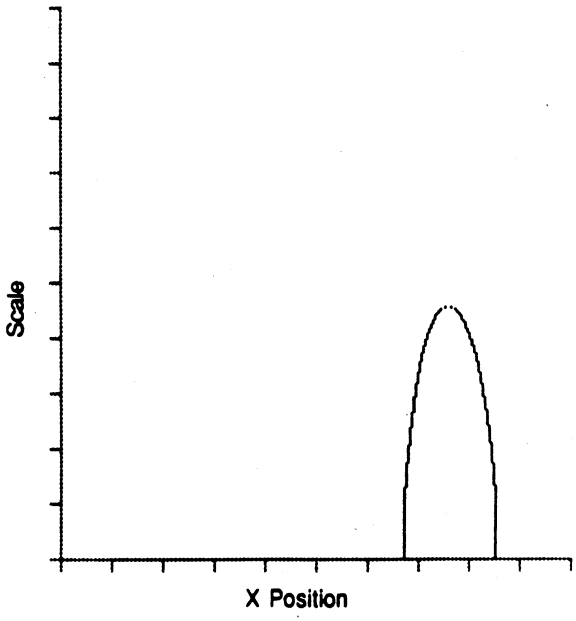

Figure 4. High frequency sensor fingerprints.